Print ISSN 0033-9008
Online ISSN 1880-1765

QUARTERLY REPORT of RTRI

Nov. 2024 Vol. 65 No. 4

CONTENTS

[H] Human factors
[I] Infrastructure
[N] Natural hazards
[O] Operations
[R] Rolling stock
[T] Technical system integration and interaction

RAILWAY TECHNICAL RESEARCH INSTITUTE

QUARTERLY REPORT of RTRI

Print ISSN 0033-9008
Online ISSN 1880-1765

November 2024 Vol. 65 No. 4

CONTENTS

PAPERS

RESEARCH REPORT

SUMMARIES

[H] Human factors
[I] Infrastructure
[N] Natural hazards
[O] Operations
[R] Rolling stock
[T] Technical system integration and interaction

Snow Falling Experiments and Modeling to Simulate Phenomena of Snow Dropping from Railway Vehicle

Hiroki TSUJI Yasushi KAMATA Daisuke TAKAHASHI
Meteorological Disaster Prevention Laboratory, Disaster Prevention Technology Division

In order to elucidate the mechanism of snow-falling from railway vehicles in winter, a mathematical model was studied to estimate the time taken for snow to fall from a railway vehicle in a warm tunnel. In addition, to validate the model which is based on the heat balance of snow accretion, snow falling experiments were carried out in a low-temperature room. Then the onset time of snow-falling was compared between the model and the results of the experiments. The result showed that it was possible to estimate the onset time of snow-falling, by setting an appropriate influence melting height on snow accretion at the interface between the metal plate and the snow accretion in the model.

Key words: *snow falling experiment, heat balance*

1. Introduction

When railway vehicles run in heavy snowfall areas in winter, snow on the track can be blown up and adhere to the bogies and other parts of the railway vehicles. The adhesion of snow to railway vehicles is called “snow accretion.” Snow accretions dropping from running vehicles, due to various causes, can cause flying ballast, damage to trackside equipment and blocked turnouts. This contributes to transport disruptions in winter. In order to reduce snow accretion on vehicles, railway operators wet the snow by sprinkling water on the track and to smooth snow under vehicle bodies (e.g., body mount structure), and remove the snow from railway vehicles at stations [1]. However, transport disruptions caused by snow accretion still occur. Therefore, the Railway Technical Research Institute is conducting research to develop effective and efficient countermeasures to snow accretion [2, 3]. One of these is the development of a method for estimating the amount of snow accretion [4].

Although studies have been carried out on the amount of snow accretion, the mechanisms underlying snow falling from railway vehicles (hereinafter referred to as “snow dropping”) has not been fully elucidated, since it is not easy to directly capture the occurrence of snow dropping because the timing and location of snow dropping varies. However, the amount of snow accretion may decrease due to melting and snow falling off vehicles in warm environments such as tunnels. Therefore, it is essential to elucidate the mechanism of snow dropping to improve the accuracy of estimations of snow accretion.

In this paper, we have devised a simple mathematical model for estimating the time taken for snow to fall. This paper also reports the results of a comparison between the model and experiments simulating snow dropping.

2. Modeling of snow dropping

Figure 1 shows a schematic diagram of the temperature and the amount of snow accretion on trains running in winter, assuming the section between Station A and Station B is in a heavy snowfall area and the section between Station B and Station C is in a snow-free area. It has been reported that the temperature inside tunnels in cold areas is higher than the outside temperature in winter [5]. This warming of railway vehicles inside tunnels is thought to facilitate snow dropping.

In this paper, we assume that snow dropping is caused by the melting of snow accretion at the interface between the snow accretion and the railway vehicle due to the rise in temperature. It is reported that in the case of Shinkansen trains, snow collects mainly on the end cover plates of the bogie cavity [4]. Moreover, as the end cover plate is mounted vertically, it is thought that the snow accretion on it is also likely to fall. Therefore, we focused on snow accretion on end cover plates in this paper.

In addition to the above, the following assumptions will be made in considering the model for snow dropping.
(1) The physical properties of snow are constant and there is no evaporation, sublimation and melting of snow accretion from the surface.
(2) In general, snow accretion occurs when snow particles adhere to other materials or to each other by various forces, but snow accretion is considered to occur only by adfreezing.
(3) Snow dropping may well be caused by pressure fluctuations due to the entry of railway vehicles into the tunnel, or by vibration due to passing turnouts, but these factors are not considered in this paper.

3. Simple modeling for snow dropping

In this paper, we construct a model (hereinafter referred to as “snow dropping model”) to estimate the time until the snow accretion falls when a railway vehicle enters a tunnel.

A schematic diagram of the snow dropping model is shown in Fig. 2. First, the snow accretion and the end cover plate are adhered together by adfreezing, and heat is supplied (i.e., increase in sup-

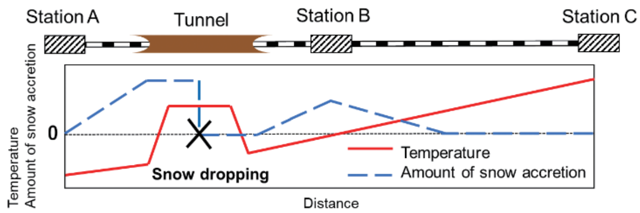

Fig. 1 A schematic diagram of the temperature and the amount of snow accretion on trains running from station A to station C in winter

plied amount of heat), which depends on the air temperature, wind speed, and area of snow accretion. The increase in the heat supplied warms the snow accretion, and the interface between the end cover plate and the snow accretion thaws (i.e., the freeze-thaw is dissolved), resulting in a decrease in the adhesion force. On the other hand, since it is assumed that there is no evaporation, sublimation and melting of the snow accretion from the surface, the gravity acting on the snow accretion does not change. Since the adhesion force decreases as the thawing of the interface progresses, snow dropping is considered to occur at the time (t_{slide}) when the adhesion force is less than gravity.

The snow dropping model can be divided into two parts: the part that calculates the process of the interface thawing and the part that calculates the relationship between adhesion force and gravity. The former is called the "thawing heat model" because the thawing of the interface is caused by an increase in the amount of heat supplied. The latter is called the "falling model" because snow accretion falls due to a change in the balance of two forces.

3.1 Thawing Heat Model

The thawing heat model calculates the process of the interface thawing. The process is calculated by establishing the relationship between the amount of heat supplied to the end cover plate and the snow accretion (hereinafter referred to as "supplied amount of heat: Q_s") and the amount of heat used for the interface thawing (hereinafter referred to as "thawing heat: Q_T"). Because of the difference in thermal conductivity between the snow (~10^{-1} W/mK, depending on density [6]) and the end cover plate (~10 W/mK for common materials), the temperature rise of the snow itself is considered to be small, so all the amount of heat supplied is assumed to be used to thaw the interface (1).

$$Q_s = Q_T \tag{1}$$

The amount of heat supplied is the product of the heat supplied per unit time (q) and time (t). Based on the difference in thermal conductivity described above, it is assumed that the amount of heat supplied required to thaw the interface is provided by the running wind from the area of the end cover plate without the snow accretion. The heat supplied per unit time to the end cover plate can be described by the following equation.

$$q = h\Delta S\Delta T_e \tag{2}$$

where h is the heat transfer coefficient, ΔS is the area without snow accretion on the end cover plate, and ΔT_e is the temperature difference before and after snow dropping from the end cover plate.

The heat transfer coefficient can be described by the following equation using a Nusselt number (N_u).

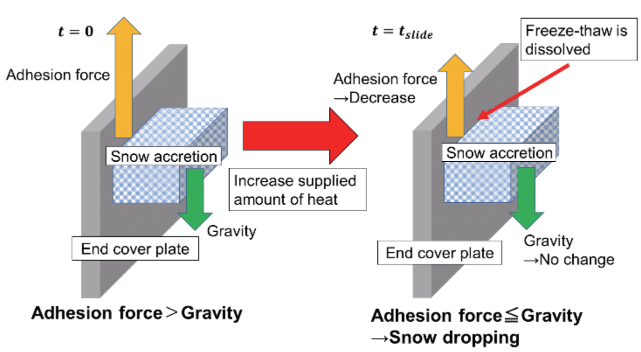

Fig. 2 A schematic diagram of snow dropping model

$$h = \frac{\kappa_a N_u}{L_e} \tag{3}$$

where κ_a is the thermal conductivity of air and L_e is the representative length of an object perpendicular to the wind, for example, the vertical length of the end cover plate.

From (2) and (3), the amount of heat supplied can be described by the following equation.

$$Q_s = qt = \frac{\kappa_a N_u}{L_e}\Delta S\Delta T_e t \tag{4}$$

For a Nusselt number, different notational formulas were used depending on the wind speed. Equation (5) is used when the wind speed is 0 m/s, and equation (6) is used at other times [7].

$$N_u = 0.59(Gr \cdot Pr)^{\frac{1}{4}} \tag{5}$$

$$N_u = 0.664 \cdot Re^{\frac{1}{2}} \cdot Pr^{\frac{1}{3}} \tag{6}$$

where Gr is a dimensionless number called a Grashof number, and is described by the following equation when the gravitational acceleration is g, the volumetric thermal expansion coefficient of air is β, the initial temperature of the end cover plate is T_{e_i}, the air temperature is T_a, and the kinematic viscosity of air is ν.

$$Gr = \frac{{L_e}^3 g\beta(T_{e\_i} - T_a)}{\nu^2} \tag{7}$$

where Pr is the Prandtl number, which is 0.71 for air, and Re is the Reynolds number, which is described by the following equation using the wind speed W.

$$Re = \frac{L_e W}{\nu} \tag{8}$$

Next, we discuss the amount of heat of thawing. The amount of heat of thawing required for the ice at the freezing point to rise in temperature and change to water can be described by the following equation.

$$Q_T = \rho_i V_i C_v \Delta T_i + Q_i \rho_i V_i = \rho_i V_i (C_v \Delta T_i + Q_i) \tag{9}$$

where ρ_i is the density of ice, V_i is the volume of ice melted in the interface by time (t), ΔT_i is the temperature rise range of ice, C_v is the specific heat of ice, and Q_i is the heat of fusion of ice.

To determine the amount of heat of thawing, the volume of ice thawed in the interface is necessary, but this is difficult to measure directly. Therefore, for simplicity, we assume that the snow accretion which was a mixture of ice and air of identical particle size would change to a mixture of ice, water and air as the ice melts and changes to water over time (Fig. 3).

In the Y-Z plane, the area of ice adfrozen to the end cover plate (hereinafter referred to as "effective adfrozen area: S_e") gradually decreases with melting. Therefore, we consider the effective adfrozen area as a function of time.

Since the snow accretion is a mixture of ice and air in the initial state, using the density of snow accretion (ρ_s), the proportion of ice in the snow accretion (i.e., presence rate α) can be described by the following equation.

$$a = \frac{\rho_s}{\rho_i} \tag{10}$$

Assuming that the effective adfrozen area is proportional to the density of snow accretion, using the area of snow accretion (S_i), the effective adfrozen area in the initial state can be described by the following equation.

$$S_e(0) = S_i a \tag{11}$$

Since the number of melting ice particles increases as time passes, the volume of ice (V_i) melted by time (t) can be described by the following equation when the influence range in the X direction is the melting height (H).

$$V_i = (S_e(0) - S_e(t))H \tag{12}$$

From (9), (11) and (12), the amount of heat of thawing can be described by the following equation.

$$Q_T = \rho_i (S_i a - S_e(t))(C_v \Delta T_i + Q_i)H \tag{13}$$

3.2 Falling model

The falling model considers the relationship between the adhesion force (F_a) and the gravity (F_g). In the initial state, the snow accretion does not fall because the adhesion force is greater than the gravity. Since it is assumed that there is no melting of the snow accretion from the surface, the gravity is constant and can be expressed as the product of the mass of the snow accretion (M) and the acceleration of gravity (g). On the other hand, since the adhesion force is due to adfreezing, it is obtained by the product of the ice adhesion strength (σ_i) and the effective adfrozen area. Assuming that the adhesion strength is constant, the adhesion force will decrease as the effective adfrozen area decreases. Therefore, the fall of snow accretion occurs when the adhesion force and gravity are equal.

$$F_a = F_g \Leftrightarrow \sigma_i S_e(t) = Mg \tag{14}$$

3.3 Snow dropping model

Combining the thawing amount of heat model and the falling model, the snow dropping model is constructed. Suppose that the snow accretion falls at time (t_{slide}), the following equation is derived from (14).

$$S_e(t_{slide}) = \frac{Mg}{\sigma_i} \tag{15}$$

Note that the above equation shows that the effective adfrozen area when the snow accretion falls depends on the mass of the snow accretion.

Solving equations (1), (4), (13), and (15) for time (t_{slide}) leads to (16).

$$t_{slide} = \frac{\rho_i L_e \left(S_i a - \frac{Mg}{\sigma_i}\right)(C_v \Delta T_i + Q_i)H}{\kappa_a N_u \Delta S \Delta T_e} \tag{16}$$

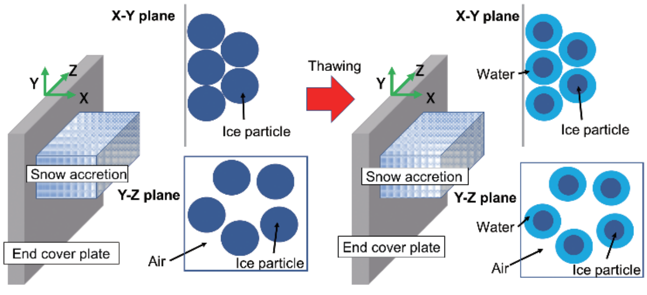

Fig. 3 A schematic diagram of melting snow accretion

Consider the application of the snow dropping model to snow dropping. The length and area of the end cover plates are known, and the temperature increase at the snow accretion and the end cover plate can be considered as the difference between the temperature at the time of snow accretion and the temperature at the time of snow dropping (= 0°C). The density, area, and mass of snow accretion have been observed, although the number of observations is small. The wind speed at the end cover plate, which is included in the Nusselt number, can also be roughly estimated from the airflow analysis of railway vehicles. By substituting other physical constants, the only unknown in (16) is the melting height H. Therefore, by setting an appropriate value for the melting height, the time at which snow dropping occurs can be calculated.

4. Experiments for snow dropping

Experiments to reproduce snow dropping phenomena (hereinafter referred to as “snow falling experiments”) were carried out to investigate the parameters that affect the snow dropping model. The snow falling experiments were conducted under the following conditions.
(1) Snow accretion area is constant.
(2) Positive temperature conditions for a long tunnel.
(3) Wind speed corresponding to the wind of moving railway vehicles.

4.1 Methods

(1) Snow sample creation

A frame of a fixed area (“small”: 10,000 mm^2, “medium”: 22,100 mm^2, “large”: 50,400 mm^2) was placed on a SUS304 metal plate (300 mm × 200 mm × 1.5 mm) simulating an end cover plate, into which natural snow stored in a low-temperature chamber was placed using a sieve. Snow samples were then formed to a height 50 mm, the frame removed and stored in a cold room at −30°C for freezing (Fig. 4).

(2) Snow falling experiments

Snow samples were placed on a trestle at the exit of the blower in a low-temperature laboratory set at constant temperatures (5°C, 10°C, and 15°C) and were subjected to a constant wind speed (0-20 m/s in 2.5 m/s increments) (Fig. 5). In order that only the surface of the end cover plate where snow accretion exists would be exposed to wind as in railway vehicles running conditions, insulation was applied to the back of the metal plate. The maximum running speed of trains in Japan is 320 km/h (~89 m/s), and it is known that the ratio of wind speed to running speed is about 0.5 near the middle between the lower edge of the railway vehicle and the ground surface [8], and the wind speed at the end cover plate is considered to be lower than that of the middle. Therefore, in the snow falling experiments, the wind speed was assumed to be lower than the running

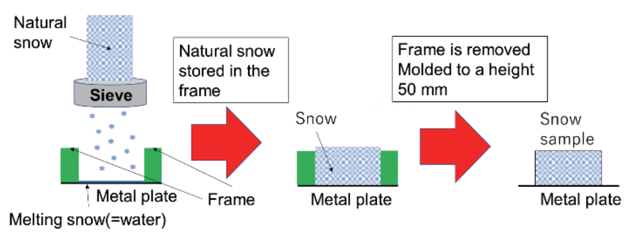

Fig. 4 A schematic diagram of snow sample creation

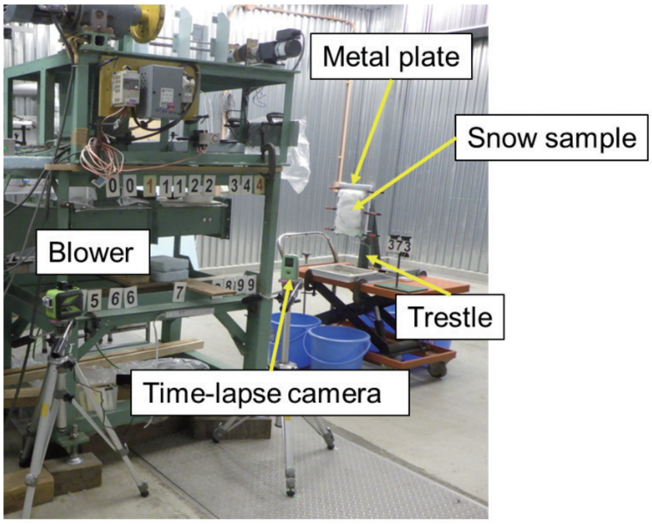

Fig. 5　Photo of snow falling experiment

speed. A time-lapse camera (Brinno, TLC200) was used to capture the conditions of the snow sample, and the time from the start of the air blast to the start of sliding (hereinafter referred to as "sliding time") was read from the video.

4.2　Results

Figure 6 shows the relationship between wind speed and sliding time for varying air temperatures and snow accretion areas. For all conditions of temperatures and snow accretion areas, the sliding time tended to shorten as the wind speed increased. At the same wind speed, the sliding time tended to shorten as the temperature increased and the snow sample area decreased.

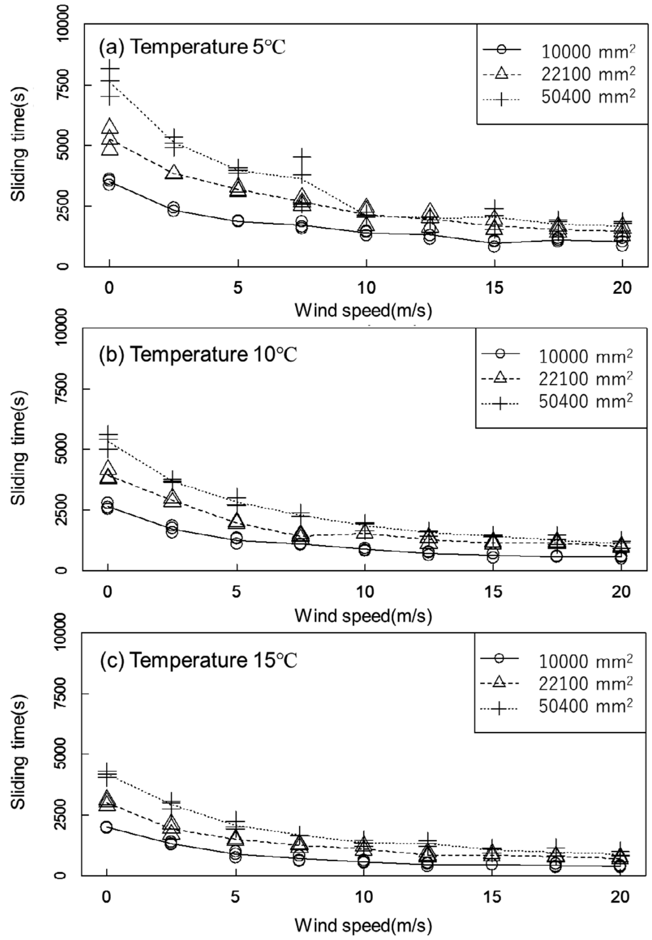

Fig. 6　Relationship between wind speed and sliding time

5.　Comparison of experimental results with model calculations

In this chapter, we compare the time at which snow dropping occurs derived by the snow dropping model (hereinafter referred to as "estimated time") with the results of experiments (sliding time) and discuss the validity of the model calculations. Table 1 shows the parameters used in (16).

Figure 7 shows a comparison of the sliding time and the estimated time at different temperatures for a "medium" snow sample area. The interface of snow sample after the snow falling experiments showed that the snow sample in the range of about 10 mm from the interface contained water, so the melting height was set to 10 mm for the model.

In the snow falling experiments at 10°C and 15°C (wind speeds of 2.5 to 20 m/s), the sliding time was plotted on the 1:1 line in Fig. 7, so it can be assumed that the estimated time was in agreement with the sliding time. In the experiment at 5°C (especially at wind speeds of 2.5 to 10 m/s, the area surrounded by blue line in Fig. 7), the estimated time is underestimated compared to the sliding time, but the correlation between sliding times and estimated times is generally good. On the other hand, in the snow falling experiments with a wind speed of 0 m/s, the estimated time was greatly overestimated (at the area surrounded by red line in Fig. 7).

Figure 8 shows a comparison of sliding time with estimated time in snow falling experiments for different snow accretion areas at 10°C temperature. Both axes are graduated on logarithmic scales. In the snow falling experiments with a "medium" snow sample area, the sliding time and the estimated time are in some agreement, except for a 0 m/s wind speed. On the other hand, for all wind speeds, the estimated time is underestimated for the "small" snow sample areas (especially in the area surrounded by the blue line in Fig. 8) and overestimated for the "large" snow sample areas (especially in the area surrounded by the red line in Fig. 8). In the snow falling experiments with a wind speed of 0 m/s at all snow sample areas, the results show a different tendency with other results (especially in the area surrounded by the green line in Fig. 8). However, the correlation between the sliding time and the estimated time is generally good.

In the experiment with a wind speed of 0 m/s, the discrepancy between the sliding time and the estimated time tends to be relatively large, which may be due to the different equations for a Nusselt number with respect to wind speed. One of the reasons for the discrepancy between the sliding time and the estimated time with respect to the snow sample area is that the snow sample is assumed not to melt in the snow dropping model, but the snow sample melts in the snow falling experiments (Fig. 9). As the snow sample melts, the snow accretion area decreases and the heat supplied increases, while the mass of the snow sample decreases. The increase in heat supply shortens the sliding time, while the decrease in the mass of the snow sample lengthens the sliding time because the snow accretion is retained even if the adhesion force is small. In snow falling experiments, the former was considered to have a greater effect when the snow sample area was small, while the latter was considered to have a greater effect when the snow sample area was large. The snow melting process from the surface needs to be incorporated into the snow dropping model in the future.

From the above, it was found that by keeping the melting height constant, the correlation between the estimated time and the sliding time is generally good, although deviations between the estimated time and the sliding time are observed when the temperature is 5°C and the snow sample areas are different. During actual railway vehicle running, it may be possible to calculate the time until snow dropping occurs in the tunnel using the snow dropping model by setting the appropriate melting height as a function of temperature.

6. Conclusions

We constructed a snow dropping model that can estimate snow

Table 1 Parameters used in this chapter

Parameter (unit)	Value	Description
L_e (mm)	300	Length of metal plate
S_i (mm^2)	10000(small) 22100(medium) 50400(large)	Area of snow sample
ΔS (mm^2)	50000(small) 37900(medium) 9600(large)	Difference between area of metal plate and snow sample
$a = \frac{\rho_s}{\rho_i}$ (-)	Change in each experiment	Measure density of snow sample
M (kg)	Change in each experiment	Measure mass of snow sample
ΔT_i (°C)	30	Difference between temperature of cold room and 0°C
N_u (-)	Change in each experiment	Calculated by (5) and (6) and below parameters
β (1/°C)	Change in each experiment	Calculated by temperature of low temperature laboratory
ν (m^2/s)	Change in each experiment	Calculated by temperature and pressure of low temperature laboratory
T_a (°C)	5, 10, 15	Temperature of low temperature laboratory
W (m/s)	0, 2.5, 5, 7.5, 10, 12.5, 15, 17.5, 20	Wind speed of blower
T_{e_i} (°C)	-30	Temperature of cold room

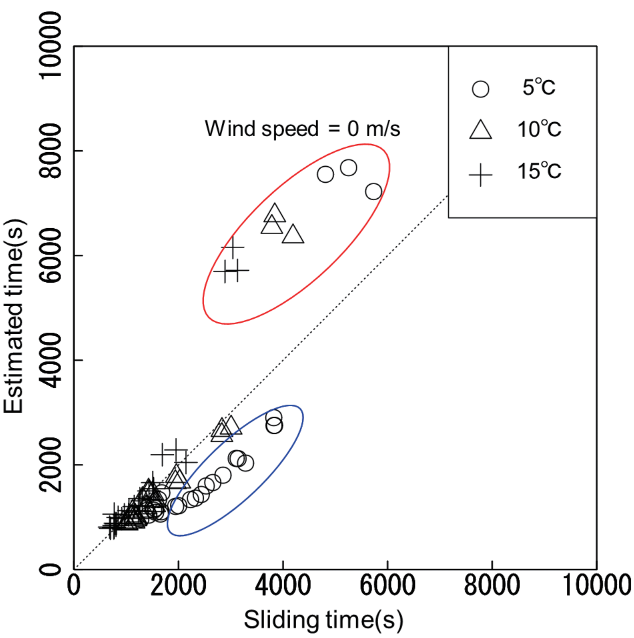

Fig. 7 A comparison of the sliding time and estimated time at different temperatures for a "medium" snow sample area

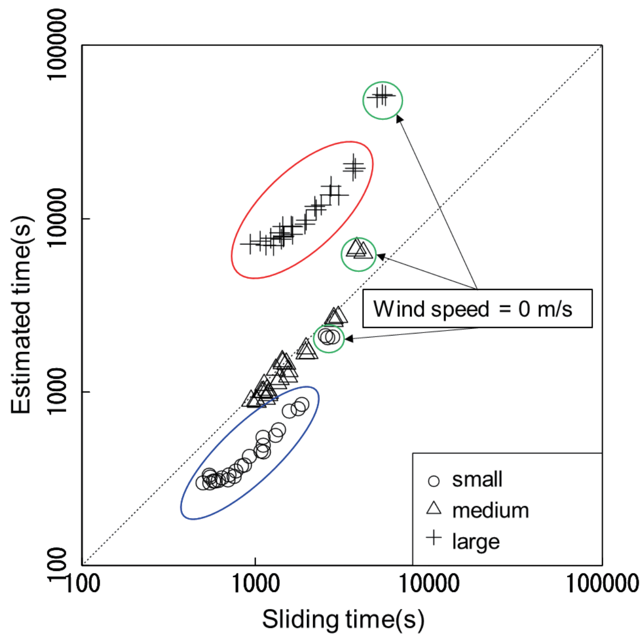

Fig. 8 A comparison of sliding time with estimated time in snow falling experiments for different snow sample area at 10°C

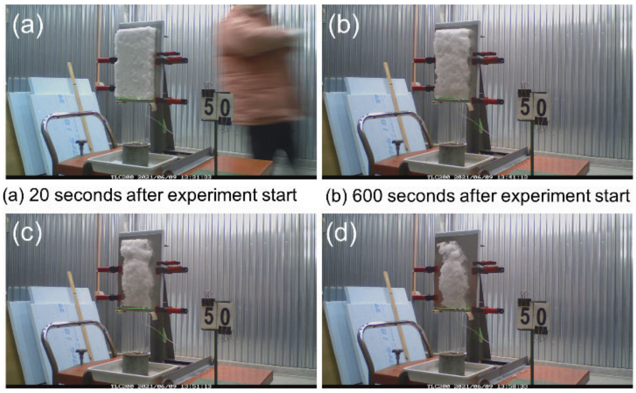

(a) 20 seconds after experiment start (b) 600 seconds after experiment start

(c) 1200 seconds after experiment start (d) 1640 seconds after experiment start = Sliding time

Fig. 9 A snow sample is melting in the experiment

dropping time. Although the model uses many assumptions, we have confirmed that it can estimate the onset time with some accuracy for the results of the snow falling experiments. To improve the accuracy of the model, it is necessary to take into account the melting process of the snow accretion and to investigate appropriate values for the melting height.

By applying this model to an actual running of railway vehicle, it should be possible to determine how long it takes for snow dropping to occur after a railway vehicle enters a tunnel. Since the running speed of railway vehicles is generally fixed, it is possible to identify the location of snow dropping based on the time when snow dropping occurs. If the locations where snow dropping frequently occurs can be extracted, it will be possible to study countermeasure prioritization.

The above is just one example of a use for the snow dropping model. In the future, we would like to contribute to more efficient countermeasures against snow accretion and snow dropping.

This paper is a reorganization of Reference [9].

References

[1] Azuma, T. and Horikawa, S. et al., “Countermeasure Against Snow,” *JR EAST Technical Review*, No. 16, pp. 31-34, 2010.
[2] Takami, H. and Araki, Y. et al., “Measures Against Snow Accretion Around Shinkansen Bogies Using Running Wind,” *QR of RTRI*, Vol. 64, No. 2, pp. 129-134, 2023.
[3] Fujii, T., Endo, T. and Imai, T., “Prevention of Snow Accretion to and its Dropping from Car Body Using a Panel-Heater,” *QR of RTRI*, Vol. 32, No. 3, pp. 174-181, 1991.
[4] Kamata, Y., Shishido, M. and Sato, R., “Method for Estimating Snow Accretion on Shinkansen Bogies using Weather Data,” *QR of RTRI*, Vol. 62, No. 4, pp. 245-250, 2021.
[5] Andrén, A., Dahlstöm, L. and Nordlund, E., “Temperature Flows in Railway Tunnels: Field Measurements of Frost Penetration,” *Journal of Earth and Geotechnical Engineering*, Vol. 10, No. 5, pp. 161-194, 2020.
[6] Matthew, S., Jon, H. et al., “The thermal conductivity of seasonal snow,” *Journal of Glaciology*, Vol. 43, No. 143, pp. 26-41, 1997.
[7] The Japan Society of Mechanical Engineers, *JSME Textbook Series Heat Transfer*. Maruzen Publishing Co., Ltd., Tokyo, Japan, pp. 55-97, 2005 (in Japanese).
[8] Ido, A. and Iwasaki, M., “Study on Air Flow between Underside of Railway Vehicle and Track On-Track Tests,” *RTRI Report*, Vol. 30, No. 7, pp. 35-40, 2016 (in Japanese).
[9] Kamata, Y., Tsuji, H. and Takahashi, D., “Snow Falling Experiments and Modeling to Simulate Phenomena of Snow Falling from Railway Vehicle,” *RTRI Report*, Vol. 38, No. 1, pp. 9-15, 2024 (in Japanese).

Authors

Hiroki TSUJI
Researcher, Meteorological Disaster Prevention Laboratory, Disaster Prevention Technology Division
Research Areas: Snow Damage Safety

Daisuke TAKAHASHI
Researcher, Meteorological Disaster Prevention Laboratory, Disaster Prevention Technology Division
Research Areas: Snow Damage Safety

Yasushi KAMATA, Ph.D.
Senior Chief Researcher, Head of Meteorological Disaster Prevention Laboratory, Disaster Prevention Technology Division
Research Areas: Snow Damage Safety

Operational Risk Assessment Method Based on Wayside and Vehicle Condition Information for Autonomous Train Operation

Yuki OTA **Akihiro GION**
Train Control Systems Laboratory, Signalling and Operation Systems Technology Division

Sho NISHIMOTO **Yuki SAKURAI**
Train Control Systems Laboratory, Signalling and Operation Systems Technology Division

We are developing an autonomous train operation system that allows trains to operate automatically while controlling wayside equipment based on the condition of the vehicle and wayside equipment. Autonomous train operation not only controls the acceleration and deceleration of trains, achieved through automatic operation, but also automatically makes operational decisions on board. We have developed the railway dynamic map as an information infrastructure for collecting and sharing onboard and wayside condition information needed for operational decision making and for risk assessment. This paper provides an overview of condition information management and risk assessment using the railway dynamic map.

Key words: *autonomous train operation, operation risk assessment, dynamic map, information sharing*

1. Introduction

Automatic Train Operation (ATO) has already been in practical use in subways and AGT (Automated Guideway Transit). ATO has been attracting attention with its purpose of improving efficiency and cost reduction of railway operations. In recent years, studies and demonstration tests of ATO in Japan [1], [2] have been conducted with the goal of achieving driverless operation on general railway lines.

As an evolution of ATO, we are researching an autonomous train operation system [3] to realize safer and more flexible train operation with as few ground facilities as possible. This autonomous train operation aims to systematize the handling of information, and to operate trains autonomously while the trains themselves control the wayside facilities based on the status information collected on board. The difference between autonomous operation and conventional ATO is that in addition to train acceleration/deceleration control realized in ATO, operation decisions, which were conventionally handled by command staff and ground equipment, are performed automatically onboard the train in autonomous operation. To realize such a system, it is necessary to develop a method for integrating various types of status information on the vehicle, and a method for sharing information between ground and vehicle or vehicles.

In this research, we studied a method for collecting and managing condition information and a risk assessment method based on condition information as elemental technologies to realize onboard operational decisions.

2. Outline and challenges of autonomous train operation

2.1 Outline of autonomous train operation

2.1.1 Current ATO

The level of automation of ATO systems is classified into GOA (Grade Of Automation) 0 to 4, as shown in Table 1 [4], [5], where the higher the number, the higher the level of automation. For example, in the ATO in practical use on subways in Japan, a driver is on board to operate the system, which corresponds to GOA2. The more advanced GOA3 and GOA4 systems are used on elevated or underground tracks, where platform doors are installed, preventing passenger and object access to the tracks. In these systems, acceleration and deceleration of trains are adjusted so that they run according to speed patterns created in advance in accordance with the speed limit at each location and the running time between stations. In recent years, the identification of technical issues and requirements for implementing automatic operation equivalent to a level higher than the system with an attendant at the front of the train (referred to as GOA2.5) in general line sections where there are level crossings, etc., have been studied [6].

2.1.2 Autonomous train operation

In autonomous train operation, driverless operation, which corresponds to GOA3 or higher, is further advanced to automatically make appropriate operation decisions based on various status information, in addition to conventional acceleration/deceleration control. Figure 1 illustrates how we realize the autonomous train operation system that we are developing.

As shown in Fig. 1, each train registers conditions inside and along the tracks, controls running speed and directly controls ground equipment, such as level crossings, from onboard. The following five research and development elements are required to realize an autonomous driving system:

1) Detection of abnormalities on and along railway tracks using

Table 1 Classification of automatic train operation according to IEC 62267 (JIS E 3802) [4], [5]

Level	Type of Crew	Practical example in Japan
GOA0	Driver (and conductor)	Trams
GOA1		General railways
GOA2	Driver	Subways, Elevated railways
GOA3	Staff (anywhere on the vehicle)	Monorail line
GOA4	Without staff	AGT lines

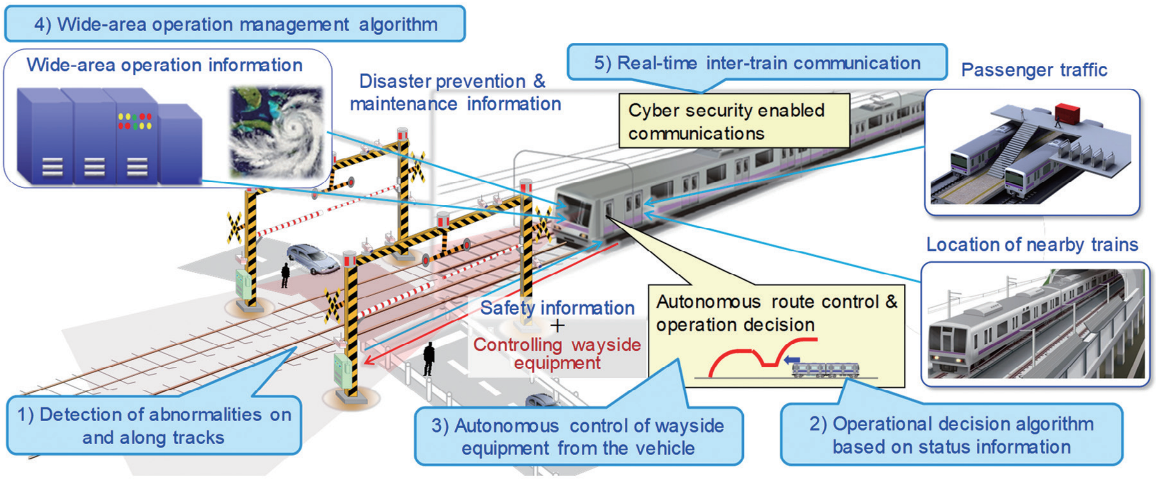

Fig. 1 Vision of autonomous train operation

images and radar.

2) An algorithm that judges whether trains can be operated by integration of both information on the status of trains on and along the railway tracks and information on status of vehicles.

3) Autonomous control of wayside equipment from the train using wireless radio technology.

4) A wide-area operation management algorithm for prevention of delay propagation and early delay recovery, energy saving, etc.

5) Real-time inter-train communication that considers cyber security.

The establishment of these technologies would lead to realizing a low-cost automated driving system for general railway lines and highly automated driving with less wayside equipment.

2.2 Challenges of autonomous train operation

In particular, the realization of the operation decision algorithm shown in 2), described in 2.1.2, requires an on-board method for integrating various pieces of status information and a method for determining the range within which trains can be safely operated.

In current railway operations, a dispatcher in an Operation Control Center (OCC) makes operational decisions and restrictions based on information detected by wayside equipment, and crews operate trains according to the operating regulations instructed by the dispatcher. In addition, if the crew or the system notices an abnormality on the track or in the condition of the train, a decision is made to stop the train to ensure safety. Figure 2 shows the flow of information related to the operational decisions. On the ground side, the OCC consolidates information from various monitoring systems, disaster prevention information systems, etc. to make operational decisions, and if operational restrictions are necessary, the OCC informs the crew through the dispatcher of operational restrictions and temporary speed limits. In addition, a method that does not involve the OCC is to monitor and issue alarms using on-site devices such as obstacle detectors at level crossing and rockfall detectors.

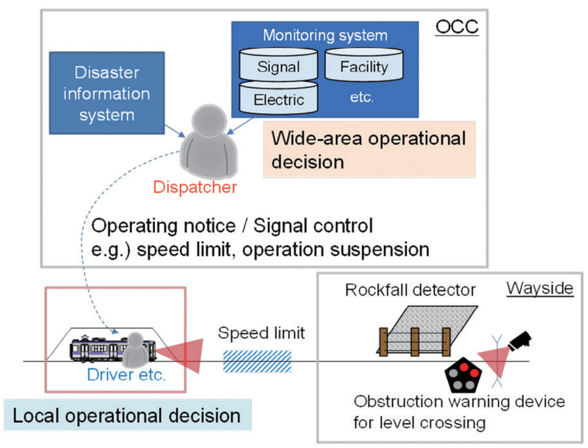

Fig. 2 Current operational decision

To realize autonomous train operation, it is required not only to confirm the safety of the train's own recognition range, but also to correctly recognize the situation outside of the train's visual range for appropriate control. However, the information that can be transmitted and received between the wayside and the trains is currently limited to instructions or an overview of the situation, so that most of the information acquired or aggregated by the OCC or train is not utilized by the other equipment.

Therefore, to realize an autonomous operational system, in addition to a method for acquiring such status information, it is necessary to have a method for evaluating the risk of hazards in order to make operational decisions by aggregating and sharing a large amount of information.

3. Information management method

3.1 Information necessary to make operational decisions

The information required for operational decisions is largely derived from onboard, wayside, and construction and other planning information. This information is provided by facilities managed by railway operators and by public agencies. Examples of relevant information and each characteristic of the information are summarized in Table 2.

The operational risk to train operations may arise when obstructions on or near the tracks make it unsafe for the train to pass through or remain at a point, and when the condition of the train cars makes it impossible for the train to continue running. Therefore, the information shown in Table 2 which shows characteristics of status information should be used to evaluate operational risks.

The information can be handled in the following ways. First, the information that can be detected by wayside equipment should

Table 2 Characteristics of status information

Source	Example of information	Characteristics
On-board	·Status of electrical equipment ·Noise ·Vibration	·Affects whether trains can continue to run ·Changes over time
	·Forward camera or radar	·Detection by relative distance from train location ·Short-term change of state
Wayside equipment	·Passenger fall detector ·Anemometer ·Earthquake ·Weather alert ·Status of wayside infrastructure (electrical power, signalling, broken rail detection, etc.) ·Rock fall detection	·Source location and alarm area are known ·Changes over time
Plan	·Maintenance area ·Speed limit for construction	·Range can be pre-determined by day or time

be used to define the target area in advance according to the location of the equipment and treated as a risk occurrence when an abnormality occurs. On the other hand, the information detected on board, such as disturbances on the tracks or wayside, should be set as occasional risk information. The vehicle status information that can be detected on board the vehicle is used to control the train by overriding decisions based on other status information as to whether the train can continue running from its current location. Information from planning could be used to assess risk of the scope of work, apply mitigations and also change the status as work progresses.

3.2 Elements of information integration

There are various types of status information required for risk assessment in autonomous driving, as indicated in Section 3.1. Each of these types of information has different temporal characteristics of information change, ranging from those that change from moment to moment to those that remain unchanged over a long period of time. As a method for centrally handling information with such different temporal characteristics, the dynamic map is being studied in the automotive field [7]. A conceptual diagram is shown in Fig. 3. The dynamic map is classified into four levels according to the temporal characteristics of information change: dynamic, semi-dynamic, semi-static and static. For example, information on obstacles in front, which may change suddenly, is classified as dynamic information, while lane information which does not change over a long period unless there is large-scale construction, is classified as static information. Based on the information allocated to these four layers, dynamic maps for vehicles are used to avoid hazards during automatic driving and to avoid traffic congestion. This information is displayed on the dynamic map with latitude and longitude coordinates.

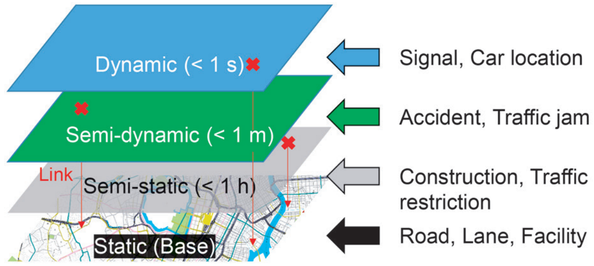

Fig. 3 Overview of dynamic map

Such a concept can also be used for autonomous railway operation. One point that differs from automobiles is that there are two types of position of the status information to be displayed: one is according to latitude and longitude coordinates and the other is according to the position on the railway track (e.g., distance from the starting point). Therefore, we developed a system that has a railway track map side in addition to the map side, and devised a method to integrate and utilize the information developed on the two sides. This is referred to as the railway dynamic map[8] and an overview is shown in Fig. 4.

Since the railway dynamic map has two surfaces, a map surface and a railway track drawing, it not only allows status information to be integrated and managed centrally, but also allows information to be provided according to the way it is used. When used for autonomous operation control, the information developed on the railway track diagram is effective because the risk assessment is based on the train's position on the track. On the other hand, from the point of view of providing information to the dispatcher and other human systems, it is also possible to display the information developed on the map to support decision-making according to the current situation.

3.3 Risk assessment method using the railway dynamic map

The railway dynamic map is a database that integrates and manages dynamic information from trains and various monitoring systems. Therefore, it can be regarded as a system that aggregates sensing data in the railway.

Each train, disaster prevention system, facility monitoring system, or facility along the line, respectively, converts the information which it acquires or detects into the format of the railway dynamic map and distributes it to other trains. To ensure that there is no omis-

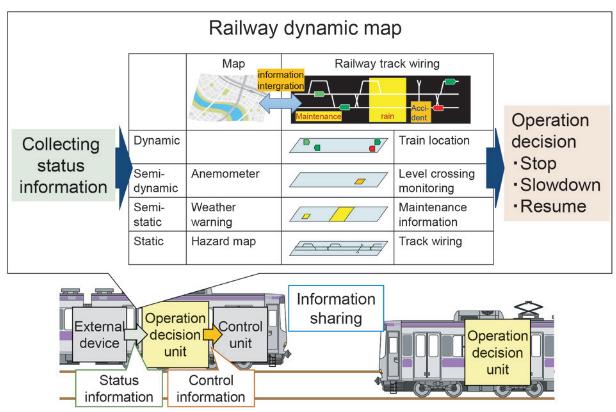

Fig. 4 Overview of railway dynamic map

sion of information to be referred to when using the distributed information, a list of information on trains in motion, existing facilities, and the source of disaster prevention information, respectively, are managed for each line segment (Fig. 5(a)).

By acquiring information from each source using this list of information sources, trains can register the situation in areas that they cannot directly recognize. Furthermore, this acquired information is superimposed on the information directly recognized by the train and used for decision making (Fig. 5(b)). For example, in the event of heavy rainfall, the possibility of slope collapse is recognized through hazard maps and weather information. In addition, information from the ground monitoring system, forward monitoring information from other trains, and information on actual passing results are combined to estimate whether or not the section is passable. By combining this condition information with the forward monitoring information provided by the train itself, a comprehensive judgment of operational risk can be made. On the ground side, the same facility management and status monitoring can be performed as before by acquiring the information distributed by each device.

The basic unit of information distribution is a decentralized configuration in which information is distributed to each device individually. In addition to a decentralized configuration, an intermediate device can also consolidate and redistribute some of the information or integrate them.

Based on the status information aggregated on the railway dynamic map of each train, the current position of the train, and the route of the train, the railway dynamic map is analyzed to see if there is any status information that affects the train's own running.

4. Implementation of railway dynamic map

4.1 Example of railway dynamic map

Based on these studies, maps and track map data were prepared for the in-house test tracks of the Railway Technical Research Institute. Then, the railway dynamic maps shown in Fig. 6 were created and the railway dynamic map simulator was developed to enable the placement of simulated trains. The underlying map information is based on map data provided by the Geospatial Information Authority of Japan (GSI) [9], overlaid with separately prepared track and other data.

In this simulator, wayside equipment failures, operating restrictions and obstructions can be set. When these are set, the information detected by each train is updated to detect operational restrictions that exist within a certain distance from the train.

Figure 7 shows examples of the information recognized by Train 1 and Train 2 in Fig. 6 when the hazard information shown in Fig. 6 is obtained. Train 1 has hazard information that affects its operation on the route, so that this information is shown in red in Fig. 7 and the train symbol in Fig. 6 is also red. Although Train 2 also recognizes this hazard information, because it is not on the route, the color of the status information in Fig. 7 does not change and the train symbol in Fig. 6 also remains light blue. Thus, it is possible to evaluate the impact on each train by combining the state information developed on the railway dynamic map and the route of the train.

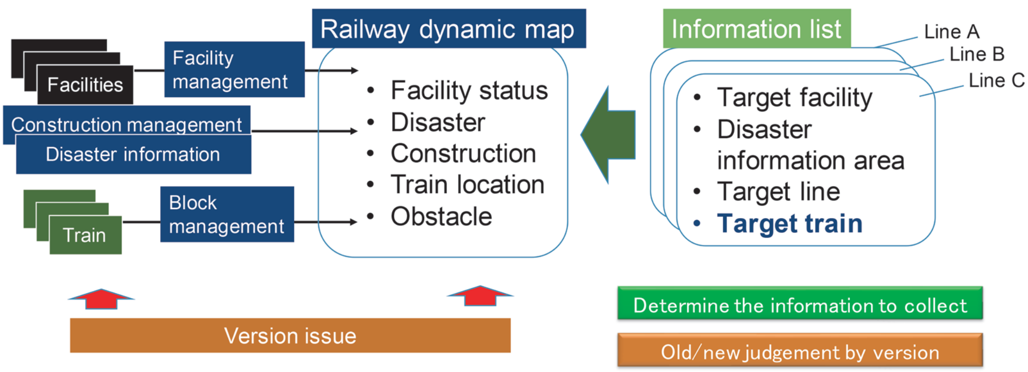

(a) Information management method

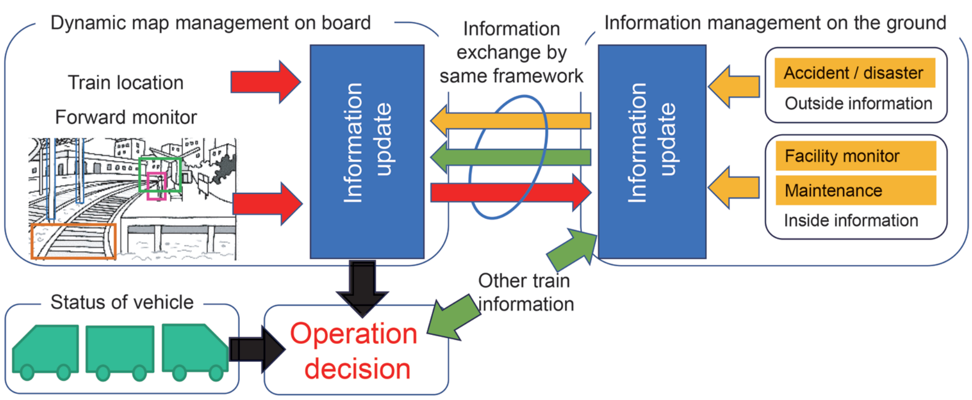

(b) Information sharing and streaming method for operation decision

Fig. 5 Information sharing and streaming method of railway dynamic map

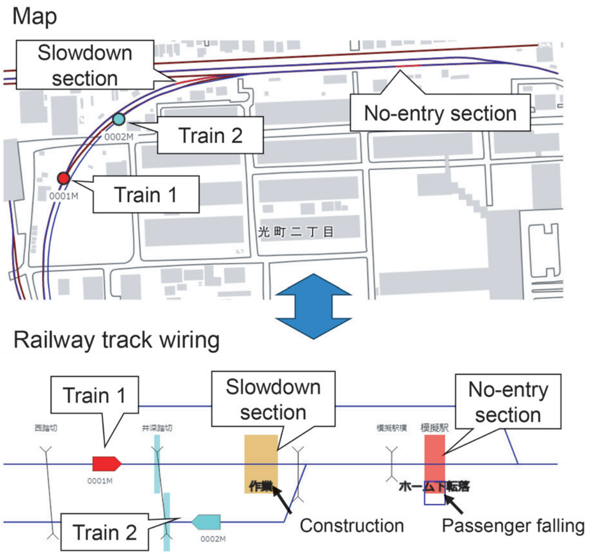

Fig. 6 Railway dynamic map (map and railway track wiring)

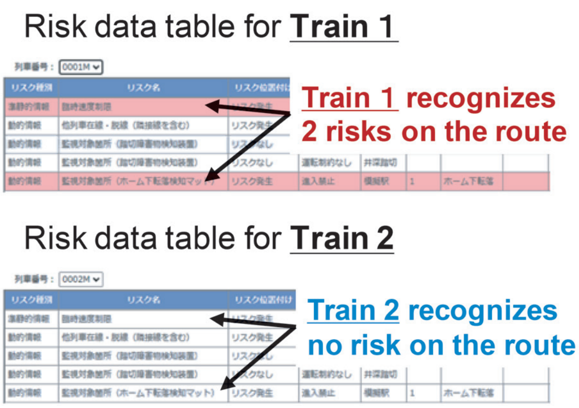

Fig. 7 Railway dynamic map (Example of hazard information update)

4.2 Application of the railway dynamic map to current operation

The railway dynamic map can also be applied to support the dispatcher and crews in operational decision-making in current operations. When a certain transport disruption occurs, the dispatcher currently collects information from various monitoring systems, and displays it on a whiteboard in the OCC to visualize. This creates a significant burden on the dispatcher. Using the railway dynamic map, it is possible to collect information on a single screen in a centralized operation, allowing the dispatcher to focus on operational decisions and to efficiently organize operations in the event of an abnormality (Fig. 8). In addition, by installing display units on trains and at stations, it is possible to facilitate the sharing of information between the dispatcher, crews and station staffs, and more accurate passenger guidance can also be achieved.

5. Conclusions

The authors studied automatic on-board operational decisions which is one of challenges of realizing autonomous train operation.

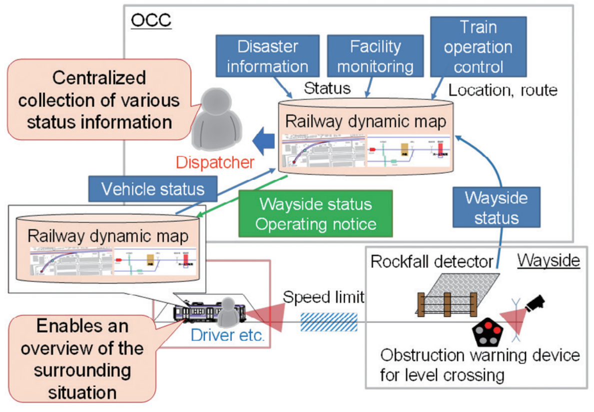

Fig. 8 Railway dynamic map (Example of hazard information update)

In this study, information about vehicle and wayside equipment condition, necessary for operational decisions, was used, and the railway dynamic map was developed as an information infrastructure to manage information about the state of operations.

Using the proposed railway dynamic map, it is possible to identify abnormal conditions affecting the train based on the position and planned route of each train, and to make appropriate operational decisions depending on operational conditions. It has also been shown that it is possible to provide this information to command staff and crew members to support them in making decisions in the context of current railway operations.

In the future, we will develop a train control interface for using this railway dynamic map and investigate methods for realizing more complex operational decisions.

References

[1] Aoyagi, T., "Development of ATS (Automatic Train Stop)-based automatic train operation system using FS-ATO," *Proceedings of STECH 2021*, IL-4, 2021.
[2] Fujita, H., Nomura, T., Aoyagi, T., Morita, S., "Development of Automatic Train Operation System Based on Intermittent Type ATP with Continuous Speed Checks," *Quarterly Report of RTRI*, Vol. 63, No. 3, pp. 187-192, 2022.
[3] Kawasaki, K., "Overview of Research and Development Activities Relating to Digitalization of Railway Operation Management and Future Outlook," *Quarterly Report of RTRI*, Vol. 61, No. 4, pp. 235-239, 2020.
[4] IEC 62267:2009 "Railway applications - Automated urban guided transport (AUGT) - Safety requirements," 2009.
[5] JIS E 3802 "Automated urban guided transport (AUGT) -Safety requirements," 2012.
[6] Study Group on Automatic Operation Technology for Railways, "2019 summary (main text)," https://www.mlit.go.jp/tetudo/tetudo_fr1_000058.html, accessed June 6, 2023.
[7] Shimada, H., Yamaguchi, A., Takada, H., Sato, K., "Implementation and Evaluation of Local Dynamic Map in Safety Driving Systems," *Journal of Transportation Technologies*, Vol. 5, No. 2, pp. 102-112, 2015.
[8] Ota, Y., Gion, A., Nishimoto, S., Sakurai, Y., "Operation risk assessment method based on information on wayside and vehicle conditions for autonomous train operation," *RTRI Report*, Vol. 38, No. 3, pp. 43-48, 2024. (in Japanese).

[9] Geospatial Information Authority of Japan, "GSI Tiles," https:// maps.gsi.go.jp/development/ichiran.html

Authors

Yuki OTA, Ph.D.
Assistant Senior Researcher, Train Control Systems Laboratory, Signalling and Operation Systems Technology Division
Research Areas: Train Control Systems, Automatic Train Control, Train Location Detection

Akihiro GION
Senior Researcher, Train Control Systems Laboratory, Signalling and Operation Systems Technology Division
Research Areas: Train Control Systems, Safety Information Transmission, General Purpose Device

Sho NISHIMOTO
Researcher, Train Control Systems Laboratory, Signalling and Operation Systems Technology Division
Research Areas: Train Control Systems

Yuki SAKURAI
Researcher, Train Control Systems Laboratory, Signalling and Operation Systems Technology Division
Research Areas: Train Control Systems

Effect of Structural Details of Beam-to-column Joint in RC Viaducts on Capacity

Yuki NAKATA **Ken WATANABE**
Concrete Structures Laboratory, Structures Technology Division

Toshiya TADOKORO
Structures Technology Division

RC beam-to-column joints in railway viaducts are designed to satisfy structural details. However, when overcrowded reinforcement arrangement measures are implemented at joints or high strength rebars are applied to members, a relationship between details of reinforcement arrangement and capacity of joint is required. In this study, we carried out cyclic loading tests and 3D FEM analyses to clarify this relationship. The results show that as the inside radius of the bend of longitudinal rebars decreases, the capacity of a joint decreases due to the reduction of compressive strut width, and that the ties in the joint have little effect on the capacity, although it increases the deformation performance.

Key words: *beam-to-column joint, RC viaduct, capacity, nonlinear finite element analysis, structural details*

1. Introduction

The beam-to-column joint of reinforced concrete (RC) viaducts does not require specific verification by complying with structural details such as the details of reinforcement arrangement and haunches shown in Fig. 1 [1, 2]. Such structural details have the advantage of simplifying the verification.

Structural details relating to joints have long been specified in design standards. One of the structural details of joints is that the number of ties in a joint must be the same as the ties in the plastic hinge of the columns [1]. The increase in seismic forces that must be considered in seismic design leads to increasing the number of ties in the plastic hinge of columns, so that the number of ties in the joints also increases. As a result, the reinforcement of joints has to be overcrowded. To address this issue, it is important to clarify the relationship between the ties in the joint and the capacity, etc.

In past earthquakes, damage has occurred at the joints between columns and middle beams whose dimensions are relatively small [3]. High-strength rebars such as SD490 and SD685 have been increasingly used for longitudinal reinforcement in recent years. However, since the dimensions of columns and beams become smaller due to the use of high-strength rebar, the joints also become smaller. In this case, since the capacity of the joint is expected to be relatively smaller than that of the members, a method of evaluating the capacity of the joint is required.

In this study, we aimed to clarify the effect of the ties in the joint and the inside radius of bends in the longitudinal rebars along the outside of the corner on the capacity. Specifically, we used experiments and nonlinear finite element analyses to understand the load-bearing mechanism of beam-to-column joints. Based on these results, we also verified the validity of the structural details of the joint.

2. Experimental evaluation of damage and capacity of joints

2.1 Experimental outline

Figure 2 and Table 1 show an outline of specimens. The specimens were reduced down by approximately 50% from the L-shaped joints used in typical railway viaducts. Both the horizontal and vertical members had a square cross section with a cross-sectional width of 500 mm and a cross-sectional height of 500 mm. The length from the support or loading point to the base of the member was 1,800 mm for both vertical and horizontal members. Both the vertical and horizontal members were supported by a pin structure. The material test results are shown in Table 1. SD490 was used for the longitudinal rebars so that the joint would fail first.

Four test specimens were prepared, with or without ties in the joint and with the different inside radius of bend r of the longitudinal rebars along the outside of the corner. No. 1 and No. 3 had ties placed in the joints (tie ratio $p_w = A_w/(b_w \cdot s_s) = 0.57\%$, A_w: total area of ties in section s_s, b_w: web width of the horizontal member, s_s: spacing of ties), while No. 2 and No. 4 did not have ties placed in the joints. The inside radius of the bend r was set to 10ϕ (ϕ: diameter of longitudinal rebars) as specified in the design standard for No. 1 and No. 2, and $r = 3\phi$ for No. 3 and No. 4. Semicircular hooks were used to fasten the inner longitudinal rebars, with the inside radius of bend r of 3.5ϕ.

The loading was carried out using the L-shaped frame shown in Fig. 2. A vertical jack was used to control the vertical displacement at the loading point to zero, while alternating positive and negative loads was applied in the horizontal direction. The side where the joint opens was subjected to positive loading, and the side where the

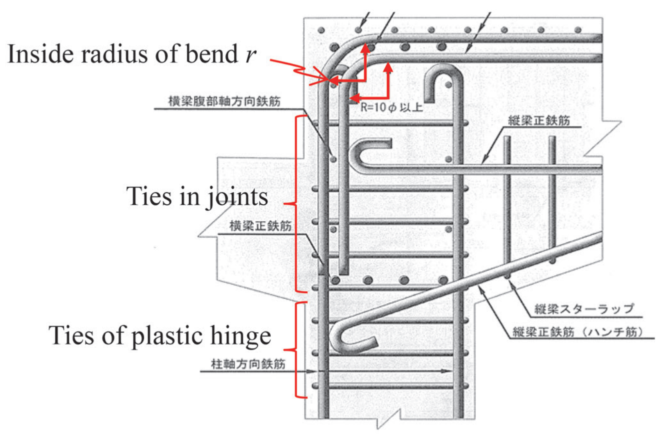

Fig. 1 Examples of structural details for joints [2]

joint closes was subjected to negative loading. The loading was repeated once when diagonal cracks appeared in the joint. After that, the displacements at which the longitudinal rebars of No. 1 yielded under positive and negative loading were set to $+1\delta_y$ (39.5 mm) and $-1\delta_y$ (−38.5 mm), respectively, and the loading was repeated three times at integer multiples of $\pm1\delta_y$. In addition, No. 2 to No. 4 also used the same $\pm1\delta_y$ as No. 1.

2.2 Experimental result

Figure 3 shows the relationship between horizontal load and horizontal displacement, and Fig. 4 shows the damage to the joints. Under positive loading, as the load increased, cracks initiated at the corners and propagated along the longitudinal rebars in the joint. Then, diagonal cracks occurred in the joint. Under negative loading, after the bending cracks occurred, diagonal cracks occurred in the joint. The order of crack initiation was similar for all specimens. The horizontal load and the location at which the main diagonal cracks occurred were roughly the same for all specimens. Figure 5 shows the displacement measured by a π gauge across the main diagonal cracks ① and ② shown in Fig. 4. Although the measured displacement includes microcracks and elastic displacement of the concrete around the main diagonal crack, it is thought that the width of the main diagonal crack accounts for most of the displacement. The results are also shown for the range up to $2\delta_y$, for which measurements were possible. Even with the ties in place, there was no significant difference in the measured displacement of diagonal cracks ① and ②, indicating little restraint by the ties.

The longitudinal rebars in No. 1 yielded under positive loading and negative loading: No. 2 under negative loading, and No. 3 under positive loading. In other cases, the longitudinal rebars did not yield, and load reduction occurred due to the opening of diagonal cracks in the joints, etc. In No. 1 and No. 3 where ties were placed in the joints, the ties near the diagonal cracks yielded before the maximum horizontal load P_{max} was reached. As can be seen from Fig. 3, r does not have a significant effect on P_{max} under positive loading, but P_{max} decreased as r became smaller under negative loading. As shown in Fig. 5, the presence or absence of ties in the joints does not have much effect on P_{max} because the restraint by the ties is small up to P_{max}. This fact results in improving deformation performance.

3. Effect of details of reinforcement arrangement on load-bearing mechanism and capacity

3.1 Analysis outline

Nonlinear finite element analysis is used to examine the effects of the load-bearing mechanism and details of reinforcement arrangement of the joints on capacity. Figure 6 shows the analysis model. The analysis was performed using the general-purpose finite element analysis code, DIANA ver. 10.2, to create a three-dimensional model. The concrete was treated as solid elements, and the rebar as embedded rebar elements where only the stiffness in the axial direction were considered. The curve of the bent anchor point of the longitudinal rebars was reproduced by dividing the elements

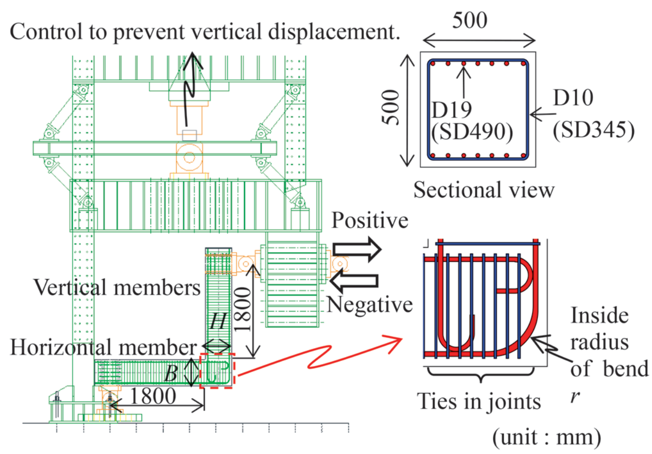

Fig. 2 Specimen and loading outline

Table 1 Outline of specimens

(a) List of specimens

Specimens	Concrete			Beam-to-column Joint			Longitudinal rebars				Column and beam ties		
	f'_c (N/mm²)	f_t (N/mm²)	E_c (N/mm²)	Diameter, Spacing (mm)	p_w ※1 (%)	r	Diameter	f_{sy} (N/mm²)	E_s (N/mm²)	p_t (%)	Diameter, Spacing (mm)	f_{wy} (N/mm²)	p_w (%)
No.1	26.1	2.5	24.5	D10, 50	0.57	10ϕ	D19	530	179	0.89	D10, 50	367	0.57
No.2	27.0	2.6	25.9	—	0	10ϕ							
No.3	21.9	1.9	24.8	D10, 50	0.57	3ϕ		527	195		D16, 50	370	1.59
No.4	23.9	2.1	24.5	—	0	3ϕ		530	179		D10, 50	367	0.57

f'_c : Compressive strength of concrete, f_t : Splitting tensile strength of concrete, E_c, E_s : Young's modulus, f_{sy}, f_{wy} : Yield strength, p_w :Tie ratio, r : Inside radius of bend, p_t : Tensile reinforcement ratio, A_w : Total area of ties in section s_s, b_w : Web width of the horizontal member, s_s : Spacing of ties
※1 : $p_w=A_w/(b_w \cdot s_s)$

(b) Method combination of concrete

Specimens	Maximum size of coarse aggregate(mm)	W/C	Fine aggregate ratio (%)	Unit amount (kg/m³)				
				Water W	Cement C	Fine aggregate	Coarse aggregate	AE water reducing agent
No.1	13	73.5	53.2	202	275	906	824	2.75
No.2~4	13	75.6	54.6	202	267	934	806	2.67

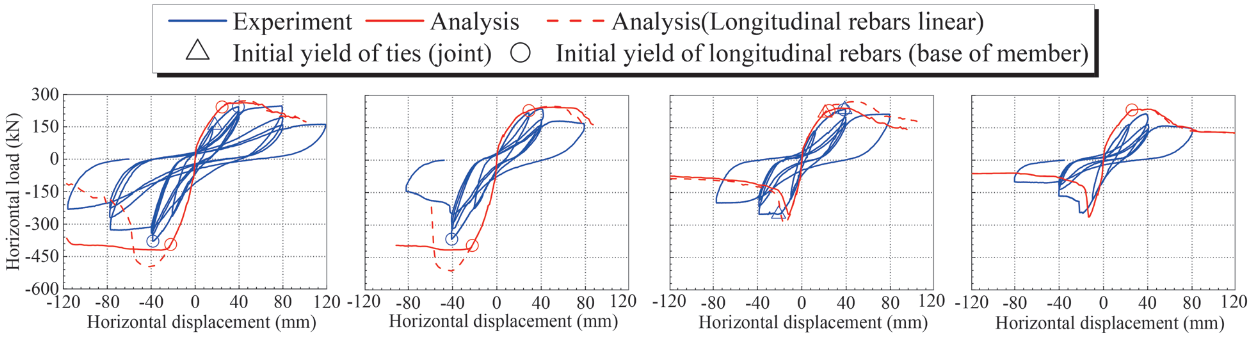

(a) No.1(p_w=0.57%, r=10ϕ) (b) No.2(p_w=0%, r=10ϕ) (c) No.3(p_w=0.57%, r=3ϕ) (d) No.4(p_w=0%, r=3ϕ)

Fig. 3 Relationship between horizontal load and horizontal displacement

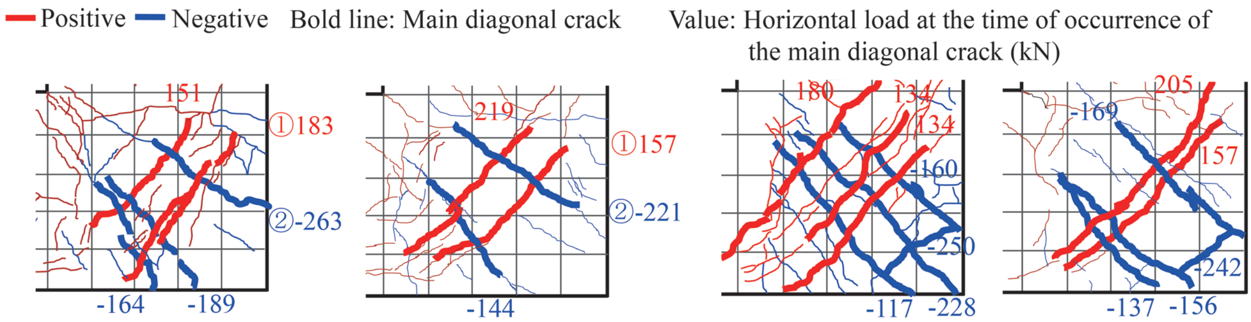

(a) No.1(p_w=0.57%, r=10ϕ) (b) No.2(p_w=0%, r=10ϕ) (c) No.3(p_w=0.57%, r=3ϕ) (d) No.4(p_w=0%, r=3ϕ)

Fig. 4 Damage to the joint (just before concrete spalling occurs)

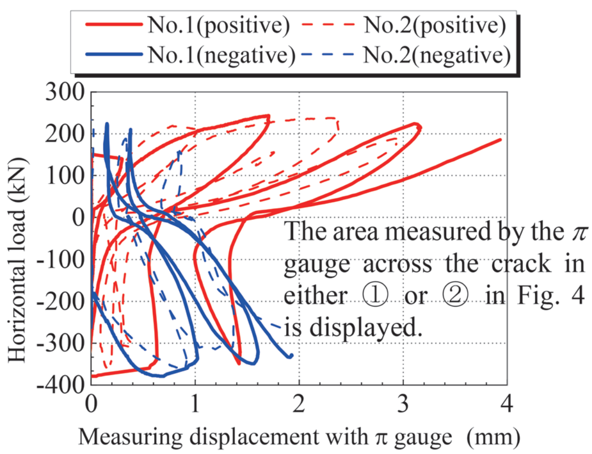

Fig. 5 Measuring displacement with a π gauge

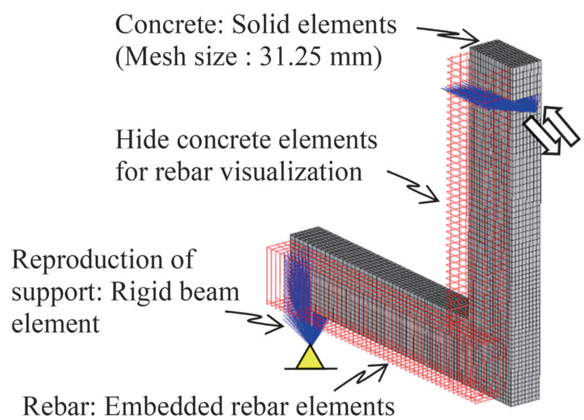

Fig. 6 Analysis model

into approximately 10 mm intervals. In order to reproduce the pin support used in the experiment, the center of rotation of the pin support and the solid elements of the supports of the horizontal and vertical members were connected by rigid beam elements. For concrete, a parabolic model was used on the compression side, and the Hordijk model [4] was used on the tension side. The fracture energy of concrete was calculated based on the design standard [1] and the formula proposed by Nakamura et al. [5]. The cracks were treated as fixed cracks, and the Al-Mahaidi model [6] was applied to the transmission of shear force at the crack surfaces. The rebars were of bi-linear type, and the stiffness after yielding was set to 1/100 of the initial stiffness. In order to take into account the effect of a small cover thickness, the bond model between the rebars and concrete was based on the bond stress-slip relationship proposed by Shima et al. [7], in which the bond stress was reduced to 40%. In the analysis, monotonic loading was performed in one direction on both the positive side (opening side) and the negative side (closing side).

3.2 Reproducing experimental results

Figure 3 also shows the relationship between horizontal load and horizontal displacement obtained from the analysis. Although the analysis tends to overestimate the stiffness up to P_{max}, it generally reproduces the experimental results. In addition, the figure also shows the analysis results in which the stress-strain relationship of the longitudinal rebars is linear. In the loading direction in which the longitudinal rebars at the base of the horizontal and vertical members yield, P_{max} increases by linearizing the stress-strain relationship of the longitudinal rebars because it is affected by yielding.

Figure 7 shows the distribution of maximum principal strain at P_{max} for No. 1 and No. 2 (r =10ϕ). The analysis was also able to reproduce the flexural cracks and the main diagonal cracks that occurred in the joints observed in the experiment. It has been separately confirmed that the analysis was able to generally reproduce the strain distribution in the longitudinal rebars and the ties in the joints in the experiment [8].

It was shown that the damage characteristics and capacity of the joints could be reproduced by nonlinear finite element analysis. In the following, we will use nonlinear finite element analysis to examine the effects of details of reinforcement arrangement on the load-bearing mechanism and capacity.

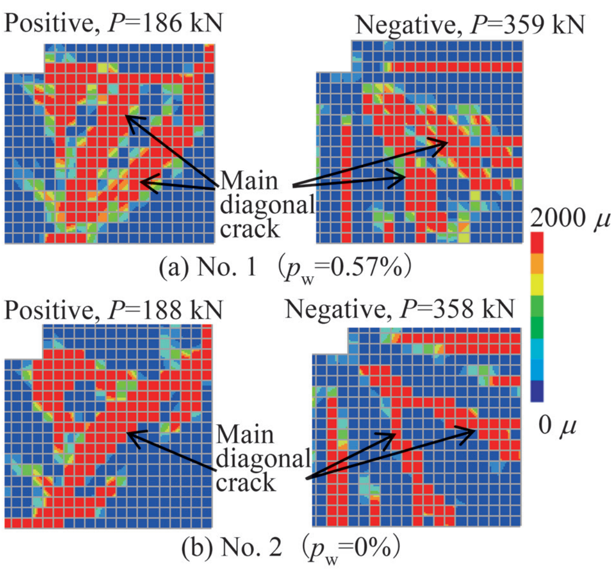

Fig. 7 Maximum principal strain distribution (r=10φ)

3.3 Effect of ties in joints

Here, in order to verify the capacity of the joint, the stress-strain relationship of the longitudinal rebars was assumed to be linear so that the horizontal and vertical members would not yield. Table 2 shows the analysis parameters. The analysis was also performed for the cases where p_w=0.29%, r=5, 7ϕ, and the ratio of the joint height H to width B (H/B) =1.6 as shown in Fig. 2, as well as for T-shaped [9] and cross-shaped joints. The T-shaped and cross-shaped joints are reproduced using the same cross sections and lengths of members as the L-shaped joints. In addition, in order to examine the effects of the ties alone, the compressive strength of the concrete was set to 27 N/mm², the tensile strength to 2.6 N/mm², the Young's modulus to 25.9 kN/mm², the yield strength of the ties to 345 N/mm², and the Young's modulus of the rebars to 200 N/mm².

Figure 8 shows the effect of p_w on P_{max}. The negative loading of r =7 and 10ϕ at H/B =1.6 for the L-shaped joint are not shown in the figure because the member occurred flexural compression failure. When H/B =1.6 for the L-type, P_{max} tends to increase slightly as p_w increases. The ratio of P_{max} at p_w =0.29 or 0.57% to P_{max} at p_w =0% was 1.03 on average at H/B =1.0 and 1.11 on average at H/B =1.6.

Figures 9 and 10 show the minimum principal stress distribution. Under positive loading, the compression struts were formed to con-

Table 2 Analysis parameters

Specimen shape※1	H/B	Beam-to-column joint tie ratio p_w (%)	Inside radius of bend r※2
L-shape T-shape Cross-shape	1.0 1.6	0.00 0.29 0.57	3ϕ 5ϕ 7ϕ 10ϕ

H: Height of joint, B: Width of joint
※1: L-shaped joints carry both positive and negative loads
※2: Longitudinal rebar along the outer side of the corner of L-shape

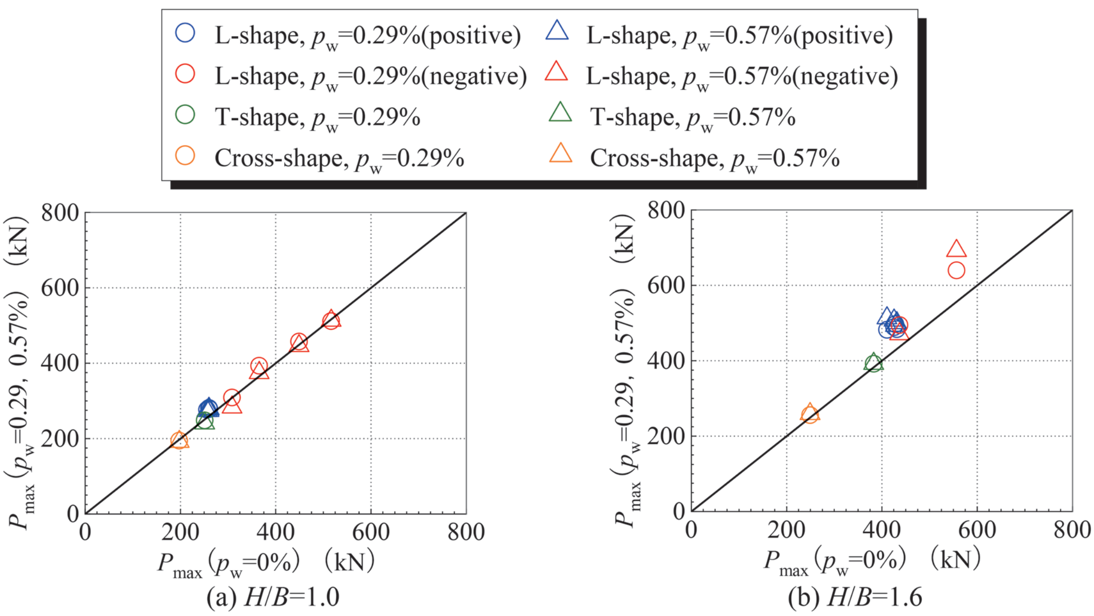

Fig. 8 Effect of ties in joints (Analysis)

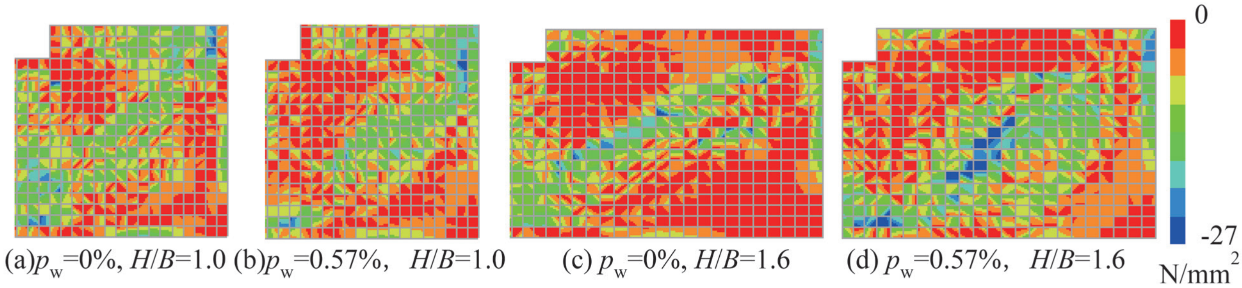

Fig. 9 Minimum principal stress distribution (r=10φ, positive loading, P_{max})

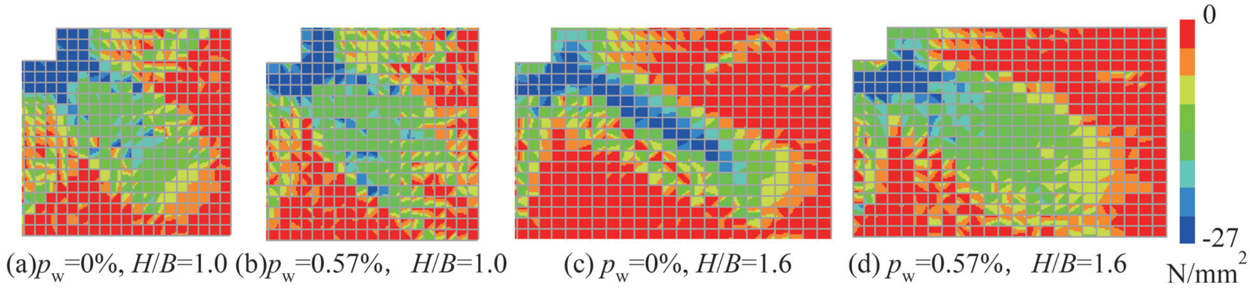

Fig. 10 Minimum principal stress distribution (r=10φ, negative loading, P_{max})

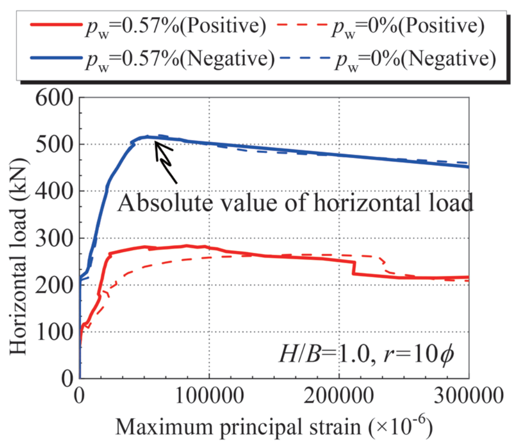

Fig. 11 History of maximum principal strain

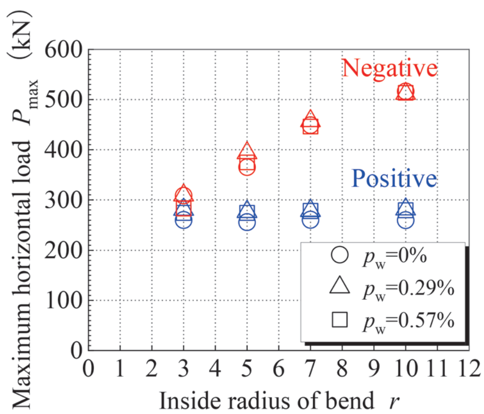

Fig. 12 Effect of inside radius of bend r (Analysis, H/B=1.0)

nect the flexural compression edges of the horizontal and vertical members. On the other hand, under negative loading, the compression struts were formed to connect the flexural compression edges of the horizontal and vertical members with the inside radius of bend. When H/B =1.0, no difference is observed in the shape of the compressed strut even if p_w increases. However, when H/B =1.6, the width of the compression strut increased slightly with increasing p_w.

Figure 11 shows the history of the maximum value of the maximum principal strain of concrete, focusing on the element where the main diagonal crack in the joint shown in Fig. 7 occurred. The horizontal load under negative loading in Fig. 11 is shown as an absolute value (positive). When p_w increases, the maximum principal strain tends to be suppressed at positive loading, but no significant difference was observed in the maximum principal strain during negative loading.

3.4 Effect of the inside radius of bend

Figure 12 shows the effect of r on P_{max}. The analysis conditions are the same as those in Section 3.3. P_{max} under positive loading was hardly affected by r, but P_{max} under negative loading decreased as r became smaller.

Figures 13 and 14 show the minimum principal stress distribution. Under positive loading, no difference was observed in the compression struts even if r changed. On the other hand, under negative loading, the smaller the value of r, the smaller the width of the compression strut. This is because the load-bearing mechanism under positive loading is such that the compression struts are formed to connect the flexural compression edges of the vertical and horizontal members, so r does not directly contribute to the compression struts and does not affect P_{max}.

Under negative loading, compression struts are formed to connect the flexural compression edges of the vertical and horizontal members with the inside radius of bend, so that the inside radius of bend acts as a reaction force for the compression struts. Therefore, it is thought that the width of the compression struts depends on r and has a significant effect on P_{max}.

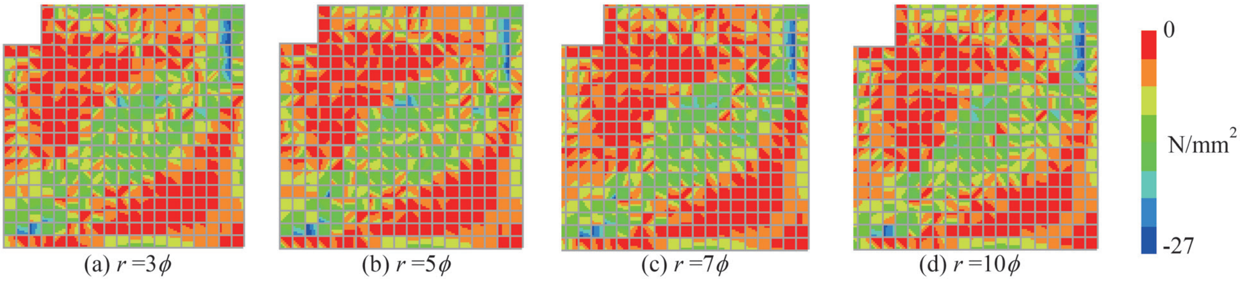

Fig. 13 Minimum principal stress distribution (p_w=0.29%, H/B=1.0, positive loading, P_{max})

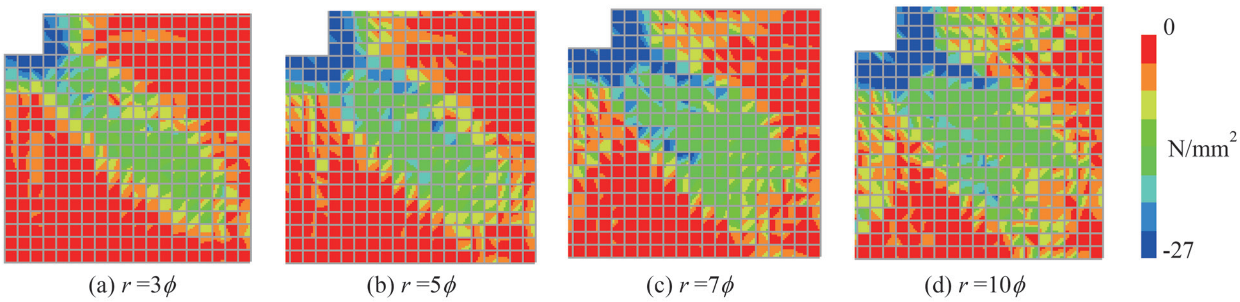

Fig. 14 Minimum principal stress distribution (p_w=0.29%, H/B=1.0, negative loading, P_{max})

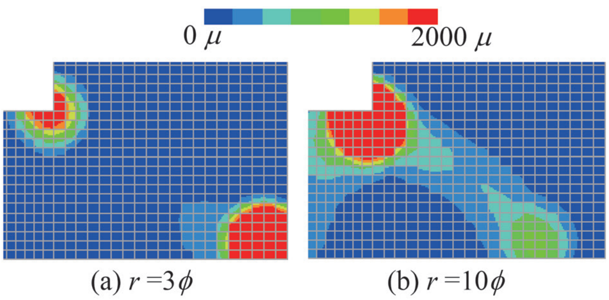

Fig. 15 Distribution of the average normalized accumulated strain energy

4. Structural details of joints

4.1 Ties in joints

Structural details, such as the requirement that the number of ties in joints should be the same as that in the plastic hinge of the columns [1], were introduced in Design Standards for Railway Structures and Commentary (Concrete Structures) enacted in 1992, and were set based on experimental studies [10] and the number of rebars required at the time. Because joints are difficult to repair, it is common to first induce damage to adjacent members such as columns and beams to prevent major damage to the joints. In this type of design concept, it is necessary to ensure a specified capacity and stiffness without allowing deformation beyond the capacity of the joint. However, considering that the ties in the joints did not have a significant effect on P_{max} and that the number of ties in the joints in the study where structural details were set [10], there is a possibility that excessive ties were placed.

Therefore, it is proposed that the number of ties in the joints should be equal to or greater than the number of shear reinforcement bars in the columns required against shear force. This is based on the fact that in many cases the shear reinforcement ratio of the columns is about 1/2 to 2/3 of the tie ratio placed in the plastic hinges, in which case the number of ties in the joint will be about the same as that assumed at the time of setting. It is also based on the fact that the greater the flexural capacity and shear capacity required of the columns, the greater the number of shear reinforcement bars in the columns will be, and that this number is correlated with the cross-sectional force introduced from the columns to the joints. However, the ties at the joints act as additional reinforcement and also contribute to the anchoring of longitudinal rebars in the columns and beams. Furthermore, the Building Code [11] indicates that the ties in joints contribute to maintaining the stiffness of the joints and that the concrete needs to be restrained to retain axial force. Based on this, it is considered advisable to place ties with a shear reinforcement ratio of 0.3% or more of the column in joints.

4.2 Inside radius of bend of the longitudinal rebars along the outer side of the corner

The design standard requires that the inside radius of a bend r of longitudinal rebars along the outer side of the corner should be 10ϕ or more. Here we verify the validity of r. Figure 15 shows the distribution of the averaged normalized accumulated strain energy $\overline{W}_n$ [12]. $\overline{W}_n$ is an index that represents compressive damage to concrete, and when it reaches 1500 μ to 2000 μ, it means that the concrete will suffer compression failure. In addition, the figure shows the results for H/B=1.6, taking into account the ratio of typical cross-sectional dimensions of columns and beams. In the case of r =10ϕ, the results indicated that the horizontal members were likely to have suffered flexural compression failure, but the compressive damage at the inside radius of the bend was small. On the other hand, when r=3ϕ, compressive damage at the inside radius of the bend was predominant. As r was reduced from 10ϕ, compressive damage at the inside radius of the bend gradually became more predominant, but by keeping r at around 10ϕ or more as in the past, it was possible to suppress bearing failure at the inside radius of the bend.

In this paper, the effects of the load-bearing mechanism and details of reinforcement arrangement of the joint on P_{max} were clarified. If details of reinforcement arrangement of joints assumed when setting the structural details or the size of the joints are significantly different from those in the past by using high-strength longitudinal rebars, it is advisable to verify them using nonlinear finite element analysis and material damage index [12].

5. Conclusions

(1) It was found that the ties in the joint contribute to improving the deformation performance of the joint but have no significant effect on the capacity.
(2) It was found that the inside radius of bends in the outer longitudinal rebars has little effect on the capacity of the joint in the opening direction of the joint, but a smaller inside radius of bends reduces the capacity of the joint in the closing direction.
(3) It was found that the load-bearing mechanism is such that the compression struts connect the flexural compression edges of the horizontal and vertical members in the opening direction of the joint and connect the flexural compression edges of the horizontal and vertical members with the inside radius of bends in the closing direction. It was also clarified that the inside radius of a bend has a large effect on the width of the compression struts in the closing direction.
(4) The structural details of the joints were examined. It was proposed that the number of ties in joints should be equal to or greater than the number of shear reinforcement bars in the columns. This would reduce the number of ties compared to conventional methods, and prevent over-dense reinforcement. It was also confirmed that bearing failure at the inside radius of a bend could be suppressed by keeping the inside radius of a bend of the longitudinal rebars along the outer side of the corner at 10ϕ or more as in conventional methods.

References

[1] Railway Technical Research Institute, *Design Standard for Railway Structures and commentary* (*Concrete Structures*), Maruzen, 2004 (in Japanese).
[2] Railway Technical Research Institute, *Design Standard for Railway Structures and commentary* (*Concrete Structures*) *Reinforcement arrangement guide*, Railway Technical Research Institute, 2005 (in Japanese).
[3] East Japan Railway Company Structural Technology Center, *Special feature "the Pacific coast of Tohoku Earthquake and railway structures,"* SED, Vol. 37, 2011 (in Japanese).
[4] Hordijk, A. D., "Local Approach to Fatigue of Concrete," Delft University of Technology, 1991.
[5] Nakamura, H. and Higai, T., "Compressive fracture energy and fracture zone length of concrete, seminar on post-peak behavior of RC structures subjected to seismic loads," *JCI-C51E*, Vol. 2, pp. 259-272, 1999.
[6] Al-Mahaidi, R. S. H., "Nonlinear Finite Element Analysis of Reinforced Concrete Deep Members," Tech.Rep. 79-1, Department of Structural Engineering, Cornell University, 1979.
[7] Shima, H., Chou, L. and Okamura, H., "Bond-slip-strain relationship of deformed bars embedded in massive concrete," *Journal of Japan Society of Civil Engineers*, Vol. 378/V-6, pp. 165-174, 1987 (in Japanese).
[8] Kusano, H., Nakata, Y., Tadokoro, T. and Abo, T., "Influence of the specifications of reinforcement arrangement in the joint on the failure mode of L-shaped RC beam-column joint," *The 15th Japan Earthquake Engineering Symposium*, pp. 51-60, 2018 (in Japanese).
[9] Nishimura, S., Nakata, Y., Watanabe, K. and Tadokoro, T., "Damage process and analytical evaluation of T-shaped beam-to-column joint with equal cross-sectional heights," *Japan Society of Civil Engineers 2020 Annual Meeting*, V-602, 2018 (in Japanese).
[10] Watanabe, T. and Matsumoto, N., "Study on Seismic Design of Reinforced Concrete Railway Structures (Part 2) -Strength of Beam-Column Joint and its Effect on Toughness of Members-," *RTRI Report*, Vol. 5, No. 9, pp. 21-30, 1991 (in Japanese).
[11] Architectural Institute of Japan, *Design guidelines for earthquake resistant reinforced concrete buildings based on inelastic displacement concept*, 1999 (in Japanese).
[12] Japan Society of Civil Engineers, *Standard Specifications for Concrete Structures -2017 Design*, 2018 (in Japanese).

Authors

Yuki NAKATA, Doctor of Engineering
Senior Researcher, Concrete Structure Laboratory, Structures Technology Division
Research Areas: Concrete Structures

Ken WATANABE, Doctor of Philosophy
Senior Chief Researcher, Head of Concrete Structure Laboratory, Structures Technology Division
Research Areas: Concrete Structures

Toshiya TADOKORO, Doctor of Engineering
Director, Head of Structures Technology Division
Research Areas: Concrete Structures

Nighttime Rail Temperature Prediction Method in Consideration of Radiant Heat from Surrounding Geographical Features

Fumihiro URAKAWA **Tsutomu WATANABE**
Track Dynamics Laboratory, Railway Dynamics Division

This study proposed a new method capable of predicting the rail temperature distribution in nighttime at intervals of about 1 m by modeling the radiant heat of rail in detail using digital surface model (DSM) and meteorological data. To verify its prediction accuracy, the distribution of rail temperature and radiant heat were measured on a real track. As a result, the minimum rail temperature was about 2°C higher at the measurement points near buildings compared with that at other points due to strong radiant heat. We also confirmed that the proposed method can accurately reproduce the actual rail temperature distribution in nighttime.

Key words: *rail temperature prediction, track buckling, heat balance, GIS*

1. Introduction

While long rails have many advantages such as improved running safety, reduced noise and vibration, and improved ride comfort, they also lose the ability to absorb rail expansion and contraction at joints. Therefore, when the rail temperature rises in summer, the risk of track buckling, where the rail track overhangs in the horizontal direction, increases due to the compressive rail axial force. On the other hand, tensile rail axial forces due to lower rail temperatures in winter cause rail breakage and increased rail gaps in the event of rail breakage. Both are significant events that can lead to derailment accidents. However, with growing concerns about rising railroad temperatures due to global warming, ensuring safety against track buckling and developing labor-saving management measures in a society with a declining population, have both become urgent issues. For continuous welded rail sections, the rail axial force in compression at rail temperature T_R is calculated from (1).

$$P_R = EA\beta(T_R - T_0) + \Delta P \quad (1)$$

where E, A, and β are the Young's modulus, cross-sectional area, and linear expansion coefficient of rails; T_0: fastening-down temperature (the temperature measured when rails are installed [1, 2]); and ΔP: additional axial force caused by rail creeping (movement in the longitudinal direction) and work at low temperatures [1].

In Japan, before the summer season, when the rail temperature is high, the degree of safety against buckling is determined by checking the maximum axial force generated which is determined by substituting the expected maximum rail temperature during the summer season into T_R in (1) against the buckling capacity calculated from the track stiffness and geometry. Depending on the results of the evaluation, the following measures are taken: addition of crushed stone to the ballast layer and track ballast trimming, re-stressing of continuous welded rail (adjusting rail creep to an appropriate value), and special track patrols in summer. Special track patrols are carried out to visually check the condition of the track when the rail temperature exceeds the control value (around 50°C). Under the recent thermal environment, special summer patrols are required almost every sunny day during the summer, which is labor intensive. As is clear from (1), a high fastening-down temperature, T_0, reduces the rail axial force at high temperatures, but increases the tensile rail axial force at low temperatures. Therefore, the upper limit of the fastening-down temperature, T_0, is determined from the expected minimum rail temperature in winter, and T_0 is generally set at 25°C to 30°C in consideration of the risks mentioned at the beginning of this paper.

It is therefore important to predict rail temperature not only at high temperatures but also at low temperatures to prevent track buckling. While several detailed prediction methods have been proposed for the former [3-6], simple predictions based on air temperature have been used for the latter. It is easy to expect that the minimum rail temperature will vary greatly depending on climatic conditions in different regions and at different elevations. It has also been reported that nighttime rail temperatures vary due to radiant heat from trees and other features [7]. In practice, it is difficult to determine the changes in rail temperature associated with the above factors, so the expected minimum rail temperature is currently set uniformly on a line-by-line basis. By quantitatively predicting the distribution of rail temperature in the longitudinal direction of the track, taking into account the above factors, and optimizing the fastening-down temperature and joint gap according to the predicted minimum rail temperature, we believe that safety against track buckling and labor-saving management can be achieved simultaneously.

The highest rail temperatures are recorded during the daytime in summer and the lowest during the nighttime in winter. In the field of road temperature control, the temperature of the road surface is predicted by calculating the heat absorbed by solar radiation (short wave radiation from the sun) and long wave radiation (hereinafter referred to as "radiant heat") from the atmosphere and surrounding geographical features (the ground, buildings, trees, etc.), considering their relative angle to the road surface. In reference [3], we have developed a method for predicting rail temperature by applying the evaluation method of solar radiation in previous studies [8] to a rail heat balance model and by analyzing heat transfer in the longitudinal direction of the rail. In the rail temperature prediction model in reference [3], the rail temperature during the daytime, when solar radiation is dominant, was accurately reproduced in the analysis by modeling solar radiation and the three-dimensional shape of the rail that receives solar radiation. On the other hand, for nighttime, when radiant heat dominates, the analyzed rail temperature was lower than the actual value because the radiant heat from surrounding objects was simply modeled as described below. In this paper, we develop a mathematical model to predict rail temperature by precisely calculating the radiant heat irradiated to the rail from elevation data including the height of surrounding objects ("DSM; Digital Surface Model") and the temperature of surrounding objects. Furthermore, rail temperature and radiant heat were measured on a real track and compared with the analytical results to verify the validity and accuracy of the proposed method. The model developed in Reference [3] is referred to as the "daytime rail temperature prediction model" and the model developed in this paper is referred to as the "nighttime rail temperature prediction model.

2. Nighttime rail temperature prediction model

2.1 Definition of coordinate system

In this chapter, the time is t, the position in the longitudinal direction of the rail is l, and the circumferential position in the cross-section of the rail is k. For the three-dimensional Cartesian coordinate system, the x-axis is used for west to east, the y-axis for south to north, and the z-axis for vertical upward direction, and their positions are denoted by $\{\boldsymbol{X}\}(=\{x,y,z\}^{\mathrm{T}})$. The azimuth angle on the xy plane is denoted by ψ, and the elevation angle by θ.

2.2 Model overview

Figure 1 shows the calculation flow for nighttime rail temperature prediction. First, the heat flow, $Q_{\mathrm{IN}}(l,t)$, absorbed by the rail is calculated from GIS (Geographic Information System) data and meteorological conditions. Then, after specifying the initial rail temperature, the heat flow, $Q_{\mathrm{OUT}}(l,t)$, discharged by the rail is calculated from the rail temperature, and the rail temperature at time $t+\Delta t$ is calculated by heat conduction analysis. These are repeated until an arbitrary time, t_N, to obtain the rail temperature, $T_{\mathrm{R}}(l,t)$, from t_0 to t_N at l. This calculation flow is the same as the daytime rail temperature prediction model, but the modeling method for the radiant heat received by the rail (Fig. 2(a)) is different. In the daytime rail temperature prediction model, when calculating the solar radiation received by the rail, the geographical features surrounding the rail are modeled by DSM, and the shielding of solar radiation by the geographical features is taken into account [3]. On the other hand, the radiant heat from the ground is calculated by assuming that the ground is a horizontal surface with no geographical features. This means that the radiant heat from geographical features and the shielding of radiant heat from the atmosphere and the ground by geographical features are not taken into account (Fig. 2(b)). Such a simplified modeling approach was a cause of error in the prediction of rail temperatures at night. Therefore, in order to reproduce the actual thermal environment (Fig. 2(a)) in the analysis, an advanced modeling method (Fig. 2(c)) was applied to the nighttime rail temperature prediction model, which takes into account the radiant heat from the geographical features and the shielding of the radiant heat from the atmosphere and the ground by the geographical features using DSM. Solar radiation is zero in the nighttime rail temperature prediction model.

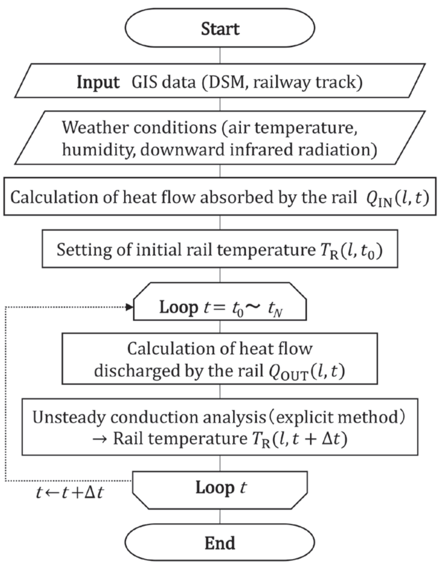

Fig. 1 Calculation flow for nighttime rail temperature prediction

2.3 Analytical mesh creation based on GIS data

2.3.1 Elements of geographic features based on DSM raster data

Raster data are one of the common data formats for expressing elevation in GIS, in which cells are arranged in a grid pattern, and one value is stored in each cell. As shown in Fig. 3, a quadrangle [ix, iy] is created from the four nodes of the DSM raster data by assigning node numbers of ix (= 1, 2,...) in the x direction and iy (= 1, 2,...) in the y direction. Furthermore, to simplify the formula for radiant heat described below, [ix, iy] is divided into two triangle elements, a and b, with the elements as planes. Nodes 0, 1, and 2 of triangle a are nodes (ix, iy), (ix + 1, iy), and (ix, iy+1), and nodes 0, 1, and 2 of triangle b are nodes (ix+1, iy+1), (ix+1, iy), and (ix, iy+1).

2.3.2 Modeling of three-dimensional rail geometry

As in Ref. [3], nodes for heat conduction analysis are placed at intervals of about 1 m along the GIS data of the rail track, and virtual rail cross sections (virtual cross sections) are added around the nodes to simulate the three-dimensional shape of the rail as a set of inclined planes (Fig. 3). Using this virtual cross-section, the shielding of radiant heat from the surroundings to the rail surface by other rail surfaces and the relative angles between the radiant heat and the rail surface are calculated and these are reflected in the heat absorp-

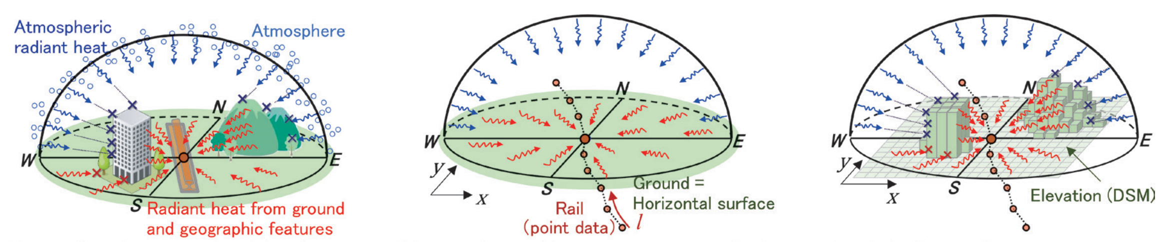

(a) Radiant heat received by the actual rail (b) Daytime rail temperature prediction model (c) Nighttime rail temperature prediction model

Fig. 2 Calculation model of radiant heat

tion. Compared with previous studies [6], this method enables the calculation of rail temperature distribution over a wide area of about 100 km, while ensuring the accuracy of the rail geometry reproduction and significantly reducing the calculation cost.

2.4 Radiant heat from the geographical features received by the rail

2.4.1 Identification of elements where radiant heat reaches the rail

First, as shown in Fig. 4(a), the nodes (the center of the raster) are extracted in the direction ψ as seen from the rail. Secondly, as shown in Fig. 4(b), the elements that include the node whose elevation angle θ_j as seen from the rail satisfies (2) (red point in Fig. 4(b)) and its rail-side node are the elements where radiant heat reaches the rail. This is done for all orientations ($0 \leq \psi \leq 2\pi$).

$$\theta_j \geq \max\{\theta_j\left(D < D_{(ix,iy)}\right)\} \tag{2}$$

2.4.2 Formulation of radiant heat from geotechnical features

Consider the radiant heat, q_{jk}, that the surface k on the rail surface receives from triangular element (geographic feature) j, as shown in Fig. 5. Assuming that the surface k is sufficiently small compared to the element j that the effect of its location on the surface k can be neglected, q_{jk} can be expressed by (3).

$$q_{jk} = \frac{A_k}{\pi}\sigma\cos\phi_k \int \varepsilon_j {T_j}^4 \frac{\cos\phi_j}{R^2} \mathrm{d}A_j \tag{3}$$

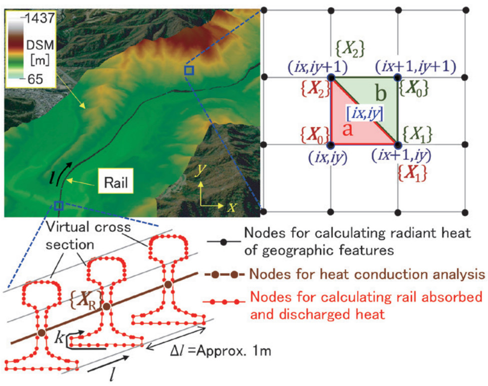

Fig. 3 Analytical mesh based on GIS data

where A_j and A_k are the areas of element j and surface k. ε_j is the emissivity of element j. σ is Stefan—Boltzmann constant. T_j is the absolute temperature of element j. ϕ_k and ϕ_j are the angles formed by the line segment connecting surface k and element j and the normal vector $\vec{n_k}$ and $\vec{n_j}$. R is the length of the line segment connecting surface k and a point on element j.

Vectors, $\vec{e_1}$ and $\vec{e_2}$, shown in Fig. 5 represent two sides of the triangle element j defined by (4). The vector $\vec{r}$ from the rail to a point on element j can be expressed in (5) using $\vec{e_1}$ and $\vec{e_2}$.

$$\vec{e_1} := \{\boldsymbol{X}_1\} - \{\boldsymbol{X}_0\}, \quad \vec{e_2} := \{\boldsymbol{X}_2\} - \{\boldsymbol{X}_0\} \tag{4}$$

$$\vec{r} = s_1\vec{e_1} + s_2\vec{e_2} + \{\boldsymbol{X}_0\} - \{\boldsymbol{X}_k\} \tag{5a}$$

$$0 \leq s_1 \leq 1, \quad 0 \leq s_2 \leq 1, \quad 0 \leq s_1 + s_2 \leq 1 \tag{5b}$$

where $\{\boldsymbol{X}_0\}$, $\{\boldsymbol{X}_1\}$, and $\{\boldsymbol{X}_2\}$ are the nodes 0, 1, and 2 of the triangle element. $\{\boldsymbol{X}_k\}$ is the coordinate of the center of surface k. Assuming that emissivity and temperature are uniform inside element j, (3) can be transformed into (6) using the vectors in (4) and (5).

$$q_{jk} = \frac{A_k}{\pi}\sigma\cos\phi_k\left(2A_j\varepsilon_j{T_j}^4\right)\int_0^1\int_0^{1-s_1}\frac{\cos\phi_j}{|\vec{r}|^2}\mathrm{d}s_2\mathrm{d}s_1 \tag{6}$$

The area of element j, A_j, can be calculated from (7), the normal vector $\vec{n_j}$ can be calculated from (8) , and $\cos\phi_j$ can be calculated from (9). The normal vector of surface k, $\vec{n_k}$, is obtained from the rail azimuth and shape data, and $\cos\phi_k$ is obtained from (10).

$$A_j = \frac{1}{2}\sqrt{|\vec{e_1}|^2|\vec{e_2}|^2 - (\vec{e_1}\cdot\vec{e_2})^2} \tag{7}$$

$$\vec{n_j} = \frac{\vec{e_1}\times\vec{e_2}}{|\vec{e_1}\times\vec{e_2}|} \tag{8}$$

$$\cos\phi_j = \frac{\vec{n_j}\cdot\vec{p}}{|\vec{n_j}||\vec{p}|} \tag{9}$$

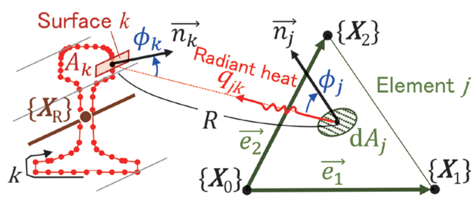

Fig. 5 Radiant heat received by the rail from the geographical feature (triangle element j)

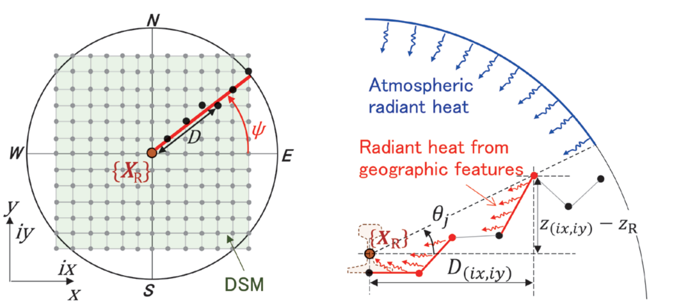

(a) Node extraction in the ψ direction (b) Determination of radiant heat shielding (ψ direction)

Fig. 4 Modeling of radiant heat with shielding of ground objects

$$\cos\phi_k = \frac{\overrightarrow{n_k} \cdot \vec{p}}{|\overrightarrow{n_k}||\vec{p}|} \tag{10}$$

Substituting (7) - (10) into (6), the radiant heat q_{jk} received by the rail from element j can be calculated. Applying this to all the elements identified in the previous section and to the rail surface and summing them up, the radiant heat Q_G ($=\sum_k \sum_j q_{jk}$) received by the rail at position $\{\boldsymbol{X}_R\}(=l)$ from the surrounding geographical features can be calculated.

2.5 Atmospheric radiant heat received by rails

Downward infrared radiation, R_D, is used to calculate the radiant heat of the atmosphere. Downward infrared radiation is the heat radiated to the earth's surface from all directions in the sky by clouds, water vapor, carbon dioxide, etc. in the atmosphere. This is constantly observed by the Japan Meteorological Agency to monitor global warming. In the developed model, the downward infrared radiation, R_D, is corrected using (11), assuming that the radiative heat from the atmosphere is uniform in all directions in the sky and taking into account the shielding of the radiative heat by the geographical features shown in Fig. 4. Furthermore, the radiant heat of the atmosphere received by surface k is calculated from (12), which is the product of the area of surface k, the corrected downward infrared radiation, and the view factor for looking up at the sky from surface k on the rail.

$$\acute{R}_D = \frac{R_D}{2\pi}\int_0^{2\pi}\int_0^{\frac{\pi}{2}} sky_{(\psi,\theta)}\cos\theta \mathrm{d}\theta \mathrm{d}\psi \tag{11}$$

$$p_k = A_k \acute{R}_D \frac{1+\cos\beta_k}{2} \tag{12}$$

where $sky_{(\psi,\theta)}$ is a parameter indicating whether or not the radiative heat of the atmosphere is shielded by the geographical features. As shown in Fig. 4(b), $sky_{(\psi,\theta)}$ is set to 1 in regions of the sky area where θ>max$\{\theta_j\}$ as the atmospheric radiant heat reaches the rail, and 0 otherwise. β_k is the inclination angle of surface k from the horizontal plane (Fig. 6). At $\{\boldsymbol{X}_R\}(=l)$, the radiant heat Q_W ($=\sum_k p_k$) that the rail receives from the atmosphere can be calculated by finding the radiative heat p_k over the entire circumference of the rail and summing them. The absorbed heat Q_{IN} of the rail is given by (13) using Q_W, Q_G and the rail surface emissivity ε_R.

$$Q_{IN}(l,t) = \varepsilon_R(Q_G + Q_W) \tag{13}$$

2.6 Heat discharged by the rail and heat conduction analysis

The heat discharged from the rail Q_{OUT} is the sum of heat conduction to the track pad (a cushioning rubber pad placed between the bottom of the rail and the top of the sleeper) J_C, convective heat transfer to the air J_T, and radiation heat from the rail surface J_R. J_C is a function of rail temperature and air temperature, J_T is a function of rail temperature, air temperature, and wind speed, J_R is a function of rail temperature [3]. Rail temperatures at night are often lower than the air and track pad temperatures. In such cases, heat is absorbed from the air and track pad, but is treated as negative emission heat in the calculations.

In the heat conduction analysis, the heat balance of the rail, (Q_{IN} - Q_{OUT}), is substituted into the heat conduction equation, and the temperature change during Δt is calculated successively by an explicit method. For details, see Ref. [3].

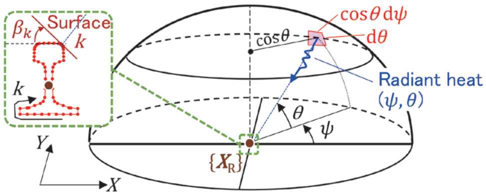

Fig. 6 Radiant heat of the atmosphere received by the rail from the (ψ, θ) direction

3. Verification test of the accuracy of rail temperature analysis at night

As shown in Fig. 7(a), rail temperature and radiant heat received by the rail were measured and compared at locations in close proximity to the building. In addition, meteorological elements were measured and input into a nighttime rail temperature prediction model to obtain rail temperatures analytically. The analysis results were compared with the measured rail temperatures to verify the accuracy of the analysis.

3.1 Measuring conditions

Figure 8 shows the geographic features and measurement points on the test site. The test site is a ballasted track with a continuous welded rail, straight track alignment, JIS 60 kg rails, and PC sleepers. The major surrounding geographical features are Building 1, Building 2, and Building 3 (Fig. 7(a) and Fig. 8). The test period was from December 7, 2022 to January 7, 2023. There was no snowfall during this period, and rainfall occurred on December 13, 18, and 22. The following items were measured.

3.1.1 Rail temperature

In order to determine the distribution of rail temperatures, thermocouples (T-FFF(M), Fukuden) were attached on the side of the rail on the FC (field corner) side at the 11 measuring points (T1-T11) shown in Fig. 8, and rail temperatures were measured at 10-minute intervals.

3.1.2 Meteorological elements (air temperature, wind speed)

As shown in Fig. 8, a weather station (Fig. 7(b) right, Vantage Pro2, Davis) was installed at a height of 1 m above the ground near T1 to measure air temperature (A1) and wind speed (W1). A thermo-hygrometer (Fig. 7(b), middle left, LR5001, HIOKI) was installed at a height of 20 cm above the ground near T9 to measure air temperature (A9). The measurement interval was 10 minutes.

3.1.3 Radiant heat from surroundings

To measure the difference in radiant heat from the environment at each location, a long-wave radiometer (lower left in Fig. 7(b), CHF-IR02, Climatec) was installed near T2, T6 and T9 as shown in Fig. 8, and the radiant heat (L2, L6, L9) from the atmosphere and surrounding geographical features were measured at 10-minute intervals. The measured values of this instrument are the radiant heat received by the installation surface (in this case, a horizontal surface), and the measurement sensitivity U is proportional to the sine of the elevation angle θ of the ground object viewed from the instrument ($U \propto \sin\theta$). Therefore, the measured radiant heat from geographical features is less than the true value at lower height and

(a) Surrounding buildings

(b) Measurement equipment

Fig. 7 Photographs of the test condition

more distant. Thus, we used the apparatus for measuring the radiant heat distribution in the sky developed in Ref. [7], shown in Fig. 9. This apparatus can measure the radiant heat distribution in the sky spherically (with no decrease in measurement sensitivity due to elevation angle θ) by installing a thermography camera at the top surface of the rail, taking multiple thermal images of the entire sky, converting the obtained thermal images into radiant heat, and integrating them. Using this apparatus, we measured the radiant heat distribution of the sky as seen from the measurement points at T1, T2, and T4 to T10, a total of 9 measurement points, between 3:00 and 4:00 on December 15.

3.2 Analysis conditions

Figure 10 shows the results of rail temperature measurements. The days analyzed were the nighttime hours (0:00-7:00) of December 24, the day with the lowest rail temperature during the test period (−6°C at T11), and the nighttime hours of December 25, the following day.

3.2.1 Geographical data

The geographic data used for the analysis were the DSM and rail node data shown in Fig. 8, where the DSM is NTT Data's AW3D (0.5 m pitch) and the rail nodes are points placed at approximately 1 m intervals along the L_ROAD rail line data of the ArcGIS Geo Suite.

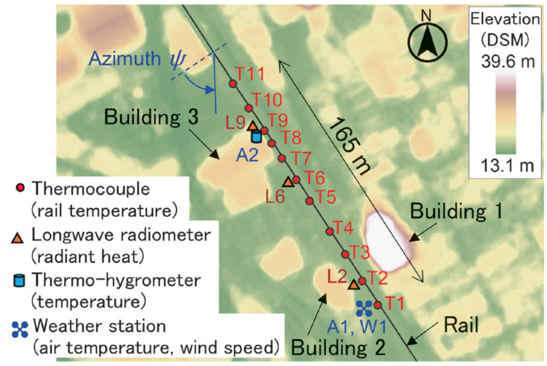

Fig. 8 Arrangement of measuring points and surrounding geographical features

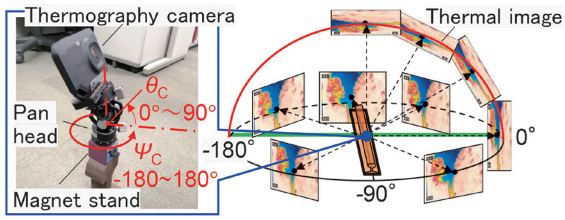

Fig. 9 Measuring device for radiant heat (spherical) distribution

3.2.2 Meteorological data

Measurements of air temperature (A1) and wind speed (W1) at the weather station shown in the upper part of Fig. 11 were applied to the air temperature and wind speed data used to predict the rail temperature prediction. The bottom part of Fig. 11 shows the sum of the radiant heat from the geographical features and the atmosphere, with L6 having the smallest radiant heat. This is because L6 is the furthest away from the surrounding buildings among the three locations where the longwave radiometer was installed. Thus, we considered that the measurement at L6 contains the largest radiant heat component of the atmosphere, and used it as the radiant heat of the atmosphere in the analysis.

3.2.3 Analysis parameters

The main parameters used in the rail temperature analysis are listed in Table 1. The rail surface emissivity ε_R was set to 0.20 for the top (30 mm wide) assuming a polished surface, and 0.75 for the others assuming an oxidized surface. The emissivity ε_j of geographical features was set to 0.95 for elements with elevations lower than the rail elevation +0.1 m, assuming the ground surface, and 0.57 (0.6 times the ground surface) for other elements, assuming trees or other features with gaps or man-made features. The measured air temperature ("A1" on Fig. 11) was applied to the temperature of the geographical features. The time increment Δt was 10 min (600 s) and the spatial increment Δl in the longitudinal direction of the rail was 1 m, the same as the point data interval of the track.

3.3 Test results

3.3.1 Comparison of the measurements of rail temperature and radiant heat

Figure 12 shows the radiant heat distribution in the sky mea-

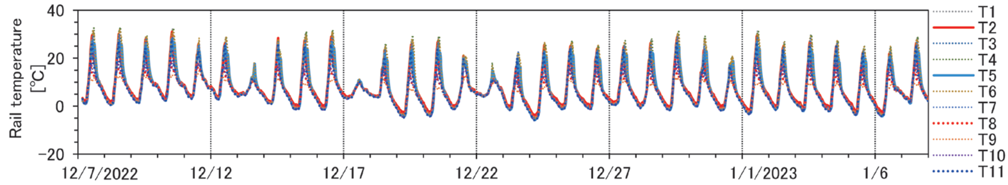

Fig. 10 Measurements of rail temperature

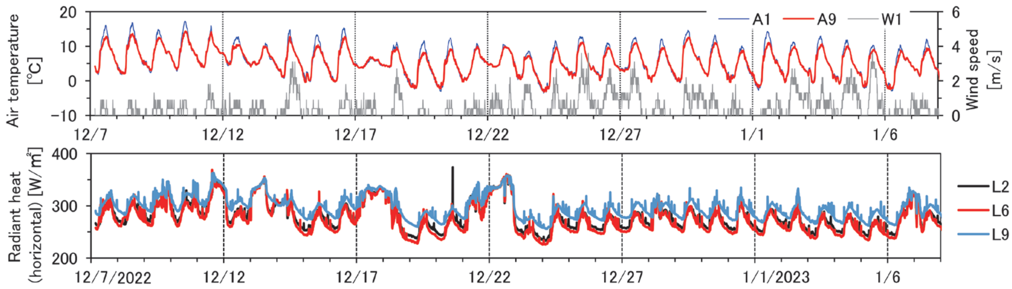

Fig. 11 Measurements of meteorological elements

Table 1 Analysis parameters

Item		Value
Emissivity on the rail surface	ε_R	Top Surface : 0.20 Other surface : 0.75
Emissivity on the geographical features	ε_j	$z < (z_R + 0.1\text{m})$: 0.95 $z \geq (z_R + 0.1\text{m})$: 0.57
Downward infrared radiation	R_D	Figure 11 bottom “L6”
Stefan–Boltzmann constant	σ	5.67×10^{-8} W/(m^{2}K^4)
Temperature of the geographical features	T_j	Same as air temperature
Thermal conductivity of the rail pad	λ_p	0.25 W/(mK)
Thickness of the rail pad	L_p	0.007 m
Density of the rail steel	ρ_R	7820 kg/m^3
Specific heat of the rail	c_R	461 J/(kgK)
Thermal conductivity of the rail	λ_R	50 W/(mK)
Cross-sectional area of the rail	A_R	0.00775 m^2

z: Elevation of the geographical feature, z_R: Elevation of the rail

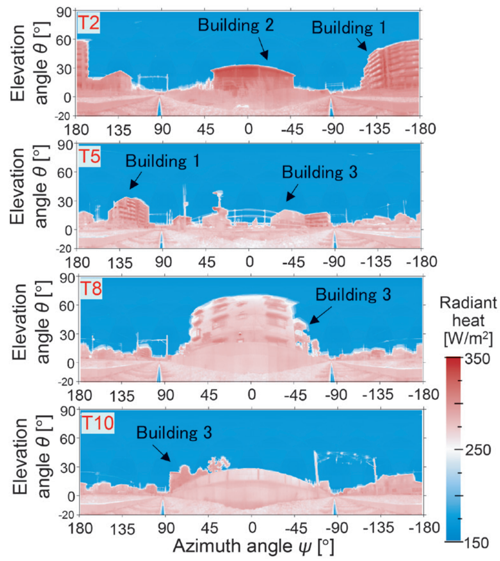

Fig. 12 Measurements of radiant heat distribution

sured by the thermography camera. The azimuth angle ψ=0° is in the direction orthogonal to the railway track on the southwest side (lower left direction in Fig. 8), ±90° is the measurement rail, 0° to 180° is the T1 side, and −180° to 0° is the T11 side. In Fig. 12, areas with buildings, trees, poles, and other geographical features are colored white to red because of their high radiant heat, while areas without landmarks that receive radiant heat from the atmosphere are colored blue. This figure shows that uneven surfaces such as windows and balconies of buildings have more radiant heat than flat surfaces. In addition, the total radiant heat from the walls of Building 2 is greater than that of Building 3. Comparing Building 1 near T2 with Building 3 near T8, Building 1, whose southwest wall faces the railway track (Fig. 7(a)), has more unevenness and more radiant heat (darker red in Fig. 12) than Building 3, whose northeast wall faces the railway track because its balcony extends toward the railway track. In addition, the radiant heat from the walls of Building 2 is generally greater than that of Building 3 (Fig. 12). The reason for this is not clear, but it is thought to be related to differences in the emissivity of the exterior walls, thermal insulation, and wall temperatures due to the different uses of the buildings, as Building 2 is an electric substation and Building 3 is an apartment building.

The radiant heat received by the rail was calculated by integrating the measurement results in Fig. 12 over the entire sky area, and its comparison with the rail temperature is shown in Fig. 13. Figure 12 and Fig. 13 show that T2 and T8, which are close to the buildings, receive more radiant heat than the other measurement points, and their rail temperatures are about 2°C higher than those of T5 and T11, which are farther away from the buildings. This result confirms a clear correlation between the surrounding geographical features, the radiant heat and the rail temperature at night.

3.3.2 Comparison of measured and analyzed rail temperatures

Figure 14 shows a comparison of the measured and analyzed rail temperatures on December 24. Figure 14(a) also shows the measured air temperature and the results of the analysis using the daytime rail temperature prediction model. A comparison of rail temperatures and air temperatures shows a difference: rail temperatures continued to drop until around 5:00 pm and dropped to −6°C at T11, while air temperatures stopped dropping around 3:00 pm with a

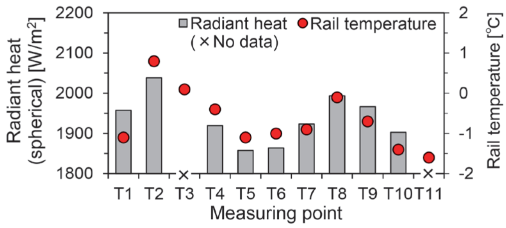

Fig. 13 Comparison of measured rail temperatures (December 15, 3:30) and radiant heat calculated from Fig. 12

minimum value of −3.5°C (Fig. 14(a)). The results of the daytime rail temperature prediction model, which does not take into account radiant heat from geological features, show a significant deviation from the measured values, with the rail temperature falling below −10°C at 3:00 pm. On the other hand, the results of the nighttime rail temperature prediction model are close to the measured values. Here, the analytical value of the lowest rail temperature at T8 is 0.2°C higher than the measured value, while at T2 it is 0.3°C lower than the measured value. This may be due to the fact that the difference in radiant heat due to the shape and use of the building, as described in the previous section, was not taken into account, but the effect on the analytical results is small, less than 0.5°C. Figure 14(b) shows that the rail temperature at 5:00 was 1.7°C higher at T2, which is closer to the building, than at T5, which is farther from the building. Similar results are obtained in the analysis, indicating that the measured and analyzed values are in good agreement. Thus, the detailed modeling of radiant heat from geological features using DSM data significantly improves the accuracy of the analysis of rail temperature at night compared to previous studies [3].

Figure 15 shows a comparison of analytical and measured rail temperatures on December 25. From the right hand side of Fig. 15(b), the difference in rail temperature between T2 near the building and T5 far from the building at 5:00 was around 1.5°C for both the measurement and the analysis, and the rail temperature difference between the measurement points generally agreed between the measurement and the analysis. However, although the analytical values of the nighttime rail temperature prediction model were closer to the measured values than the daytime rail temperature prediction model, the analytical values of rail temperature were 1°C to 1.5°C higher than the measured values at all measurement points.

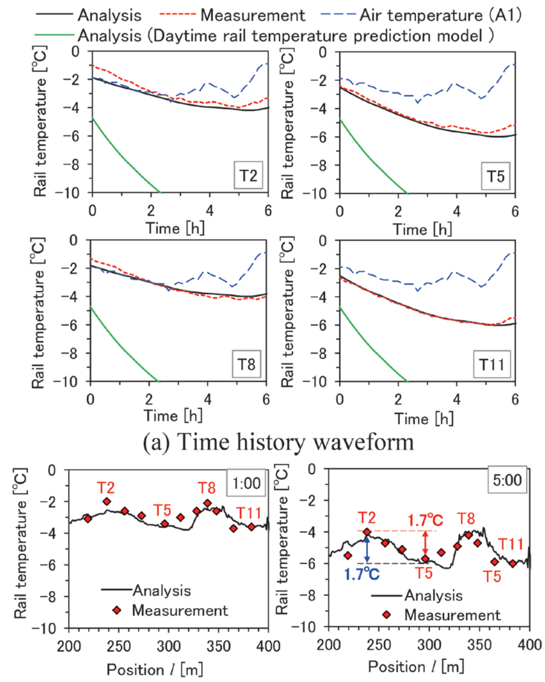

(a) Time history waveform

(b) Distribution in rail longitudinal direction

Fig. 14 Comparison of measured and analyzed rail temperatures (December 24)

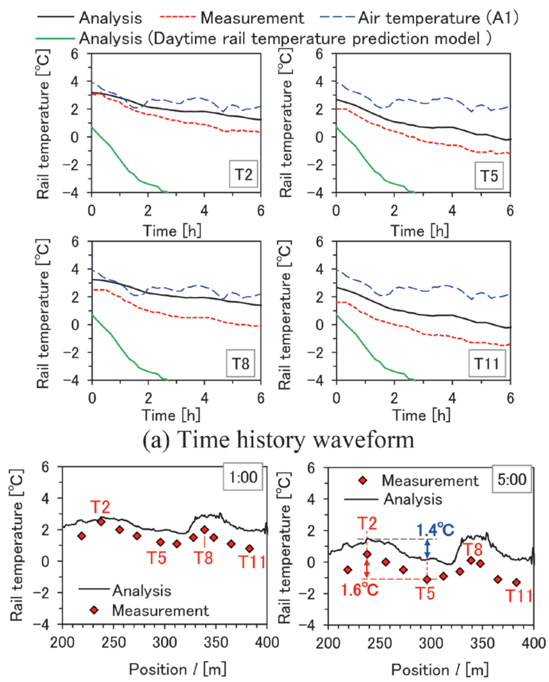

(a) Time history waveform

(b) Distribution in rail longitudinal direction

Fig. 15 Comparison of measured and analyzed rail temperatures (December 25)

4. Discussion

In order to accurately predict the annual minimum rail temperature and its longitudinal distribution, which is important for rail axial force management, a method for predicting the nighttime rail temperature was proposed based on modeling the radiant heat from surrounding geographical features using DSM data. Measurements taken at night during winter on the actual track showed a clear correlation between rail temperature, radiant heat, and the location of buildings, with the radiant heat received by the rails being greater at points closer to buildings being larger and the minimum rail temperature being approximately 2°C higher than at points farther away. Although nighttime temperatures of rails and other track components are conventionally estimated from air temperatures, these results indicate that rail temperatures are difficult to predict accurately from air temperatures alone, and that the proposed method of modeling radiant heat from geological features is effective. The measured meteorological conditions were applied to the proposed method to obtain rail temperatures analytically. The measured and analyzed values agreed well for December 24, when the rail temperature was the lowest during the measurement period. On the following day, however, the rail temperature was 1°C to 1.5°C higher than the measured rail temperature at all measurement points in the test area, although the difference in rail temperature between the measurement points could be reproduced by the analysis. The rail temperature distribution is considered to be a superposition of a wide range of average rail temperatures due to meteorological conditions and local variations due to geographical conditions. For the latter, it was found that the proposed method can accurately reproduce the temperature distribution, since the temperature difference between the measurement points is in agreement between the measurement and the analysis. On the other hand, for the former case, similar analysis errors occurred in the entire test area, suggesting that there were problems with the acquisition of meteorological conditions and the modeling method. We will continue to verify this issue in the future.

It was found that the proposed method can accurately calculate local variations in the lowest rail temperature distribution due to geographical conditions. In this paper, the maximum difference in minimum rail temperature between locations was approximately 2°C. However, the difference in rail temperature is expected to be more pronounced between locations where there are few surrounding geographical features, such as along rivers and on long viaducts, and locations where there are slopes and trees in close proximity, such as in mountainous areas. By quantitatively predicting these differences in minimum rail temperatures using the proposed method and reflecting them in the fastening-down temperature, it is expected that the safety of the track against buckling in summer will be improved and the number of measures required due to increased rail axial forces, such as restressing of continuous welded rails and special track patrols, will be reduced. However, some analytical errors were observed in this test, which may have been caused by the setting of the meteorological conditions and the modeling method. We will continue to study the effects of differences in meteorological conditions due to region and elevation on the minimum rail temperature. In the proposed method, the detailed geometry of the building was modeled simply using DSM and its characteristics (emissivity and wall temperature) were assumed to be the same for all buildings, but differences in radiant heat were measured for the actual buildings, which might be due to their shape and use. The influence of the rail temperature on the analysis results were small, less than 0.5°C. However, in order for the proposed method to be widely used, it is necessary to verify the degree of influence caused by various structures, topography, vegetation, and other factors.

5. Conclusions

In order to predict in detail, the annual minimum rail temperature and its distribution, which is important for rail axis force management, a method for predicting the nighttime rail temperature was proposed based on modeling the radiant heat from surrounding geological features using DSM data. In order to verify the validity and accuracy of the proposed method, the rail temperature and the radiant heat received by the rail were measured on a real track and compared with the analytical values. The findings are as follows.

・While there was a clear correlation between rail temperature, radiant heat, and building configuration, rail temperature and air temperature exhibited different behaviors. These results confirm the difficulty of accurately predicting rail temperature from air temperature alone and the effectiveness of the proposed method of modeling radiant heat from geographical features.
・The local variations in the minimum rail temperature distribution due to geographical conditions were observed, such as the minimum rail temperature being approximately 2°C higher at the measurement points near buildings than at other points. We found that the proposed method can accurately reproduce these temperatures.
・Since analysis errors were observed that may be attributable to radiant heat from the atmosphere, the shape and use of the building, and other factors, the effects of modeling methods for meteorological conditions, as well as the effects of various structures, topography, vegetation, and other factors on the minimum rail temperature, should be further examined.

References

[1] Tamagawa, S., Nishinomiya, and Y., Koketsu, T., “New Restrictions of Maintenance Works for Continuous Welded Rails at Low Temperatures,” *RTRI Report*, Vol. 36, No. 3, pp. 11-16, 2022 (in Japanese).
[2] Lichtberger B., *Track Compendium*. Eurailpress, pp. 63-66, 2011.
[3] Urakawa, F., Watanabe, T., and Kimura, S., “Wide-area Rail Temperature Prediction Method Using GIS Data,” *Quarterly Report of RTRI*, Vol. 62 No. 1, pp. 61-66, Feb. 2021.
[4] Zhang, Y., Clemenzi, J., Kesler, K. and Lee, S., “Real time prediction of rail temperature,” *Proceedings of the AREMA 2007 Annual Conference*, Chicago, IL, 2007.
[5] Bruzek, R., Al-Nazer, L., Biess, L. and Kreisel, L., “Rail temperature prediction model as a tool to issue advance heat slow orders,” *Proceedings of the AREMA 2014 Annual Conference*, Chicago, IL, 2014.
[6] Wang, H., Chen, J., Balaguru, P.N. and Al-Nazer, L., “Thermal benefits of low solar absorption coating for preventing rail buckling,” *Proceedings of the 2015 Joint Rail Conference*, San Jose, CA, USA., 2015.
[7] Urakawa, F., Watanabe, T., and Tsujie, M., “Measurement of Infrared Radiation Distribution from Geographical Features along Railway Tracks and its Relation to Nighttime Rail Temperatures,” *J-RAIL2022*, S2-7-2, 2022.
[8] Saida, A, Fujimoto, A. and Fukihara, T., “Forecasting Model of Road Surface Temperature Along a Road Network by Heat Balance Method,” *Journal of JSCE*, Ser. E1, Pavement Engineering, Vol. 69, No. 1, pp. 1-11, 2013 (in Japanese).

Authors

Fumihiro URAKAWA
Senior Researcher, Track Dynamics Laboratory, Railway Dynamics Division
Research Areas: Rail Temperature and Axial Force, Track Buckling, Track Vibration

Tsutomu WATANABE, Dr.Eng.
Senior Chief Researcher, Head of Track Dynamics Laboratory, Railway Dynamics Division
Research Areas: Dynamic Interaction of Vehicle, Track and Bridge, Vibration Analysis, Concrete Sleeper

Design Method for Seismic Control Devices Installed on Steel Railway Bridges

Kazunori WADA
Structural Dynamics and Response Control Laboratory, Center for Railway Earthquake Engineering Research

Takuma KUSHIYA
Steel & Hybrid Structures Laboratory, Structure Technology Division

Akihiro TOYOOKA
Center for Railway Earthquake Engineering Research

Authors have proposed a seismic control device with a bridge collapse prevention function installable in narrow spaces. In this paper, we introduce a method for designing the proposed device. Specifically, we organized the results of the nonlinear response analysis of a single degree of freedom system and proposed a nomogram that can be used to calculate the displacement of the girders and the response ductility factor of the piers in accordance with equipment specifications. By using this method, it is possible to have a rough idea of the specifications to meet the required performance before detailed dynamic analysis is carried out.

Key words: *seismic control device, design method, steel railway bridges*

1. Introduction

In the seismic retrofit of bridges, when applying common methods such as steel plate lining becomes challenging, the use of seismic control devices emerges as a viable alternative. Notably, for railway bridges, instances include the application of friction-type dampers to long bridges where conventional methods for reinforcement are difficult to use [1], and the use of brace-type dampers for viaducts where column reinforcement is hindered due to commercial space constraints [2]. However, in urban areas where bridges cross roads or railways, there are cases where the clearance beneath the girders is insufficient, making installation of traditional dampers unsuitable. Therefore, our research group has developed a compact and seismic control device using a group of steel rods with bridge collapse prevention function (hereafter referred to as the "proposed device") for steel railway bridges without a ballast floor [3].

The application of seismic control devices is expected to increase in the future. Currently, for the design of these devices, detailed analytical models such as frame models are typically constructed. Iterative nonlinear dynamic analyses are then performed based on device parameters (referred to as "detailed analysis"). However, this repetitive computational process can be cumbersome and hinders efficient application. If initial values for the device parameters that satisfy performance requirements and excessive specifications can be set efficiently, the number of iterations in the detailed analysis could be reduced, streamlining the design process.

To achieve this, we developed an efficient method for setting initial values of rod specifications during detailed analysis (referred to as "simplified rod specification setting method") for applying the proposed device to steel railway bridges. The design flow of the proposed device using this method is shown in Fig. 1. Before starting the detailed analysis (step 3) which tends to make the work complicated, the approximate rod specifications to meet the required performance can be set in step 2. This is expected to reduce the number of iterative calculations during detailed analysis. In this paper, we focus on specific aspects of the proposed device's design method (Fig. 1), including an overview of the device, trend analysis through parameter studies, and the calculation nomogram for response displacement and response ductility ratio based on literature [4]. Additionally, since some members of our team have conducted similar investigations for friction-type dampers which are widely adopted [5], combining our findings with theirs could enable efficient design of numerous seismic control devices.

2. Study overview

This section outlines the proposed device (Section 2.1) and approach to modeling rod specifications (Section 2.2).

2.1 Overview of the proposed device [3]

As shown in Fig. 2, the proposed device has a structure in which multiple steel rods are installed on the top of the abutment using post-installed anchors, and then attached to the girder via a composite frame. This structure uniformly transfers the inertial force of the grinder to the group of steel rods. The device provides seismic control through energy absorption from the post-yield bending deformation of the rods (Fig. 2A) and prevents bridge collapse by supporting the girder weight with the high ductility of the rods

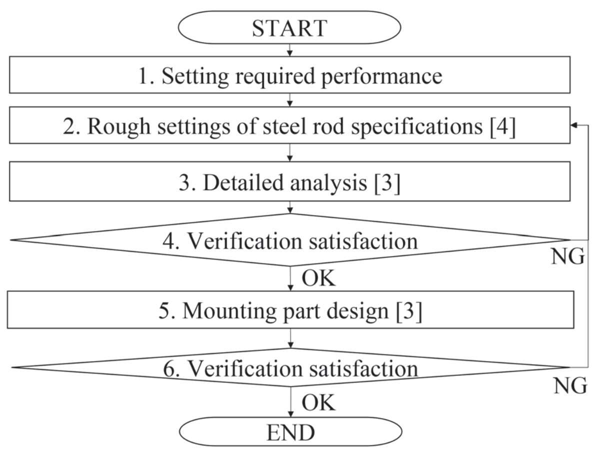

Fig. 1 Design flow of the proposed device

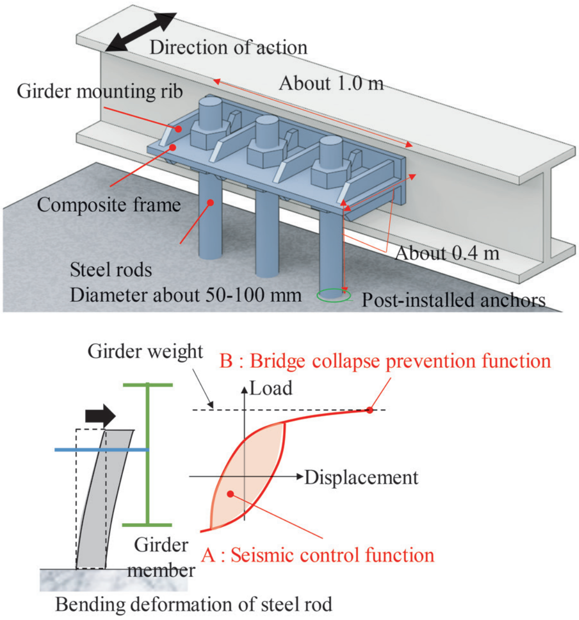

Fig. 2 Overview of the proposed device

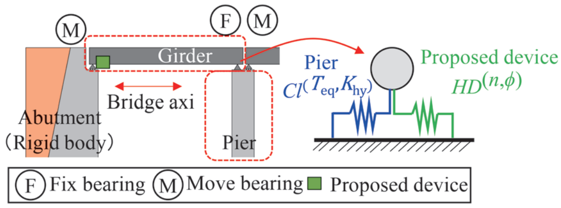

Fig. 3 Target bridges and modeling methods

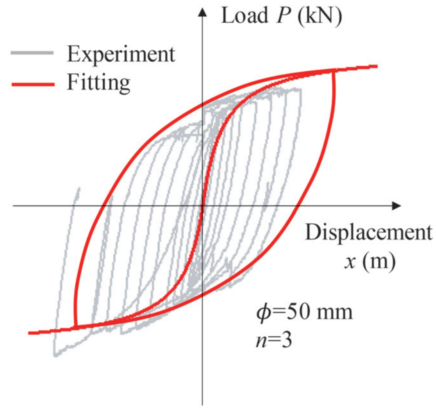

Fig. 4 Nonlinear characteristics of the device (steel rod diameter 50 mm, number of steel rods 3)

(Fig. 2B). Furthermore, since the device is designed for narrower girder bearing areas, the rod diameters are ranging from approximately 50 mm to 100 mm, the number of rods is 3 to 8 rods per location, and overall dimensions are approximately 80 mm. As a specific example, in the case of three rods, the size is 1 m in width; 1 m in height; 0.4 m in depth; and 0.4 m in depth. Therefore, the device does not foul the clearance beneath the girder. The seismic control function of the proposed device can be adjusted arbitrarily by modifying rod diameter, rod number, rod material, and load height.

2.2 Target bridges and modeling approach

Figure 3 illustrates the concept of the target bridges and modeling methods. We focused on bridges where one side serves as an abutment and the other as a pier. Such structures exist in various contexts, including bridges across roads, bridges across railroads, and bridges across rivers. Considering the primary purpose of the proposed device as a countermeasure against the risk of bridge collapse, we focused our study on the bridge axis. Our modeling approach follows the concept of design vibration units used in seismic design for railways, employing a single-degree-of-freedom model. Specifically, we modeled the girder-fixed support-pier system enclosed by the red box in Fig. 3 as one design vibration unit. The pier was modeled using a Bi-Linear skeleton curve and Clough model for hysteresis behavior (yield stiffness degradation ratio α = 0.1, stiffness degradation index β = 0.2) based on literature [6]. The damping characteristics were treated as period dependent. We assumed the abutment to be sufficiently sound and treated it as a rigid body with the same behavior as the ground. The nonlinear characteristics of the proposed device were modeled using a hyperbolic curve following the Masing rule, which was fitted to previous experimental results shown in Fig. 4. Additionally, considering variations in the number and diameter of steel rods (as discussed in Section 2.3), adjustments were made to the results from Fig. 4, allowing the proposed device to model any desired combination of rod number and diameter.

2.3 Parameter Organization

The parameters to be examined are the vibration characteristics of bridge piers (equivalent natural period T_{eq}, yield seismic coefficient K_{hy}) and the specifications of the proposed device (steel rod diameter φ, rod number n). Additionally, the equivalent mass m is considered when replacing the mass of the girder and bridge piers with a single-degree-of-freedom system. By examining the relationships between these parameters based on the motion equation for a single-degree-of-freedom system, we can organize the parameters for subsequent analysis.

The motion equation for the target model is expressed as follows:

$$\ddot{x}+2h\omega\dot{x}+\frac{Cl^{(T_{eq},K_{hy})}(x)}{m}+\frac{HD^{(n,\phi)}(x)}{m}=-\ddot{z} \qquad (1)$$

Here, x represents displacement, h is the damping coefficient, ω is the natural circular frequency, and z denotes the ground surface displacement due to input seismic motion. The terms $HD^{(n,\phi)}(x)$ is the restoring force of the hyperbolic model when the steel rod diameter is ϕ and the number of rods is n, and $Cl(T_{eq}, K_{hy})(x)$ is the restoring forces of the bridge piers at the equivalent natural period T_{eq} and yield seismic coefficient K_{hy}.

The left-hand side terms (third and fourth terms) representing the restoring forces are expected to vary with mass. Specifically, the third term corresponds to the restoring force of the bridge piers, modeled as a Bi-Linear curve for skeletal behavior and a Clough model for hysteresis behavior (as discussed in Section 2.2). Notably, these terms, which are defined by the equivalent natural period T_{eq} and yield seismic coefficient K_{hy}, as well as yield stiffness degradation ratio α and stiffness degradation index β, are known to be independent of equivalent mass (Fig. 5).

Yield point : $p_y=K_{hy}\,g$ (g : gravitational acceleration) (2a)

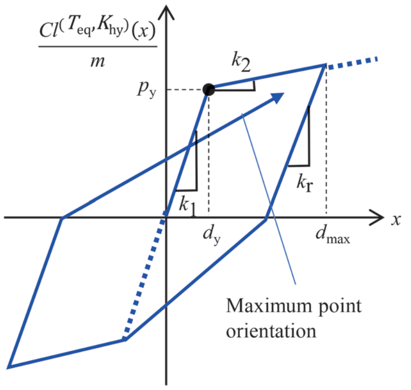

Fig. 5 Overview of pier restoring force model

$$\text{Initial stiffness divided by mass}: k_1=\left(\frac{2\pi}{T_{eq}}\right)^2 \tag{2b}$$

$$\text{Secondary stiffness}: k_2=\alpha k_1(\alpha\ :\text{constant}) \tag{2c}$$

$$\text{Stiffness during unloading}: k_r=k_1\left(\frac{d_{max}}{d_y}\right)^{-\beta}\quad(\beta: \text{constant}) \tag{2d}$$

Next, let's consider the fourth term $HD^{(n,\phi)}(x)/m$ in (1). This nonlinear behavior is modeled using a hyperbolic curve following the Masing rule, fitted to previous experimental results (as shown in Fig. 4). The skeletal curve is expressed as:

$$P_{HD}^{(n,\phi)}(x)=\frac{K_0(\phi)nx}{1+x/\delta_y(\phi)} \tag{3}$$

Here, $K_0(\phi)$ represents a stiffness-related parameter; $\delta_y(\phi)$, a parameter related to yield displacement. Each of both is an index per steel rod bar with diameter ϕ. For instance, for a steel rod diameter of 50 mm, the fitting results yield $K_0(50)=2.6\times10^3$ kN/m^2 and $\delta_y(50)=1.1\times10^{-2}$m . When considering different rod numbers n', the skeletal curve can be expressed as:

$$P_{HD}^{(n',\phi)}(x)=\frac{n'}{n}P_{HD}^{(n,\phi)}(x) \tag{4}$$

Furthermore, since the Masing rule is independent of the skeletal curve, the following relationship holds:

$$HD^{(n',\phi)}(x)=\frac{n'}{n}HD^{(n,\phi)}(x) \tag{5}$$

Now, when the equivalent mass is m' and the number of steel rods is n', (1) can be written as the following equation.

$$\ddot{x}+2h\omega\dot{x}+\frac{Cl^{(T_{eq},K_{hy})}(x)}{m'}+\frac{HD^{(n',\phi)}(x)}{m'}=-\ddot{z} \tag{6}$$

Substituting (5) into (6) yields the following.

$$\ddot{x}+2h\omega\dot{x}+\frac{Cl^{(T_{eq},K_{hy})}(x)}{m'}+\frac{n'HD^{(n,\phi)}(x)}{m'n}=-\ddot{z} \tag{7}$$

Here, comparing (7) with (1), the only difference between (7) and (1) is the fourth term on the left side, since the third term on the left side does not depend on the equivalent mass as mentioned earlier. When these coefficients are equal, that is, when the following equation holds, the behavior of the mass points is consistent.

$$\frac{1}{m}=\frac{1}{m'}\cdot\frac{n'}{n}\ \Leftrightarrow\ \frac{m'}{m}=\frac{n'}{n} \tag{8}$$

From (8), we observe that if the ratio of equivalent mass m' to actual mass $m\left(\frac{m'}{m}\right)$ and the ratio of rod number n' to actual rod number $n\left(\frac{n'}{n}\right)$ are equal, the behavior of the girder will match. Therefore, by pre-assessing a reference mass m, we can adjust the number of rods for actual bridges to account for differences in mass.

Additionally, when changing rod diameter, we compensate $P_{HD}^{(n,\phi')}(x)$ using the stiffness ratio K_r and yield displacement ratio δ_{yr}, as shown in Fig. 6 and the following equation.

$$P_{HD}^{(n,\phi')}(x)=\frac{K_0(\phi')nx}{1+x/\delta_y(\phi')}=\frac{K_rK_0(50)nx}{1+x/(\delta_{yr}\delta_y(50))} \tag{9}$$

Here, the stiffness ratio K_r is expressed as the ratio of the yield load ratio P_{yr} to the yield displacement ratio δ_{yr}, as shown in the following equation.

$$K_r=\frac{P_{yr}}{\delta_{yr}} \tag{10}$$

In addition, the yield load P_y and yield displacement δ_y of the steel rod diameter ϕ are calculated using the following equations as the load and displacement when the edge stress reaches the yield strength σ_y, assuming the steel rod is a cantilever beam.

$$P_y=\frac{I\sigma_y}{0.5\phi}\cdot\frac{1}{h},\quad \delta_y=\frac{P_yh^3}{3EI} \tag{11}$$

In the above equation, I is the second moment of area of the steel rod; h, the height of the loading point; and E, the Young's modulus. By calculating yield load and yield displacement using (11), we can determine the necessary parameters for compensating the skeletal curve in (9).

In summary, the parameters for parametric study are listed in Table 1. The study covers a range from 0.2 s to 5 s of equivalent natural periods (T_{eq}) and a range from 0.2 to 2 of yield seismic coefficients (K_{hy}). The reference mass m is set between 100 t and 2000 t. Two rod diameter cases 50 mm and 80 mm are examined, with the number of rod n ranging from 1 to 12. The input seismic motion is based on the L2 seismic spectrum II (G3 ground) used in seismic design for railway structures. Other design seismic motions are also examined in the literature [4]. The material and load height of the rods are fixed based on experimental conditions from literature [3] (material: SS400, load height: 400 mm from the base)

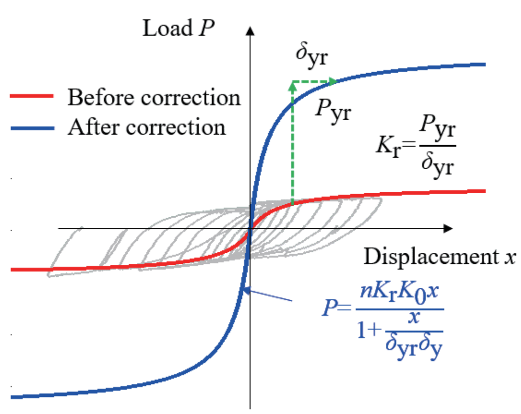

Fig. 6 Nonlinear characteristics of the proposed device (when steel rod diameters are different)

Table 1 List of parameters to consider

Item	Parameter
Pier	Equivalent natural period T_{eq}(s)
	Yield seismic coefficient K_{hy}
	Reference mass m(t)
Proposed device	Rod diameter ϕ (mm)
	Number of steel rods n (relative to reference mass m)

3. Trend analysis through parametric study

3.1 Response displacement waveforms and device hysteresis curves

In this chapter, we perform trend analysis of response results by analyzing several analytical outcomes before calculating the nomogram. As an example, we consider the response displacement waveforms of the girder and the hysteresis curve of the proposed device (Fig. 7) for the following parameters: equivalent natural period T_{eq} of 1.0 seconds, yield seismic coefficient K_{hy} of 0.5, reference mass m of 100 tons, steel rod diameter ϕ of 50 mm, and a total of 8 steel rods. From this figure, it is confirmed that the proposed device exhibits energy-absorbing seismic control effects by tracing loops, resulting in reduced maximum response displacement compared with the case without the proposed device. Subsequently, we analyze the results in terms of maximum response displacement and response ductility factor for each parameter.

3.2 Relationship between steel rod specifications and response values

Under the condition where parameters other than the number of steel rods or steel rod diameter are fixed, we examine the relationship between steel rod specifications and the girder's response displacement as well as the response ductility factor of the bridge piers and foundations. As an example, we consider the following parameters: equivalent natural period T_{eq} of 1.0 seconds, yield seismic coefficient K_{hy} of 0.5, reference mass m of 100 tons, and a total of 8 steel rods, as shown in Fig. 8. Figure 8 shows that the more the number of steel rods n or the steel rod diameter ϕ becomes, the larger the reduction in response displacement and response ductility factor of the girder, bridge piers and foundations becomes. This indicates that the proposed device has a substantial seismic control effect. However, for a steel rod diameter of 80 mm, the reduction in response ductility factor becomes less pronounced when the number of steel rods exceeds 5. This behavior can be attributed to the device's hysteresis curve (Fig. 9) at the specified conditions. When the number of steel rods is small, the device effectively absorbs energy while still supporting the load. However, with a larger number of steel rods, the device behaves almost elastically, diminishing the expected damping effect observed at smaller number of steel rods.

3.3 Relationship between reference mass and response values

Keeping parameters other than the reference mass fixed, we explore the relationship between the reference mass and the girder's response displacement as well as the response ductility factor of the bridge piers and foundations. For instance, considering an equivalent natural period T_{eq} of 1.0 seconds, yield seismic coefficient K_{hy} of 0.5, steel rod diameter ϕ of 80 mm, and a total of 8 steel rods, Fig. 10 reveals that the greater the reference mass m is, the smaller the reduction in response displacement and response ductility factor due to device installation becomes. In other words, the restoring force of the bridge piers becomes larger than that of the proposed device, so that the seismic control effect of the proposed device becomes relatively smaller, as shown in Fig. 11. The proposed device is designed for small-scale applications in urban steel railway bridges without a

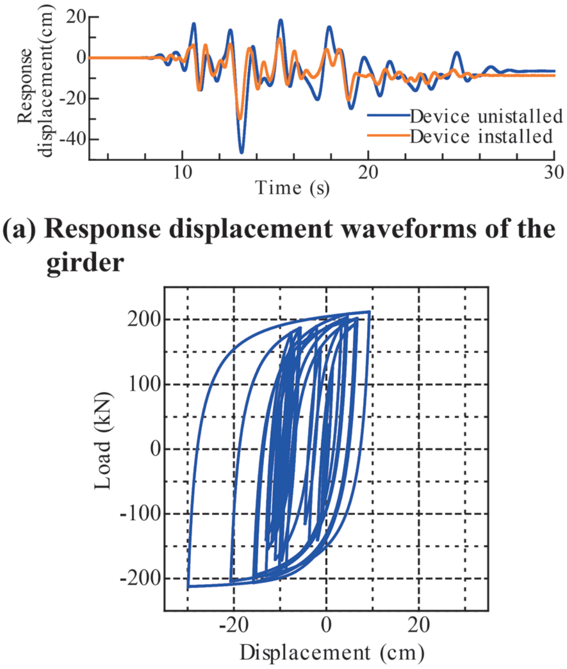

(a) Response displacement waveforms of the girder

(b) Hysteresis curve of the proposed device

Fig. 7 Example of response result (T_{eq}=1.0 s, K_{hy}=0.5, m=100 t)

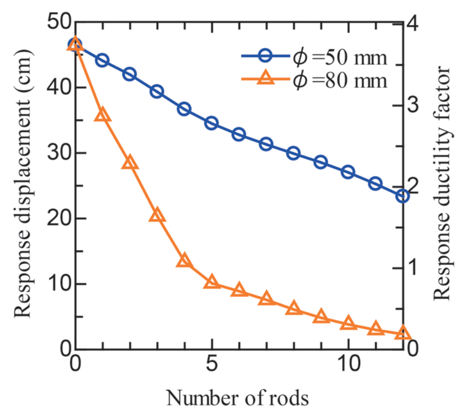

Fig. 8 Example of relationship between steel rod specifications, response displacement, and response ductility factor (T_{eq}=1.0 s, K_{hy}=0.5, m=100 t)

ballast floor. For instance, if we aim to suppress girder response displacement by approximately 50% under the conditions of Fig. 10, a girder mass of around 300 tons would be the upper limit for applicable structures.

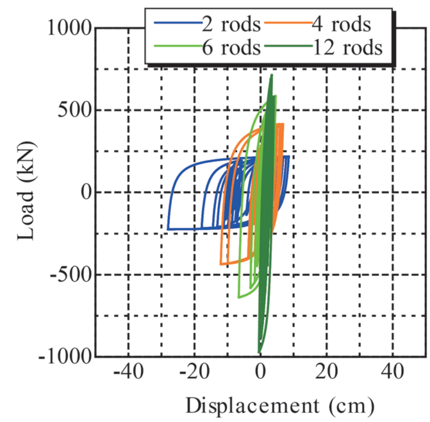

Fig. 9 Example of relationship between steel rod specifications and device's hysteresis curve (T_{eq}=1.0 s, K_{hy}=0.5, m=100 t, ϕ=80 mm)

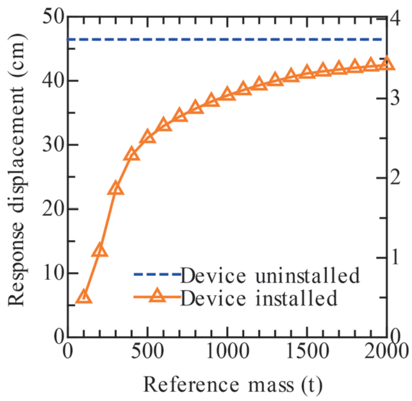

Fig. 10 Example of relationship between reference mass, response displacement, and response ductility factor (T_{eq}=1.0 s, K_{hy}=0.5, n=8)

4. Methodology for roughly setting steel rod specifications using calculation nomograms for response displacement and response ductility factor

In this chapter, we organize calculation nomograms for response displacement and response ductility factor based on seismic response analyses conducted using the parameter range discussed in the previous chapter. First, an overview of the nomogram is presented, and then the procedure for roughly setting steel rod specifications using the nomogram is shown based on a specific example.

4.1 Overview of nomograms

For seismic design of general railway bridges and viaducts, the response ductility factors are calculated by plotting equivalent natural periods and yield seismic coefficients on the well-known Strength Demanded Spectra [6]. These spectra are prepared for each design seismic motion. Therefore, if the designer evaluates the equivalent natural period and yield seismic intensity in advance, it is possible to calculate response values without detailed dynamic analysis. Regarding the rough method for setting steel rod specifications, we will consider an expression method similar to the Strength Demanded Spectra.

Specifically, the authors organized the comprehensive dynamic analysis results for the model shown in Fig. 3 in which the proposed device is installed. As a result, we organized the isolines of the equivalent natural period, response displacement, and response ductility factor for each yield seismic coefficient. An example of a nomogram is depicted in Fig. 12. Such nomogram can be prepared in advance for various design seismic motion, steel rod diameter, steel rod number, and reference mass.

4.2 Procedure for setting steel rod specifications using nomograms

The procedure for roughly setting steel rod specifications using the previously constructed nomograms is outlined in Fig. 13 and described in this section. Note that this process is before transitioning to the detailed analysis shown in Fig. 1.

Step 1: Calculate equivalent natural period and yield seismic coefficient for the target bridge. This requires push-over analysis based on the frame model, which is available from the detailed analysis in Fig. 1.

Step 2: Select the appropriate nomogram based on equivalent

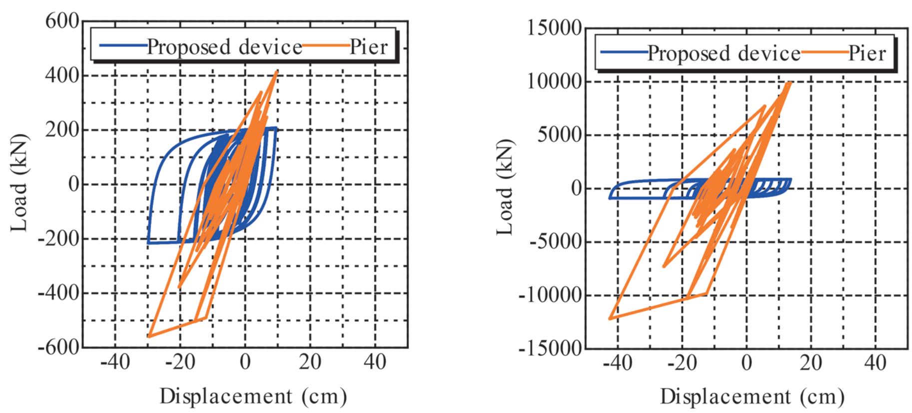

(a) Reference mass m=100 t **(b) Reference mass m=2000 t**

Fig. 11 Hysteresis curve of proposed device and pier (T_{eq}=1.0 s, K_{hy}=0.5, ϕ=80 mm, n=8)

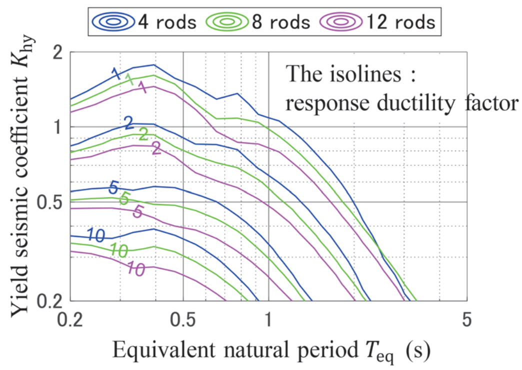

Fig. 12　Example of nomogram (ϕ=50 mm, m=100 t, L2 seismic motion spectrum II (G3 ground))

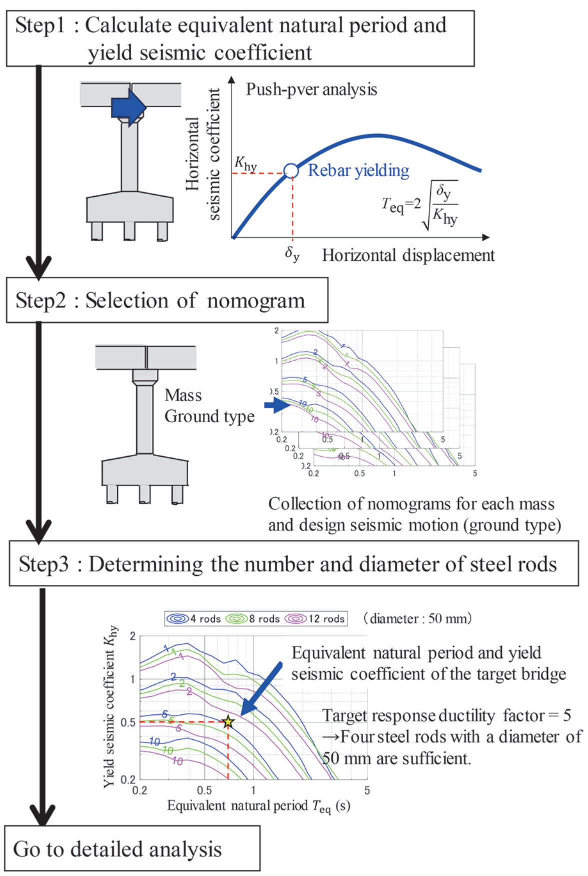

Fig. 13　Procedure for rough setting of steel rod specifications using nomogram

mass of the bridge girder and design seismic motion considering soil conditions.

Step 3: Plot the calculated equivalent natural period and yield seismic coefficient calculated in Step 1 on the nomogram selected in Step 2. Then, read off the required steel rod number and diameter from the nomogram to ensure that the response ductility factor and displacement remain within the specified limits.

Here, in the choice of limits, it is necessary to align the bridge span length to prevent collapse and consider the deformation capacity of the target bridge.

It should be noted that the applicability of this simplified steel rod specification setting method is limited to structural forms capable of being represented by the model shown in Fig. 3. Specifically, the target bridge must be modeled as a single-degree-of-freedom system, and certain conditions, where it is not inclined or its height is moderate, must be met. Additionally, if the bridge piers reach damage level 4 before reaching the target response displacement or exceed the allowable range of girder bearing movement, this method is not applicable.

4.3 Example of steel rod specifications set using nomograms

An example of steel rod specificaions set using nomograms is described in this section. Table 2 summarizes equivalent natural period (T_{eq}), yield seismic coefficient (K_{hy}), equivalent girder mass, and desired limits of a target bridge. By plotting the equivalent natural period T_{eq} and yield seismic coefficient K_{hy} from Table 2 on the nomogram (star mark in Fig. 14(a)), it is found that a steel rod diameter of 50 mm and the number of 4 rods satisfy the desired response displacement. Furthermore, Fig. 14(b) confirms that the chosen steel rod specifications also meet the desired response ductility factor. Finally, considering the ratio of girder mass to the nomogram's reference mass 1.5, we calculate that 6 steel rods are needed according to (8).

In summary, using nomograms allows us to gain a preliminary understanding of the necessary steel rod specifications for achieving target response displacement and response ductility factor before conducting detailed analyses.

5. Conclusions

In this paper, we present a design method for a narrow construction-compatible collapse prevention and seismic control device specifically suitable to steel railway bridges without a ballast floor. Our focus was laid on efficiently setting initial values for steel rod specifications before conducting detailed analyses. To achieve this, we created a model bridge with a one single-degree-of-freedom system and performed seismic response analyses by changing steel

Table 2　Information on the target bridge for which steel rod specifications are roughly set

Equivalent natural period T_{eq}(s)	0.7
Yield seismic coefficient K_{hy}	0.5
Equivalent mass m(t)	150
Target response displacement (cm)	30
Target response ductility factor	5
Desing seismic motion	L2 spectrum II (G3ground)

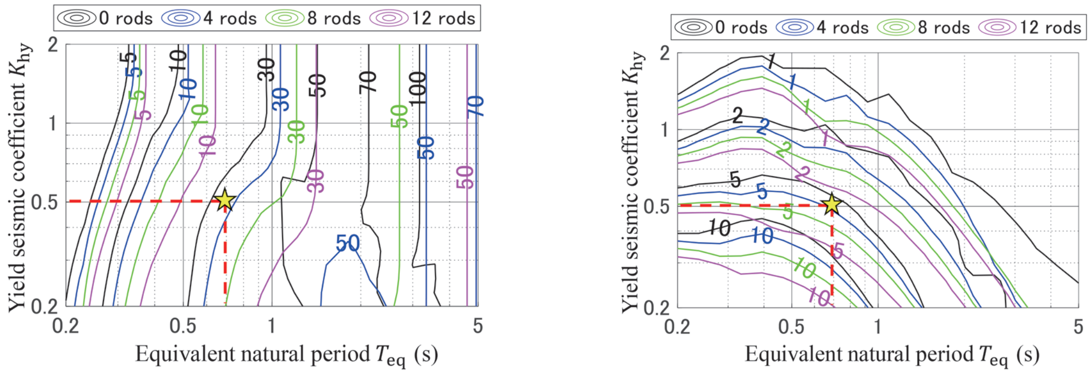

(a) Response displacement (unit : cm) **(b) Response ductility factor**

Fig. 14 Example of rough setting of steel rod specifications using nomogram (ϕ=50 mm, m=100 t)

rod specifications and bridge characteristics. The relationship between steel rod specifications and response displacement and response ductility factor was organized. Additionally, we constructed nomograms by which we calculated response displacement and the response ductility factor based on steel rod specifications and bridge characteristics. The findings of this paper are shown below:

- As the diameter and number of steel rods increase, the response displacement and response ductility factor of the bridge decrease. However, an excessive number of steel rods leads to elastic material like behavior, diminishing the impact of historical damping. Therefore, optimal conditions for efficient response reduction exist in terms of steel rod diameter and number.
- As girder mass increases, the reduction in response displacement and the response ductility factor due to the proposed device becomes less pronounced. There are limits to the bridges to which the proposed device can be applied.
- Considering the above trends, we constructed nomograms for calculating response displacement and response ductility factor based on equivalent natural period, yield seismic coefficient, girder mass, steel rod diameter and number. Using these nomograms, we can preliminarily estimate the required steel rod specifications to achieve target response displacement and response ductility factor before detailed analyses.

References

[1] Toyooka, A., Furuya, T., Nakata, Y. and Uno, M., "Seismic reinforcement of large-scale railway PC bridges using seismic isolation structure," *Proceedings of the 19th Symposium on Performance-Based Seismic Design of Bridges, etc.*, pp. 279-286, 2016 (in Japanese).

[2] Kita, N., Yoshida, K., Okano, M. and Seki, M., "Practical application of compression-type steel damping braces for railway viaducts," *Proceedings of JSCE F*, Vol. 63, No. 3, pp. 277-286, 2007 (in Japanese).

[3] Doi, T., Toyooka, A., Saito, M., Wada, K., Nanami, K. and Fukumoto, M., "Development of space-saving damping device with bridge collapse prevention function," *Proceedings of JSCE*, Vol. 79, No. 13, 22-13003, 2023 (in Japanese).

[4] Wada, K., Toyooka, A., and Kushiya, T., "Proposal of a simple design method of a damping device with bridge collapse prevention function installable in narrow spaces," *Proceedings of JSCE A1*, Vol. 78, No. 4, pp. I_152-I_161, 2022 (in Japanese).

[5] Toyooka, A., "A simple design method of the friction damper to meet the ductility demand," *Proceedings of JSCE A1*, Vol. 73, No. 4, pp. I_568-I_579, 2017 (in Japanese).

[6] Railway Technical Research Institute, *Design Standards for Railway Structures and Commentary (Seismic Design)*, Maruzen, 2012 (in Japanese).

Authors

Kazunori WADA, M.Eng.
Senior Researcher, Structural Dynamics and Response Control Laboratory, Center for Railway Earthquake Engineering Research
Research Areas: Earthquake Engineering

Takuma KUSHIYA, M.Eng.
Researcher, Steel & Hybrid Structures Laboratory, Structure Technology Division
Research Areas: Bridge Engineering

Akihiro TOYOOKA, Dr.Eng.
Director, Head of Center for Railway Earthquake Engineering Research
Research Areas: Earthquake Engineering

Evaluation of Impact of Volcanic Ash on Railway Electric and Signal Equipment and Proposal for Utilizing Information on Ash Fall

Yuichiro NISHIKANE **Takuya URAKOSHI** **Shoichi KAWAMURA**
Geology Laboratory, Disaster Prevention Technology Division

Natsuki TERADA
Signalling Systems Laboratory, Signalling and Operation Systems Technology Division

Takeshi KONISHI
Power Supply Laboratory, Power Supply Technology Division

Volcanic ash fall can seriously affect railway operations by causing problems such as track circuit shunting malfunctions and decrease in insulation performance of insulators. In this study, we experimentally investigated volcanic ash conditions that cause these problems. Results allowed us to clarify that 0.05 mm thick volcanic ash causes shunting malfunction, and that 1.2 mm thick volcanic ash containing saline water causes insulator flashover. Based on these results, we propose preventive actions which railway companies can implement to mitigate the effects of ash fall, using public information on eruptions.

Key words: *volcanic ash fall, shunting malfunction, insulator, Volcanic Ash Fall Forecasts*

1. Introduction

There are 111 active volcanoes in Japan. 50 volcanoes of these have been designated as particularly active and requiring continuous monitoring considering the possibility of eruption within the next 100 years and the impact of such an event on society [1]. Various phenomena associated with the volcanic activity, such as, ash fall, pyroclastic flow, and volcanic earthquakes can damage railways [2]. Among these phenomena, ash fall in particular affects railway operations across a wide area since volcanic ash is carried by wind over long distances.

Various types of damage to railways due to ash fall have been identified so far, including poor visibility, motor failure, and malfunction of tongue rails [2]. Track circuit shunting malfunctions due to accumulation of volcanic ash on the rails and decrease in the insulation performance of insulators due to adhesion of ash to the insulator surface, in particular, are important issues affecting the ability to keep railway transportation safe following an eruption. In this study, we conducted several tests to evaluate the degree of impact of ash fall on railway equipment depending on fallout conditions. First, we measured the electrical resistivity of volcanic ash to clarify its electrical properties. Secondly, we conducted track circuit tests and insulation performance tests to clarify the degree of impact of volcanic ash on track circuits and insulators, and the conditions under which volcanic ash affects track circuits and insulators. Finally, based on results of the tests, we propose preventive actions to be taken during ash fall. These actions will enable railway companies to mitigate the impact of the fallout using public information on eruptions, such as the Volcanic Ash Fall Forecast (VAFF).

2. Electrical properties of volcanic ash

2.1 Samples and methods

We collected six volcanic ash samples from four volcanos and prepared Toyoura sand for comparison, as shown in Table 1. Then, we measured the resistivity of the samples using new purpose-developed equipment (Fig. 1), considering water content. The electrical resistivity of the samples filled in the measurement vessel can be measured using the quadrupole method. The electrical resistivity ρ of the sample is determined as

Table 1 Volcanic ash samples

ID	Volcano	Explanation
Sa	Sakurajima	Ash of an eruption on Dec. 18, 2014. It was collected on Sakurajima Island within hours of the eruption.
Sb	Sakurajima	Ash from a storage pile at a volcanic ash storage site in Kagoshima City. The ash pile was kept outdoors for over a year before it was collected in 2014.
Aa	Mt. Aso	Ash of an eruption on Oct. 8, 2016. It was collected within 12 hours of the eruption.
Ab	Mt. Aso	Ash of an eruption on Oct. 8, 2016. It was collected on Oct. 13. There was rainfall between the eruption and the collection.
K	Mt. Kirishima	Ash of an eruption on Mar. 6, 2018. It was collected on Mar. 7.
F	Mt. Fuji	Ash and lapilli of the Hoei eruption in 1707. It was collected in Gotemba City, Shizuoka Prefecture.
T	–	Toyoura sand as a comparison.

$$\rho = \frac{A}{L}\frac{V_S}{V_R}R \qquad (\Omega\text{m}) \qquad (1)$$

where A (m^2) is the cross-sectional area of the filled sample in the measurement vessel, L (m) is the distance between the measuring

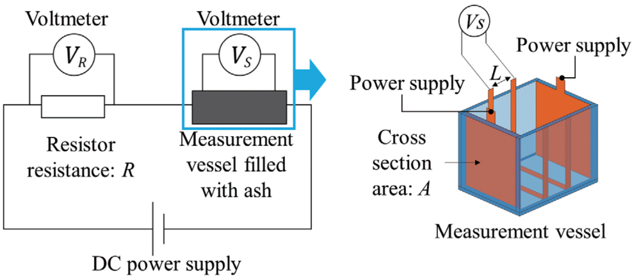

Fig. 1 Electrical resistivity measurement equipment

electrodes, R (Ω) is the resistance of the resistor, V_S (V) is the voltage between the measuring electrodes measured after one minute from the start of the power supply, and V_R (V) is the voltage between the electrodes of the resistor at the same time.

Additionally, we analyzed the electrical properties of volcanic ash suspension based on "Test Method for Electric Conductivity of Suspended Soils" (JGS 0212-2009), and "Test Method for Water-Soluble Components in Soils" (JGS 0241-2009).

2.2 Results and discussions

The results of the electric resistivity measurement of volcanic ash are shown in Fig. 2. The electrical resistivity is as high as 10^6 to 10^8 Ωm or more except for sample K, when the water content is less than 2%. It is noted that 10^8 Ωm is the measurement limit. In contrast, the electrical resistivity is 10^2 to 10^4 Ωm when the water content is 2.5%, and it decreases as the water content increases. For sample K, the tendency of the electrical resistivity to decrease with increasing water content is the same as for the other samples. However, its electrical resistivity is 10^3 Ωm when the water content is 0.2%. Furthermore, the electrical resistivity at a water content of 5% or higher is relatively high for the samples T and F, and relatively low for the other samples. At the water content of 20%, the difference in electrical resistivity for each sample except for the samples T and F is within about 10 times.

The results of electrical conductivity measurements and water-soluble component analysis of the suspension are shown in Fig. 3. The results of the water-soluble component analysis are shown as the total ion equivalent concentration eluted from 1 kg of dried volcanic ash. The electrical conductivity of the suspension is positively correlated with the total ion equivalent concentration, indicating that the more ions eluted from volcanic ash, the more easily the suspension conducts electricity.

Among the volcanic ash samples, those collected within a few days of eruption have relatively high electrical conductivity and total ion equivalent of the suspension. For example, in the case of volcanic ash from Sakurajima, sample Sa collected immediately after the eruption has higher electrical conductivity and total ion equivalent than sample Sb that has been stored outdoors for more than a year. This will be because the volcanic ash immediately after the eruption contains many water-soluble components, whereas water-soluble components were eluted from the volcanic ash exposed to rain for a long time.

Furthermore, Fig. 4 shows the cross plot between the electrical resistivity of ash with a water content of 20% and the electric conductivity of a suspension. Figure 4 clearly shows a negative correlation. It is thought that the difference in the electrical resistivity of the volcanic ash for each sample depends on the difference in the amount of ion elution, and that volcanic ash with a large ion elution has a lower electrical resistivity when the volcanic ash contains water.

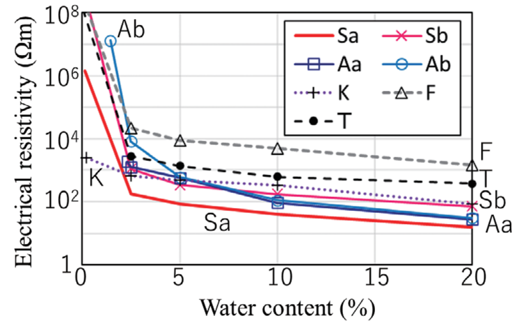

Fig. 2 Electrical resistivity of volcanic ash [3]

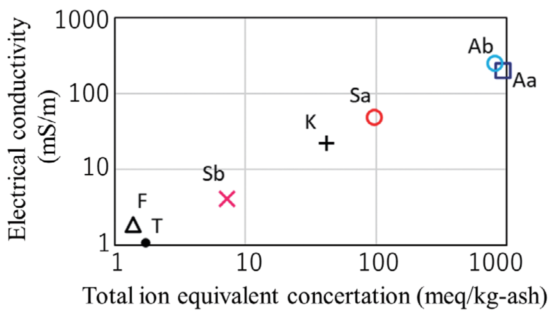

Fig. 3 Electrical conductivity and total ion equivalent concentration of volcanic ash (partly modified from [3])

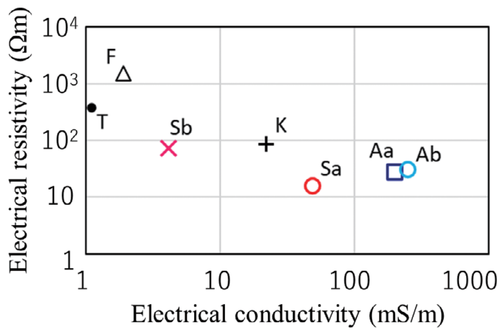

Fig. 4 Relationship between electrical resistivity of volcanic ash at a water content of 20% and electrical conductivity of suspension [4]

These results suggest that the extent of the electric influence of volcanic ash on electric apparatuses depends on the water content of the volcanic ash. Based on the results, we conducted an experimental study on track circuit shunting malfunctions that can occur with high electrical resistance of volcanic ash (Chapter 3), and decreases in insulation performance of insulators that can occur with low electrical resistance of volcanic ash (Chapter 4). In these experiments, we mainly used volcanic ash Sb from Sakurajima, which was collected in sufficient quantities. Since sample Sb has a relatively high electrical resistivity, it is assumed that the volcanic ash is likely to cause track circuit shunting malfunctions, and is unlikely to cause a decrease in insulation performance of insulators.

3. Track circuit tests

It is possible that volcanic ash on rails interferes with the energization between wheels and rails, leading to shunting malfunctions [2]. However, the relationship between shunting malfunction and thickness of ashfall has yet to be clarified. In this study, we configured a track circuit on a test track in RTRI and ran a train on rails scattered with volcanic ash to investigate the effect of volcanic ash on the track circuit [3] [5].

3.1 Methods

A simplified schematic figure of the track circuit test is shown in Fig. 5. Volcanic ash was scattered over the rails at a thickness set for each test case (Table 2) in a test segment which was 5-8 m long from the receiving end of a track circuit. A train was run on the track for each of these conditions. The residual voltage of the track relay and the state of the track relay (making contact or dropped) were measured while the train passed over the test track. An axle counter was used to determine the timing of the axle passage. The train coasted at a speed of 10 km/h while running through the test segment to prevent the volcanic ash from being blown away. The track circuit tests were conducted on a normal track circuit (commercial frequency circuit) and an electronic train detector (H type) which is used to control level crossings. The shunting sensitivity of the normal track circuit and electronic train detector on the test track are 0.12 Ω and 1.4 Ω, respectively.

Although volcanic ash Sb was mainly used in this study, other volcanic ash from Sakurajima collected at a different location was used for the case applying a 1 mm thickness of ash, to compensate for the lack of Sb. In addition to varying the thickness of the volcanic ash for each case, the tests were conducted in both dry and wet conditions. In order to wet the volcanic ash, water was sprayed on the rails after the volcanic ash was scattered. The water content of dry and wet volcanic ash was less than 1 % and between 5 and 26%, respectively.

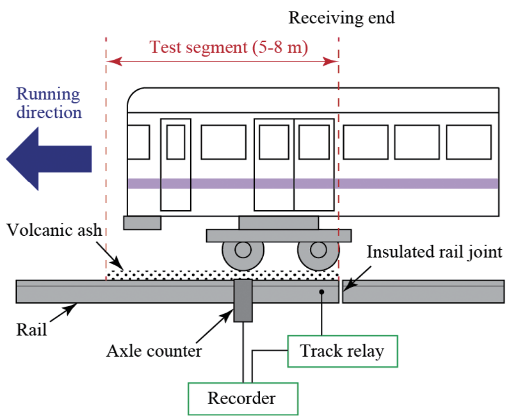

Fig. 5 Simplified schematic figure of the track circuit test (partly modified from [5])

Table 2 Test case of the track circuit test

Track circuit	Thickness of volcanic ash (mm)						
	0.01	0.025	0.05	0.1	0.2	0.5	1
Normal track circuit	D/W	D/W	D/W	D/W	–	D/W	D/W
Electronic train detector	D/W	D/W	D/W	D/W	D	–	–

D: Conducted under dry condition; W: Conducted under wet condition; –: Not conducted

3.2 Results

3.2.1 Normal track circuit cases

As examples of track circuit tests, Fig. 6 shows the results for (a) no volcanic ash, (b) 0.05 mm thick volcanic ash in dry conditions, and (c) 0.1 mm thick volcanic ash in wet conditions. In case (a), the track relay dropped away before the axle counter detected the first axle. On the other hand, in the case (b), the track relay did not drop when the axle counter detected the first axle, but dropped when the first axle left the test segment. This result shows that the

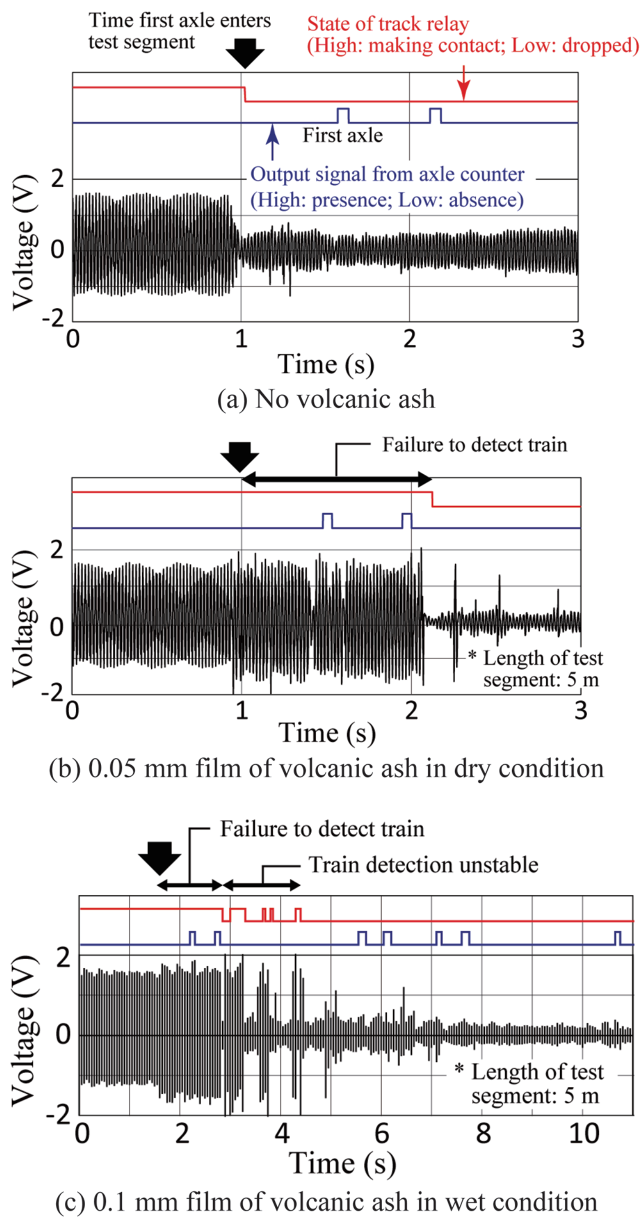

Fig. 6 Examples of results of track circuit tests (partly modified from [5])

track circuit in the test segment is not electrically shunted by the first axle since the volcanic ash interfered with the electrical conduction between the wheels and the rails. In case (c), the track relay did not drop while the first axle passed through the test segment, but the state of the track relay was unstable after the first axle left the test segment.

Table 3 shows the results of the track circuit tests. These clarify that volcanic ash of 0.025 mm thickness possibly makes the shunting of the track circuit unstable, and that volcanic ash of 0.05 mm thickness possibly causes shunting malfunctions. Additionally, in wet conditions, track circuit shunting failed or was unstable even after the train left the test segment. After the tests in wet conditions, volcanic ash adhered to the rails for several meters to 100 meters outside the test segment. The reason for this is that wet volcanic ash adhered to wheels and interfered with electrical conduction between the wheels and the rails even outside the test segment.

3.2.2 Electronic train detector cases

Table 4 shows the test results of the electronic train detector under each test condition of the track circuit tests. These clarified that volcanic ash of 0.025 mm thickness makes the shunting unstable, and that volcanic ash of 0.2 mm thickness causes shunting malfunctions. Since the shunting sensitivity of the electronic train detector is relatively high, the train detection of the electronic train detector is better than that of the normal track circuit.

3.3 Discussions

Volcanic ash accumulation to a thickness of 0.05 mm on rails for normal track circuits may cause shunting malfunctions. However, volcanic ash accumulation to a thickness of 0.2 mm on rails for electronic train detector, may cause shunting malfunctions. These tests were conducted in conditions where shunting failure would occur easily. It is therefore thought that even if a thicker layer of volcanic ash is deposited, shunting may in fact be successful. In particular, dry volcanic ash on rails would be easily blown away by a passing train.

Table 3 Test results of shunting function on normal track circuit against thickness of volcanic ash

Thickness (mm)	Train detection	
	Dry condition	Wet condition
0.1	Succeeded	Succeeded
0.025	Unstable	Unstable
0.05	Failed	Failed
0.1	Failed	Failed (unstable outside the test segment)
0.5	Failed	Failed (unstable outside the test segment)
1	Failed	Failed (failed continuously outside the test segment)

Table 4 Test results of shunting function of electronic train detector against thickness of volcanic ash

Thickness (mm)	Train detection	
	Dry condition	Wet condition
0.01	Succeeded	Succeeded
0.025	Unstable	Succeeded
0.05	Unstable	Unstable
0.1	Unstable	Unstable
0.2	Failed	(Not conducted)

4. Insulation performance tests

There is a possibility that volcanic ash adhering to insulators increases leakage current causing flashovers. Therefore, we conducted experimental study of the insulation performance of insulators with volcanic ash adhered to them [3] [6] [7].

4.1 Methods

We measured the insulation resistance of insulators with volcanic ash and the leakage current when single-phase AC voltage or DC voltage was applied to the insulators. The test circuit is shown in Fig. 7. Three types of insulators (A, B, C) were tested (Table 5). Insulators A and B are suspension insulators, and insulator C is a long rod insulator. For the suspension insulators (A and B), volcanic ash was adhered to them in the four patterns shown in Fig. 8, and for the long rod insulator (C), its upper horizontal surface was covered with volcanic ash (Fig. 9). Volcanic ash Sb was used, and the amount of volcanic ash per 1 m^2 of horizontally projected area of the insulator (hereinafter called "adhesion density") was set to 0.2 and 1.2 kg/m^2. Each adhesion density corresponds to thicknesses of 0.2 mm and 1.2 mm, respectively, assuming that the density of volcanic ash is 1 g/cm^3. Tap water was sprayed to adhere the volcanic ash to the insulators. Furthermore, in order to examine the risk of salt damage when both volcanic ash and salt adhere to the insulator, we also conducted a test in which 3% saline solution was sprayed instead of tap water.

4.2 Results and discussions

The measured insulation resistance and leakage current when AC voltage is applied to the insulators A and B are shown in Fig. 10.

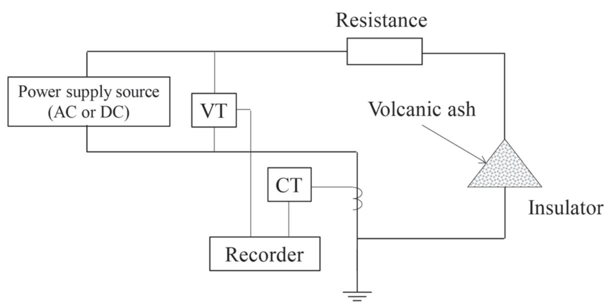

Fig. 7 Test circuit of the insulation performance test

Table 5 Insulators tested in the insulation performance test

ID	Type	Material	Explanation
A	Suspension	Ceramics	Long diameter: 180 mm
B	Suspension	Ceramics	Long diameter: 250 mm
C	Long rod	Ceramics	Number of sheds: 6

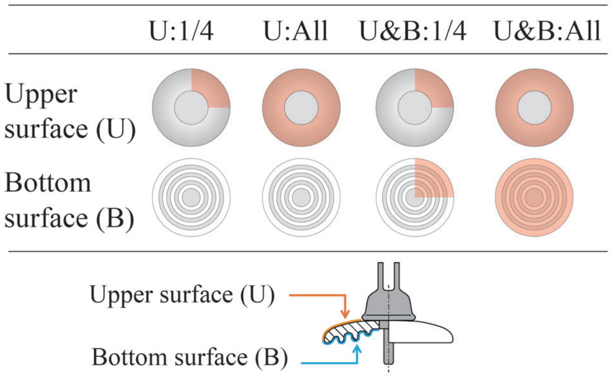

Fig. 8 Adhesion patterns of volcanic ash to suspended insulators

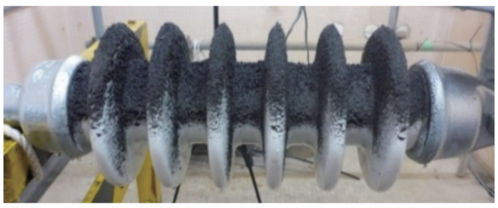

Fig. 9 Adhesion of volcanic ash to the long rod insulation [3]

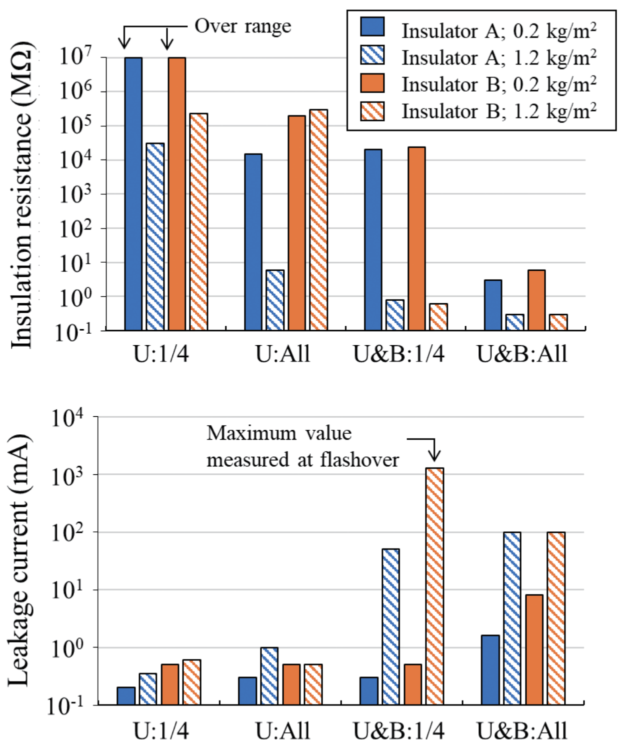

Fig. 10 Results of measurement of insulation resistance and leakage current

In these cases, while tap water was sprayed onto the insulators, 10 kV AC voltage and 20 kV AC voltage were applied to insulator A and to insulator B, respectively. As the adhesion area and adhesion density of volcanic ash increased, the insulation resistance decreased so that the decrease led to significant increase of the leakage current. For example, when volcanic ash was adhered to the entire upper and bottom surfaces of insulator A with an adhesion density of 1.2 kg/m^2, the insulation resistance was less than 1 MΩ, and the leakage current reached 100 mA when 10 kV AC voltage was applied. Thus, it was found that the insulation performance significantly deteriorated when volcanic ash was adhered to the entire upper and bottom surfaces of the insulator with the adhesion density of 1.2 kg/m^2. When volcanic ash was adhered to the 1/4 upper and bottom surfaces of insulator B with an adhesion density of 1.2 kg/m^2, electrical discharge occurred and led to a flashover. The leakage current in this case shown in Fig. 10 is the maximum value measured just before the test equipment stopped due to overcurrent. Based on these results, it is thought that insulators installed in conditions where volcanic ash can adhere to both sides, such as the insulators shown in Fig. 9, are at a relatively high risk of flashover.

Next, the test results when tap water was sprayed and those when saline water was sprayed are shown in Fig. 11. The conditions of these tests are shown in Table 6. Comparing the results of the cases using tap water with those using saline water, it was found that the latter tended to have lower insulation resistance and larger leak-

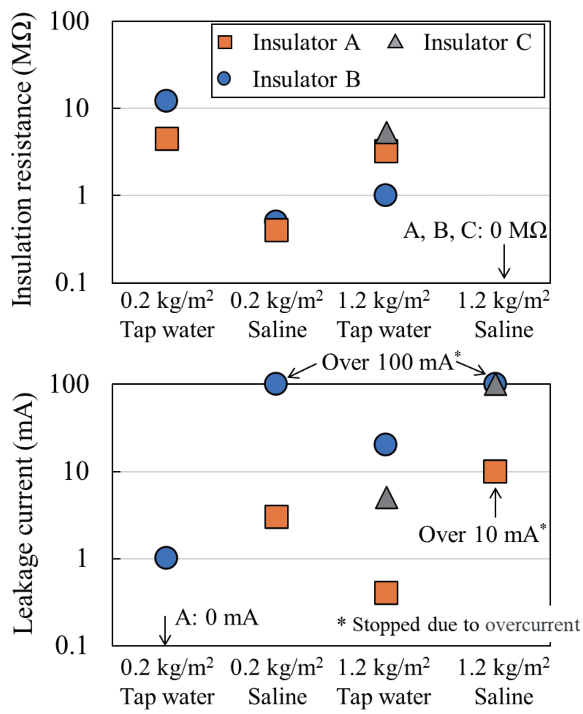

Fig. 11 Results of measurement of insulation resistance and leakage current when tap water or saline water were sprayed (partly modified from [3])

Table 6 Conditions of the insulation performance test shown in Fig. 11

Insulator	Applied voltage	Adhesion area of volcanic ash	Adhesion density
A	1.8 kV DC	Entire upper and bottom surface	0.2, 1.2 kg/m^2
B	10 kV AC	Entire upper and bottom surface	0.2, 1.2 kg/m^2
C	10 kV AC	Upper surface	1.2 kg/m^2

(a) Insulator B (adhesion density of 1.2 kg/m^2; saline water)

(b) Insulator C (adhesion density of 1.2 kg/m^2; saline water)

Fig. 12 Examples of situations where discharge occurred during the tests [3]

age current. Furthermore, when tap water was sprayed, although discharge occurred in cases at the adhesion density of 1.2 kg/m^2, no discharge occurred in all cases at the adhesion density of 0.2 kg/m^2. On the other hand, when saline water was sprayed, discharge occurred in all cases regardless of the adhesion density. Figure 12 shows examples of discharge which occurred during the tests. Based on these results, it is thought that if volcanic ash adheres to insulators in coastal areas, the risk of flashover will be relatively high.

5. Mitigation of influence of ash fall on railways by utilizing public information

There are two publicly available ash fall maps: the ash fall hazard map issued by the Commission on Mitigation of Volcanic Disasters and the VAFF issued by the Japan Meteorological Agency. The former hazard maps show expected areas of volcanic ash accumulation by thickness based on results of simulation, in which past eruptions and assumptions about eruption scale, wind direction, and wind speed. By using these sources of public information, it is possible to predict locations with a relatively high risk of ash fall.

The VAFF gives three types of information: Scheduled, Preliminary and Detailed Forecasts [1]. The Scheduled Forecasts are issued periodically when there is risk of an eruption. The Preliminary Forecasts and the Detailed Forecasts are issued within 5–10 minutes and 20–30 minutes of the start of an eruption, respectively. The assumed areas of ash fall in the Preliminary Forecast and the Detailed Forecast are categorized into thickness levels: Low (0.0001 to 0.1 mm), Moderate (0.1 to 1 mm) and Heavy (over 1 mm). The results of tests in Chapters 3 and 4 with the category of thickness are shown in Fig. 13. Based on Fig. 13, it is thought that there is a risk of track circuit shunting failure and insulator flashover in assumed areas of “Heavy” ash fall. On the other hand, these risks are thought to be

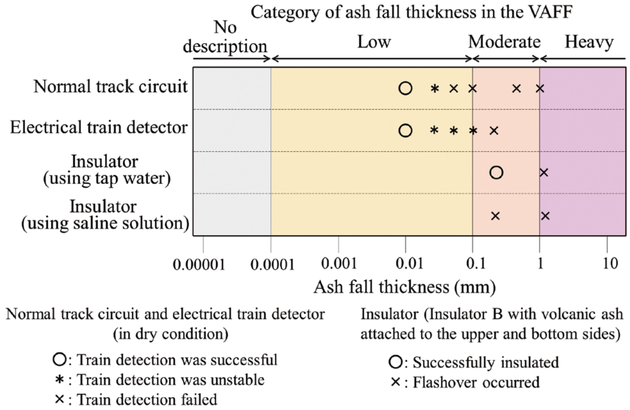

Fig. 13 Results of tests in Chapter 3 and 4 with the category of ash fall thickness in the VAFF (partly modified from [3])

small in areas where assumed area of ash fall is not described in VAFF. However, since volcanic ash Sb has a relatively high electrical resistivity, it is assumed that the volcanic ash is likely to cause track circuit shunting failure, but is unlikely to cause insulator flashover.

Based on the results of our tests, we propose some preventive actions which railway companies can implement, in normal conditions and in case of ash fall, to mitigate the impact of fallout impact on railways, using public information (Table 7). In normal situations, ash fall hazard maps are useful for railway companies to recognize areas that are affected by volcanic ash. This assumption is usable for determining where to deploy cleaning equipment to remove volcanic ash. When a volcanic warning is issued, railway companies can strengthen their emergency contact system and con-

Table 7 Examples of possible preventive action by railway companies using public information on ash fall (partly modified from [5])

Timing	Public information	Prevention actions of railway companies
Normal situation	Ash fall hazard map	Recognize areas affected by ash fall.
		Determine where equipment to clean volcanic ash should be deployed.
		Check type of track circuit, presence or absence of crossing back-up devices.
Volcanic warning	Volcanic Alert Level	Establish headquarters and strength emergency contact system.
	VAFF (Scheduled)	Dispatch workers and equipment for cleaning volcanic ash.
After eruption	VAFF (Preliminary, Detailed)	Inspect facilities.
After ash fall	VAFF (Detailed)	Determine timing and range of volcanic ash cleaning work.

firm their actions at the time of ash fall. However, it should be noted that an actual eruption might occur before a volcanic warning is issued. After an eruption, railway companies can utilize VAFFs for narrowing assumed areas of ash fall and then visually confirm actual ash fall conditions. Considering the thickness of volcanic ash, they can forecast possible crises and examine how those situations might be handled, such as carrying out inspections or cleaning facilities.

6. Conclusions

We experimentally examined the electrical properties of volcanic ash and the impact of volcanic ash on track circuits and insulators. The results of these examinations are described below.

1) The electrical resistivity of volcanic ash is 10^6 Ωm or more when the water content is less than 2%, whereas about 10 to 100 Ωm when the water content is 20%.

2) Volcanic ash thickness of 0.025 mm causes instability in normal track circuit shunting, and when the thickness reaches 0.05 mm, track circuit shunting fails.

3) 1.2 mm thick volcanic ash containing saline water causes insulator flashover.

Based on these results, we proposed preventive actions, which railway companies can implement based on publicly available information on eruptions, to mitigate the impact of ash fall. We think that this study can be useful for railway companies to develop disaster prevention plans.

Acknowledgment

Dr. Kazunori Watanabe of the Aso Volcano Museum provided us with some of the volcanic ash samples. The authors would like to express their sincere gratitude to him.

References

[1] Japan Meteorological Agency, “Volcanoes,” https://www.jma.go.jp/jma/kishou/books/kazan/kazan.pdf (Accessed: 23 May 2024).

[2] Urakoshi, T., Nishikane, Y., and Kawagoe, T., “A case study of disasters due to volcanic activities and countermeasures against them in railway of Japan,” *RTRI report*, Vol. 29, No. 1, pp. 47-52, 2015 (in Japanese).

[3] Urakoshi, T., Kawamura, S. et al.., “Electrical properties of volcanic ash and its effect on track circuits and insulators,” *The journal of Japan Railway Civil Engineering Association*, Vol. 57, No. 10, pp. 59-62, 2019 (in Japanese).

[4] Urakoshi, T., Nishikane, Y. and Kawamura, S., “Resistivity of volcanic ash and its relation to chemical composition,” in Ohta, T., Ito, T., Osada, M., “Rock mechanics and engineering geology in volcanic fields,” *CRC Press*, pp. 34-41, 2022.

[5] Nishikane, Y., Terada, N. et al., “Volcanic ash impacts on railway signal facilities and utilizing of the Volcanic Ash Fall Forecast,” in Ohta, T., Ito, T., Osada, M., “Rock mechanics and engineering geology in volcanic fields,” *CRC Press*, pp. 107-113, 2022.

[6] Hirakawa, S., Konishi, T. and Nishikane, Y., “Verification of performance for the insulator with volcanic ash for electric railway,” *2018 Annual Meeting Record IEEJ*, No. 5-246, pp. 406-407, 2018 (in Japanese).

[7] Konishi, T., Hirakawa, S., and Nishikane, Y., “Experimental study of deterioration for the insulator with volcanic ash in electrified railway,” *Proceedings of the 2018 Annual Conference of Power and Energy Society IEEJ*, pp. “9-3-19” – “9-3-20,” 2018 (in Japanese).

Authors

Yuichiro NISHIKANE
Assistant Senior Researcher, Geology Laboratory, Disaster Prevention Technology Division
Research Areas: Engineering Geology

Takuya URAKOSHI
Senior Researcher, Geology Laboratory, Disaster Prevention Technology Division
Research Areas: Ground Water, Engineering Geology

Natsuki TERADA, Dr.Eng.
Senior Chief Researcher, Signalling Systems Laboratory, Signalling and Operation Systems Technology Division
Research Areas: Signalling Systems, Track Circuit, Automatic Train Control Systems

Shoichi KAWAMURA
Assistant Senior Researcher, Geology Laboratory, Disaster Prevention Technology Division
Research Areas: Engineering Geology

Takeshi KONISHI, Ph.D.
Chief Researcher, Power Supply Laboratory, Power Supply Technology Division
Research Areas: Power Supply Systems

PAPER

Development of On-board-based Autonomous Train Control Systems

Takayasu KITANO
Train Control Systems Laboratory, Signalling and Operation Systems Technology Division

Kazumasa KUMAZAWA
Transport Operation Systems Laboratory, Signalling and Operation Systems Technology Division

Hiroyuki FUJITA **Yoichi SUGIYAMA**
Train Control Systems Laboratory, Signalling and Operation Systems Technology Division

As a basic technology for realizing autonomous train operation, we propose two functions: a function for creating a running profile on board a train and a function for creating a running profile on board to recover from delays caused by hazards. Running profiles are generated based on information such as timetables. The function for direct control of ground equipment from a train is designed to allow on-board equipment to set train routes, control turnouts on that route, and control level crossing warnings as trains approach.

Key words: *autonomous train operation, autonomous train control, running profiles, on-board path control, level crossing warning control*

1. Introduction

Autonomous operation [1], which is being researched and developed by the Railway Technical Research Institute as an advanced form of automatic operation, aims to realize more flexible train operation in addition to improving safety with as little ground equipment as possible. To make autonomous operation a reality, technology is needed to enable individual trains to safely control their own speed, while at the same time controlling ground facilities such as level crossings by monitoring the operating status and the conditions on and along the railway line. In particular, the autonomous train control system is the foundation for autonomous operation, and it is necessary to establish a technology to systematize train operation functions including handling, which has conventionally been left to train drivers and on-board staff, after installing as many functions as possible on the train. The authors are therefore working on the development of a control system in which train control functions are integrated into on-board equipment and each train can autonomously determine its course and speed (hereafter referred to as an autonomous train control system).

In this paper, as basic technologies for configuring an autonomous train control system, a function to automatically create a running profile train schedule by on-board equipment and a function to directly control ground equipment from the vehicle are proposed. The results of trial calculations of the effects of each function are reported. Chapter 2 presents an overview and configuration of the autonomous train control system, Chapter 3 describes the function for creating a running profile on board, and Chapter 4 describes the function for direct control of ground equipment from the vehicle.

2. Overview of autonomous train control systems

2.1 Autonomous train control system configuration

In autonomous operation, it is fundamental that trains can run independently. However, in several areas such as urban areas where several lines are concentrated, or in line sections with high train density, it is necessary to monitor and manage the operation of trains in a wide area to ensure smooth operation within the area or the entire line section. For this reason, the authors envisage the following two types of system configuration for autonomous operation, depending on transport demand.

(1) Trains run independently and autonomously

Each train creates a running profile and configures its path based on the previously input timetable information and dynamic map, and its own train position and speed, and then controls the turntable and level crossing from on-board [2].

(2) Ground-based support for the autonomous train operation

A device that aggregates and distributes information related to train operations, which is called supervisor, is installed centrally on the ground, and the supervisor aggregates information on train movements, passenger flows, dynamic maps and maintenance for the entire line section as shown in Fig. 1. Based on the train schedule information provided by the supervisor, each train creates a running profile and configures its path, as in (1) above, and controls the point-machine and level-crossings from the vehicle.

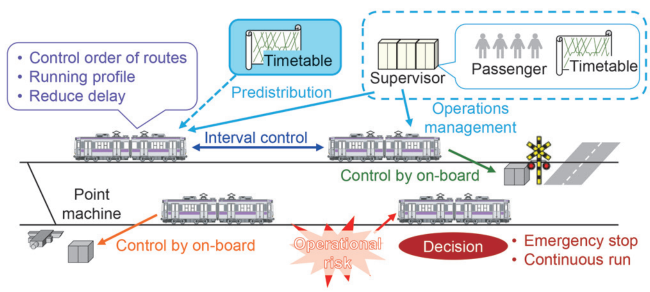

Fig. 1 Autonomous train control

2.2 Functions of a train control system in which trains run autonomously

This section presents the functions required for an autonomous train control system based on the configuration presented in Section 2.1. Autonomous on-board control is assumed in the case of normal running and when an abnormality occurs. During normal operation, the train creates a running profile by configuring the route based on the timetable information on board the train, and directly controls the point-machine and level-crossings on the path (Fig. 2(a)). When a train that has stopped due to the detection of an obstruction along the line resumes operation, a running profile is created to recover from the delay (Fig. 2(b)).

Based on above, the main functions of an autonomous train control system are as follows:

(1) Generate a running profile on board the train according to the on-board timetable information at the time of train departure
(2) Ensure a safe path for the train
(3) Direct on-board control of ground equipment, such as point-machine and level crossing controllers
(4) Develop a running profile that allows for delay recovery when resuming operations after a train has been stopped due to roadside obstruction detection, etc.

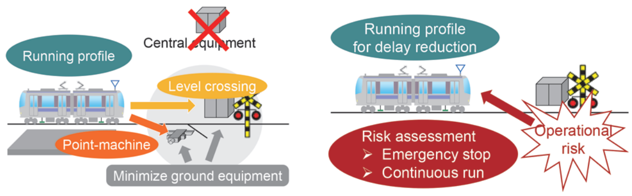

(a) Normal running conditions (b) Hazard occurrence

Fig. 2 Main functions of autonomous train control system

2.3 Equipment configuration

As shown in Fig. 3, the proposed system consists of on-board equipment and ground equipment, to implement autonomous control on the vehicle. The on-board equipment, on-board DB registering vehicle performance and track information and radio equipment are mounted on the vehicle to create a running profile, set the route and control level crossings. The ground equipment installed on site consists only of a point-machine and control unit for level-crossings.

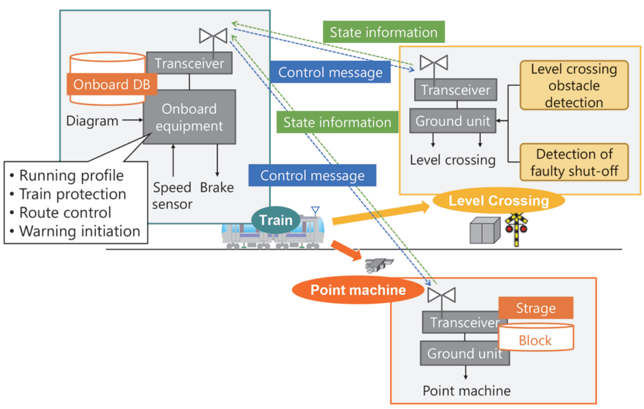

Fig. 3 Equipment configuration of an autonomous train control system

3. Creation of running profiles in on-board equipment

Each train creates a running profile based on the train schedule, which is acquired and held by the on-board equipment, and runs according to that running profile. This extends the function of timed operation in automatic operation, i.e. running trains according to the arrival and departure times at each station set in the train schedule.

In conventional automatic operation, a running profile is created in advance and the train runs according to that running profile [3][4]. In contrast, in autonomous train control systems, the running profile is created and updated on board the train before departure from the first station in order to respond flexibly to changes in the train schedule, etc. If the train stops between stations due to emergency stop information for example, the train itself recreates the running profile and continues its operation.

This chapter described two functions for realizing running profile creation on-board an autonomous train control system: running profile creation based on the train schedule and running profile creation for recovery operation after an emergency stop.

3.1 Ability to create running profiles based on train schedules

The method for creating running profiles based on train schedules is based on [5]. The first step is to create a running profile that is based on running with the shortest possible time between stations and then applying processes such as reducing the maximum speed between stations to create a running profile that satisfies the running time between stations specified in the train timetable. The running time between stations is calculated from the arrival and departure times of each station shown in the train schedule. The advantage of this method is that it can instantly create a running profile between stations for each train. Therefore, this method was applied to an autonomous train control system and an algorithm was developed to create a running profile on board.

The algorithm proposed for creating specific running profiles is shown below.

a) Extract the arrival and departure times and arrival and departure numbers of each station from the train schedule and then calculate the running time t1 between stations (Step 1).
b) Create a running curve for the shortest journey time between stations from the track data (stop position, gradient, speed limit, etc.) and vehicle data (pulling force, train length, running resistance, etc.) recorded on board the vehicle (Step 2).
c) Compare the running time t2 between stations in the running curve created on board with the running time t1 in (1), and when the difference is greater than the threshold (t1-t2>T), reduce the maximum speed between stations and create the running curve again (Step 3).
d) Repeat process Step 3 with the re-created running curve.
e) When t1-t2 ≤ T, the running curve is fixed as the running profile between stations (Step 4).

An image of the above algorithm is shown in Fig. 4. The algorithm assumes a stop at each station, but even in the case of passing trains, it can be adapted by taking into account the pursuit interval, which indicates the interval between train arrivals at a station at (ii). [6]

3.2 Function for creating running profiles for recovery operation after an emergency stop

Unlike automatic operation, the goal of an autonomous train control system is to enable trains to autonomously determine when a situation allows for service to be resumed and run to the next sta-

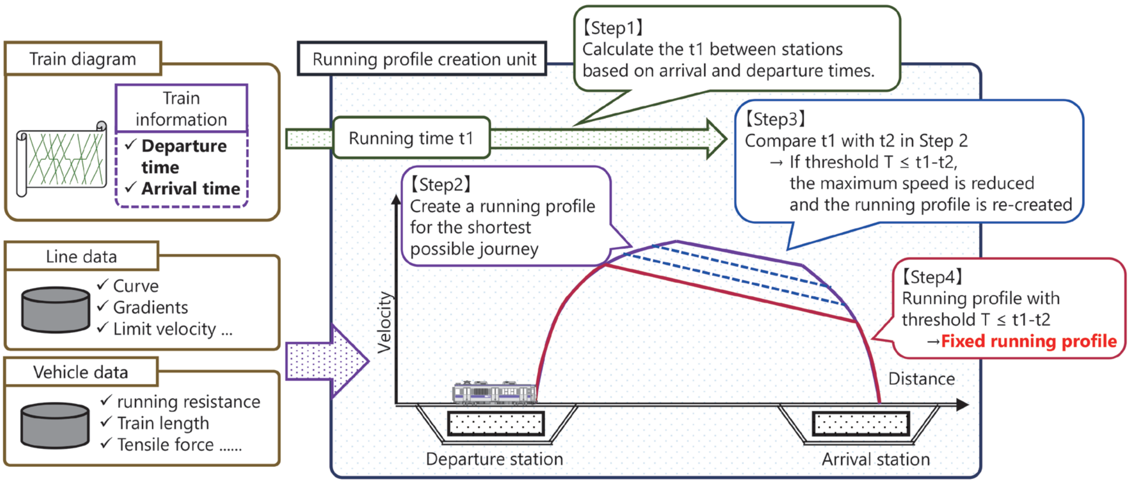

Fig. 4　Running profile creation function based on train timetables

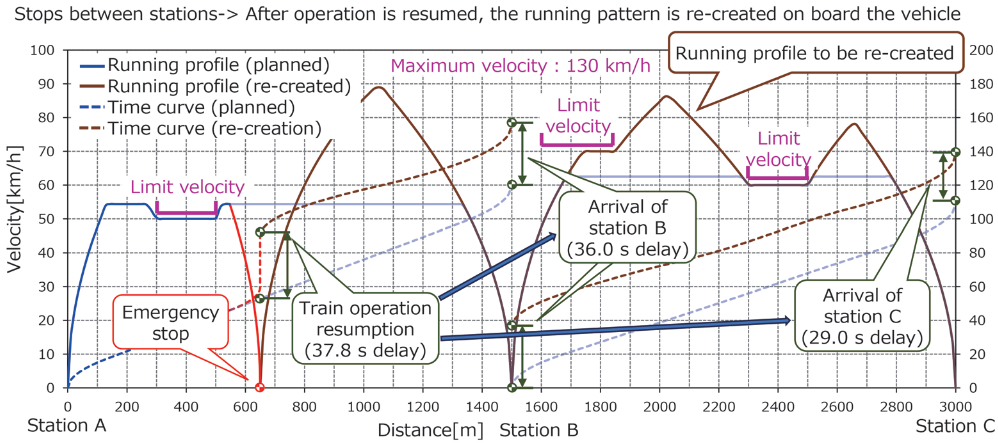

Fig. 5　Running profile creation function based on train timetables

tion even when they are stopped between stations due to emergency stop information, for example. When a train stops between stations, it is necessary to create a new running profile from the point where the train has stopped to the stopping position at the next station, because there is a gap between the running profile created when the train left the station and the actual running profile. In addition, the running time between stations increases due to train stops between stations, resulting in delays. Therefore, by extending the function for creating running profiles based on train timetables, we have developed a function for creating running profiles that autonomously recover from delays after resuming operation. The functions for re-creating running profiles and recovering train delays are described below.

3.2.1 Recreating the running profile

When a train stops between stations, the stopping point of the train becomes the new starting point after resumption of operations. Therefore, the stopping point is regarded as the starting station in the running profile generation described in Section 3.1 and the running profile is re-created. However, in order to recover from train delays, the following process is used.

a) The running curve with the shortest running time is used as the running profile (even if the train arrives at the next station earlier than the train schedule, the processes c) and d) in Section 3.1 are not carried out).
b) When the scheduled departure time at the next station is later than the departure time on the train timetable, a shortest running profile is applied between the next station and the station beyond.

3.2.2 Recovering delays by adjusting stop times

A typical train timetable, the minimum stopping time is defined at each station including some margin. Therefore, the autonomous train control system also attempts to recover from delays by utilizing this stopping time, depending on the train delay situation. Specifically, when a delay occurs, the arrival time at the station is compared with the departure time planned in the train schedule, and when the difference satisfies the minimum stopping time, the train departs from the target station according to the planned departure time [6]. However, when the minimum stopping time cannot be met, the arrival time at the target station plus the minimum stopping time is updated as the departure time at that station.

3.3 Verification of delay recovery effect

The running profile generated by the proposed method and its delay recovery effect are estimated in Fig. 5, using the case where an emergency stop occurs while the train is running, resulting in a delay. In this example, the running time between stations A and B is defined as 120 s and between stations B and C as 115 s in the train schedule. When the train departs from a station, the developed function creates a running profile on board corresponding to the running time, which is the blue line in Fig. 5. The train stops 650 m into its journey due to emergency stop information, which creates a significant gap with the previous running profile and a delay of approximately 38 seconds. When the cause of the emergency stop is resolved and the train resumes service, the proposed method recreates the running profile such that the delay is recovered, represented by the orange line in Fig. 5.

When the train runs according to this running profile, the delay is restored by approximately 2 seconds at station B and 9 seconds at station C. From this, it can be said that the re-created running profile also contributes to delay recovery. However, in order to simplify the verification process, it was decided that the train would run at constant speed without coasting when the speed limit, including the maximum speed, was reached.

4. Ground equipment control from the vehicle

4.1 Path and point-machine control from the vehicle

4.1.1 Proposals for independent route and point-machine control

In this section, a function is proposed whereby the train itself controls the point-machine related on its route, based on the position and route of other trains. The concept of the function is that only the on-board equipment that has been instructed to lock the point-machine can unlock it. The ground unit switches the point machine under the instructions of the on-board equipment.

4.1.2 Equipment configuration

This function is achieved by the ground control unit, which controls the on-board equipment and the field equipment, as shown in Fig. 6. The ground control unit is connected only to the point-machine and controls it. The ground control unit stores information on the position and route of the train. The on-board equipment, on the other hand, is connected to the dispersed ground control units and exercises independent control. The control information transmitted between devices is sequentially transmitted between the nearest devices (on-board devices and ground control units or between ground control units) as required. The transmission path between devices is not limited to a specific line, and it is assumed that a transmission line that can establish information transmission between the nearest devices is used.

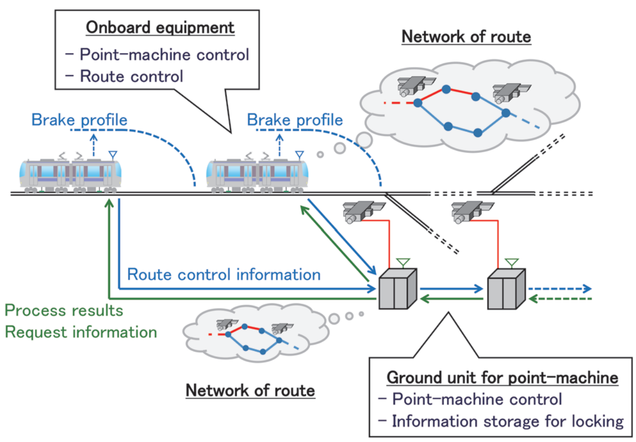

Fig. 6 Route control and point-machine control from the vehicle

4.1.3 Knowing the position and route of other trains and controlling the point-machine

The on-board equipment transmits and receives control messages to and from the ground control unit to control the route of the train. In order to secure the route of its own train, the on-board equipment transmits the train position and route control information to the ground control unit nearest to the front of the train. The ground control handles processing based on the received path control information and returns the processing results and requested information to the on-board equipment concerned, and also transfers the same information to the adjacent ground control unit on the inward side of the route. This transfer process is repeated until it reaches the ground control unit corresponding to the end of the route, so that information is shared between the on-board equipment and the ground control units concerned. The on-board equipment requests to secure the route can acquire the route status of other trains, the status of the preceding train and the status of the equipment from the information returned by the ground control equipment.

And based on this, the on-board equipment determines the route that it can secure and then secures the route, converts the point-machine and locks the point-machine. Only the on-board equipment that secures and locks the track and the point-machine can unlock them, thereby enabling exclusive control over other trains. The on-board equipment that has secured the route and locked the point-machine can run to the outside of the safe running point as a guarding point to ensure safety [2].

4.2 Level crossing control from the vehicle

4.2.1 Radio-based level crossing warning control

In autonomous train control systems, the basic concept of level crossing control is similar to the level crossing control in radio train control systems shown in Fig. 7.

The level crossing warning control in wireless train control systems is designed to start the warning at a position where a set warning time can be ensured when the train is accelerating towards the level crossing at a maximum acceleration at any speed. This allows the warning start position to be set further inwards when approaching at low speeds, reducing unnecessary warning time compared with the current fixed position warning control. However, the current mechanism for starting the warning in radio train control at level crossings assumes manual operation by the driver, so the warning is controlled at the maximum acceleration so that the driver does not have to limit

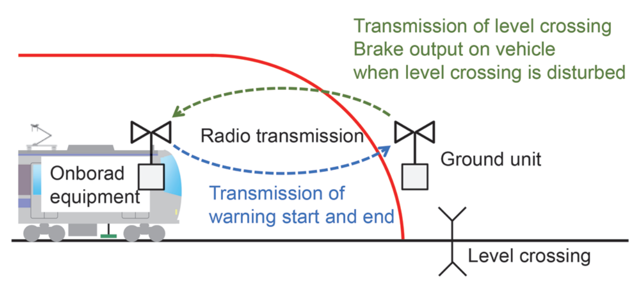

Fig. 7 Radio-based level crossing control.

the maneuvering after the warning has been started. Therefore, it is not a constant-time warning control in the original sense.

4.2.2 Warning control functions

First, the on-board equipment calculates an expected time of arrival at the level crossing based on train speed and position in the running profile. This is used to determine a 'trigger' position to initiate the warning for closure of the level crossing ('warning start profile'). When the train reaches this position information to initiate the warning is transmitted by the on-board equipment to the level crossing. Figure 8 shows a warning start profile. To calculate the warning start profile, a value obtained by adding two other values is used: the radio transmission delay time as a margin to the set warning time and adding the fluctuation range of the speed detection sensor to the speed information of the running profile. Furthermore, an overspeed prevention profile is provided to prevent the actual train speed from exceeding the pre-set running profile and to prevent the warning time from being insufficient.

For level crossings related to station departure conditions, such as level crossings located in the station departure direction, the arrival time to the level crossing is calculated from the running profile, and departure is deterred for the missing time to prevent the warning time from being insufficient. For example, when the arrival time at a level crossing is 10 s short for set warning time, warning is started 10 s before the scheduled departure time from the station.

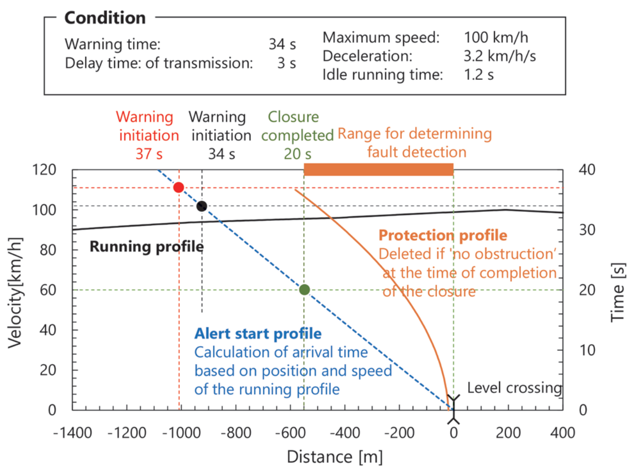

Fig. 8 Overview of warning control and train protection functions

4.2.3 Train protection functions

The on-board equipment generates a protective profile on the train at level crossings based on information such as brake deceleration and position of level crossing position registered in the on-board DB, as shown in Fig. 8 [7]. When the train speed exceeds the protection profile speed, the system automatically releases the service or emergency brake.

In normal conditions, the system receives 'no obstruction detected' as status information from the level crossing in addition to closure complete status, and then the protective profile is deleted. On the other hand, when there is an obstruction at a level crossing, the system receives 'Obstruction detected' and maintains the protection profile to ensure that the train stops before the level crossing. However, if the obstruction is detected just before the train enters the level crossing, the train may not be able to stop before the level crossing depending on the time of detection. At this point, as soon as the 'obstruction detected' is received, the protective profile is reinstated and the emergency brake is applied. The protective profile is designed taking into account the vehicle's brake deceleration, idle time, and the set warning time to ensure that normal operation is not affected when the closure of the level crossing is completed.

In an autonomous train control system, resuming operations after a stop due to a protection profile is also performed automatically. In particular, when it is judged that there are no obstacles to resuming operation, by combining information from various sensors on board the train and on the ground, it is important to have a function to erase the protective profile or generate a speed-restriction profile. In addition, it is possible to envisage situations where, for example, a level crossing that has begun to close may have to reopen because of a major delay or if service is suspended. However, in these situations, the concept of station departure should be applied and, if necessary, a departure deterrent should be applied to prevent insufficient warning time.

4.3 Verification of the effectiveness of warning time reduction

The effect of the proposed level crossing warning control system (running profile system) on reducing warning time was compared with the current fixed position warning control system (current system) and the level crossing warning control system in radio train control systems (maximum acceleration system). The warning times were estimated for three different cases: acceleration, constant speed where the speed change is less than 10 km/h and deceleration. As a case study, a simulated running profile between stations was created using SPEEDY which is an system for creating running profiles, with position and speed information given as data approximately every 10 m. Three level-crossings for verifying the performance of each system were tested: 1,101 m as acceleration case, 3,064 m as constant speed case and 5,200 m as deceleration case, and the warning time was set to 34 s for each case. The vehicle performance was set to a maximum speed of 100km/h and a maximum acceleration of 2.0 km/h/s. A margin of 3 seconds was set in consideration of transmission delays due to wireless communication between the vehicle and the level crossing, and a value of 2 km/h was added to the running profile as the fluctuation range of the speed detection sensor when calculating the running profile. The results of the warning time calculations are shown in Fig. 9 and Table 1.

The warning time of the current system is calculated with the maximum speed and therefore varies depending on the running profile. Therefore, although the warning distance is a constant value of 945 m at 100 km/h, 34 s, in the maximum acceleration method, a shortening effect is obtained in acceleration cases where the approach speed is low. However, for approaches near the maximum speed, the warning time is extended by, for example, the transmission delay margin, compared with the current method. On the other hand, in the running profile system, a margin of 3 s for transmission delay and a speed margin of 2 km/h which is about 1 second are added. Nevertheless, in all cases, the warning starts at 38 s.

Therefore, if a running profile can be obtained in advance, as in the system proposed here, the running profile method can improve the accuracy of the constant-time control and contribute significantly to reducing the warning time.

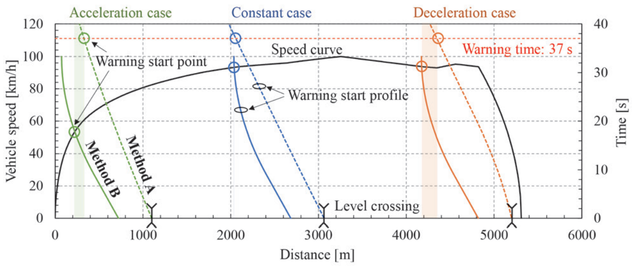

Fig. 9 Warning time calculation results and running profiles

Table 1 Results of warning time calculations

Trial case		Running profile method	Maximum acceleration method	Existing system
Acceleration	Point of warning	778 m	880 m	945 m
	Warning time	38 s	45 s	50 s
Constant speed	Point of warning	1014 m	1024 m	945 m
	Warning time	38 s	38 s	35 s
Deceleration	Point of warning	860 m	1025 m	945 m
	Warning time	38 s	45 s	42 s

5. Conclusion

This paper proposed functions and equipment configuration for an autonomous train control system developed for autonomous train operation. Specifically, the method's concept and its implementation aim to provide a function that allows on-board setting of train routes and running profiles based on the train's running position and speed, directly controls ground facilities such as turnouts and level crossings. This paper also describes the results of a trial calculation to evaluate the effectiveness of the function.

Enabling the on-board generation of running profiles allows trains in operation to automatically generate a running profile following a disruption such as a delay. This enables train operations to recover autonomously from, for example, delays caused by stopping between stations because of emergency stop information. In addition, the on-board train path and turnout control function makes it possible to run trains safely without installing a central control unit on the ground. Furthermore, the proposed level crossing control method also enables the automatic control of level crossing closure based on running profiles and the automatic control of resumption of operations if a train stops because of the generation of a protective measure in its running profile.

In future, prototype on-board and ground equipment equipped with the functions of an autonomous train control system and the ability to make operational decisions in response to hazards will be tested to verify the feasibility and effectiveness of autonomous train operation.

References

[1] Kawasaki, K., "Autonomous train operations and improved convenience and efficiency," *RRR*, Vol. 76, No. 1, pp. 12-15, 2019 (in Japanese).

[2] Soga, K., Sugiyama, Y. and Sakurai, Y., "Safety verification of autonomous path control in an operation system mainly controlled from the vehicle," *IEEJ Industrial Applications Division Conference*, 2022. (in Japanese).

[3] Kimura, A., "Proposal of a Timed Operation Control for Electric Vehicles Using Time-Position Profiles," *IEEJ Transactions D*, Vol. 119, No. 7, pp. 942-949, 1999. (in Japanese).

[4] Oya, J., Iba, S. and Nakazawa, H., "Automatic Train Operation System for Subway Trains," *Toshiba Review*, Vol. 63, No. 12, pp. 41-45, 2008. (in Japanese).

[5] Takeuchi, Y., Sakaguchi, T., Kumazawa, K., Kunimatsu, T. and Sato, K., "Improvement of Train Operation and Passenger Flow Simulator for Detailed Estimation of Train Movement on High Frequency Railway Lines," *Quarterly Report of RTRI*, Vol. 56, No. 1, pp. 39-44, 2015.

[6] Kumazawa, K., Toyama, T., Oko, N. and Ono, Y., "Operation profile generation method based on pursuit intervals," *2022 IEEJ National Convention*, 2022 (in Japanese).

[7] Fujita, H., Takasaki, K., Shindo, T., Issiki, R., Soga, S. and Kitano, T., "Study of a level crossing control method for automatic and autonomous running," *2023 IEEJ National Convention*, 2023 (in Japanese).

Authors

Takayasu KITANO, Ph.D.
Senior Researcher, Train Control Systems Laboratory, Signalling and Operation Systems Technology Division
Research Areas: Communication-based Train Control System, Wireless Communication System

Hiroyuki FUJITA
Senior Chief Researcher, Head of Train Control Systems Laboratory, Signalling and Operation Systems Technology Division
Research Areas: Signalling systems, Automatic Train Protection, Reliability

Kazumasa KUMAZAWA
Senior Researcher, Transport Operation Systems Laboratory, Signalling and Operation Systems Technology Division
Research Areas: Running Time and Headway Calculation

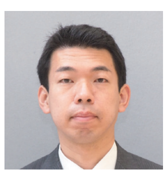

Yoichi SUGIYAMA
Assistant Senior Researcher, Train Control Systems Laboratory, Signalling and Operation Systems Technology Division
Research Areas: Radio Train Control System

Verification of Combined Maintenance Effect by Tamping and Grinding and Application to Decision Support System for Conventional Lines

Mami MATSUMOTO
Track Geometry & Maintenance Laboratory, Track Technology Division

Kenya MORI
Track Geometry & Maintenance Laboratory, Track Technology Division (Former)

In the case of ballasted tracks, track irregularity and rail surface roughness gradually increase due to repeated loadings from passing trains. Ballast tamping and rail grinding are carried out to repair these problems as part of general maintenance work. This paper verifies the effect of combining these two types of track maintenance to reduce the speed of track deterioration. Furthermore, extending the previously developed combined maintenance planning system, the authors simulate maintenance plans considering the effect of combined maintenance.

Key words: *track maintenance, rail grinding, track irregularity progression, axle-box acceleration, combined maintenance planning system*

1. Introduction

Although ballasted track is relatively simple to lay and economically advantageous, the shape of the track and the materials used in the track gradually deteriorate due to repeated train passages. Among these deteriorations, those that have a significant impact on the ride comfort and running safety of the train are the minute roughness of the rail surface and the gradual increase in irregularity of the track in relation to its normal position due to deformation of the ballast layer caused by repeated train loads. Accordingly, for the former, railway operators generally use a rail grinding machine to repair the rail surface, while for the latter, a tamping machine is utilized in ballast tamping (track irregularity maintenance). Efficient planning and execution of these maintenance activities is an important issue for railway operators to reduce costs, as the costs associated with rail grinding and track irregularity maintenance are high.

In previous studies on the efficiency of track maintenance planning, a model was designed to estimate future track irregularity from track irregularity data and generate an optimal track irregularity maintenance plan. Based on this model, a system was developed to generate an optimal operation plan for the tamping machine and the rail grinding machine [1, 2]. Moreover, it is known that when track irregularity maintenance and rail grinding are combined and carried out at the same time (hereinafter referred to as “combined maintenance”), the progression of longitudinal level irregularity is suppressed compared to that before combined maintenance [3]. And a system has been devised to create a combined maintenance plan for tamping machines and rail grinding machines [3]. This system considers that the interval between periods of maintenance for track irregularities can be extended by performing combined maintenance, thereby reducing frequency of track maintenance. However, these studies were conducted on Shinkansen lines, and the effects of combined maintenance were not clarified for conventional lines with different annual tonnage, and maintenance intervals for tamping and rail grinding.

Accordingly, in this study, we carried out trial runs for the application of combined maintenance on conventional lines and verified the effect of suppressing the progression of longitudinal level irregularity. Moreover, for the existing combined maintenance planning system, we investigated the input parameters suitable for conventional lines, and devised methods for the simple creation of combined maintenance plans for conventional lines. Additionally, we discuss the results of a simulation of the combined maintenance plan for conventional lines using this system [4].

2. Verification of efficacy of combined maintenance for conventional lines

2.1 Selection of trial section

A series of trial runs were conducted on multiple sections of conventional lines to assess the efficacy of combined maintenance in suppressing the progression of longitudinal level irregularities. The occurrence of rail surface roughness and the impact of rail grinding on the improvement of rail surface roughness were also investigated. Note that, the rail surface roughness and axle-box acceleration data presented in this paper have been subjected to a bandpass filter process (hereinafter referred to as “BPF processed”) in the wavelength band of corrugation formation of the rail surface roughness caused by inside track wear occurring in the target line section.

For selection of trial sections, we referred to the candidate lot selection model [3] for combined maintenance as utilized in Shinkansen lines, and set the conditions suitable for conventional lines. Table 1 shows the conditions for selecting candidate lots in combined maintenance of conventional lines. The lots meeting all the three conditions are selected as candidate lots for combined maintenance. The concept of each condition is described as follows.

In condition No. 1 we identify the lots where the longitudinal level irregularity is expected to exceed the threshold value such as the maintenance target value by the end of the year, since it is difficult to realize the longitudinal level irregularity improvement effect even if tamping is performed on a lot with a minor longitudinal level irregularity. In condition No. 2, using the indicator of axle-box acceleration, which has a high correlation with track surface roughness and can be continuously measured in the car, we select the lots where the effect of rail grinding on roughness improvement is most likely to be realized. In condition No. 3, adequate improvement in track irregularity cannot be achieved even when combined maintenance is performed on lots where the ballast condition is poor. Consequently, we use the indicator of longitudinal level irregularity (5-m chord), which is considered to be a more suitable means of evaluating the condition of the ballast than previous studies [5].

Note that the thresholds for longitudinal level irregularity (10-m chord) (condition No. 1) and axle-box acceleration (condition No. 2) were used as a guideline for the introduction of tamping and rail grinding in the trial sections. Accordingly, the threshold values are higher than those used in the Shinkansen.

Table 2 shows the trial sections selected by additionally considering the operational condition of tamping and rail grinding, from the candidate lots for combined maintenance selected by applying the aforementioned conditions. Note that, all the sections were 25-m fixed-length rail sections, and tamping was performed prior to rail grinding. All the trial sections were selected from the same single-track section, with the exception of section C, which was a double-track section causing the annual passing tonnage to be different. The "maintenance length" in the table presents the maintenance length for combined maintenance. "Combined maintenance interval" denotes the number of days between tamping and rail grinding.

2.2 Investigation of the effect of repairing rail surface roughness using rail grinding

To confirm the efficacy of rail surface roughness repair by rail grinding, we measured the rail surface roughness on trial sections A-C shown in Table 2 before and after rail grinding. Figure 1 shows the rail surface roughness before and after rail grinding on the inside track of the curved sections A and C. As observed in Fig. 1 (a), for section A, the amplitude of the rail surface roughness barely decreased after grinding, which may be due to the inadequate number of passages. The number of passages refers to the number of times a rail grinding car passes through while grinding with whetstone in one maintenance intervention. In contrast, for section C as shown in Fig. 1 (b), the amplitude of the rail surface roughness after rail grinding was significantly reduced compared to that before rail grinding, indicating that the rail surface roughness improved due to an adequate number of passages with the rail grinding car.

Table 1 Conditions for selection of candidate lots in combined maintenance

No	Condition	Evaluation index	Limit	
			Conventional line	Shinkansen
1	Irregularity condition	Standard deviation of longitudinal level irregularity (10-m chord) (mm)	4.3 or more	1.1 or more
2	Rail surface condition	Standard deviation of axle-box acceleration (m/s^2)	25 or more	0.7 or more
3	Ballast condition	Standard deviation of longitudinal level irregularity (5-m chord) (mm)	4.0 or less	1.5 or less
		Deference of standard deviation of longitudinal level irregularity by axis (5-m chord) (mm)	0.6 or less	-
		Maximum value of longitudinal level irregularity (5-m chord) (mm)	7.0 or less	4.0 or less

Table 2 Test section of combination maintenance

Section	Track	Passing tonnage(mil. ton/year)	Maintenance length (m)	Radius (m)	Maintenance interval (day)
A	Single	6.3	880	300	113
B	Single	6.3	225	400	124
C	Double	8.4	134	500	92
D	Single	6.3	400	300	93

Accordingly, for section C, the relationship between the number of passages and rail surface roughness was investigated when rail grinding was conducted. The amplitude of the rail surface roughness was evaluated using the average rail surface roughness, which was calculated by multiplying the total amplitude of the rail surface roughness waveform assuming an ideal sine wave, by $2\sqrt{2}$ times the standard deviation of the rail surface roughness waveform in a certain section [6]. Note that, to exclude the influence of large values that occur locally due to rail joints, such as the section surrounded by the red dashed line shown in Fig. 1 (a), the average rail surface roughness was calculated with a 25-m lot, excluding 1 m before and after the joints. Furthermore, rail grinding in these track sections was carried out using a grinding car equipped with eight grinding heads manufactured by SPENO.

Figure 2 shows the relationship between the number of passes and the average rail surface roughness when rail grinding was done on the C section lot No. 1 - No. 3 shown in Fig. 1 (b). As observed in this Fig. 2, the average rail surface roughness in all lots in this section was approximately 0.10-0.15 mm before grinding. However, the average rail surface roughness was significantly reduced in the 7th-12th grinding passage, with the average rail surface roughness after the 12th passage remaining largely unchanged. Accordingly, for section C, 12 passages were likely to be adequate for repairing rail surface roughness.

2.3 Verification of suppression effect regarding longitudinal level irregularity progression

Figures 3 and 4 show the speed of longitudinal level irregularity progression and the standard deviation for the 25-m lots before and after the combined maintenance in the test sections A-D. As observed in Fig. 3, the longitudinal level irregularity progression after maintenance is smaller than that before maintenance in most lots. Moreover, irrespective of the longitudinal level irregularity progression before maintenance, the longitudinal level irregularity after maintenance is within a certain value. Accordingly, it is likely that the larger the track irregularity before maintenance, the greater the difference in longitudinal level irregularity progression before and after maintenance, and the greater the suppression effect regarding longitudinal level irregularity progression.

Figure 4 shows the relationship between the difference in the

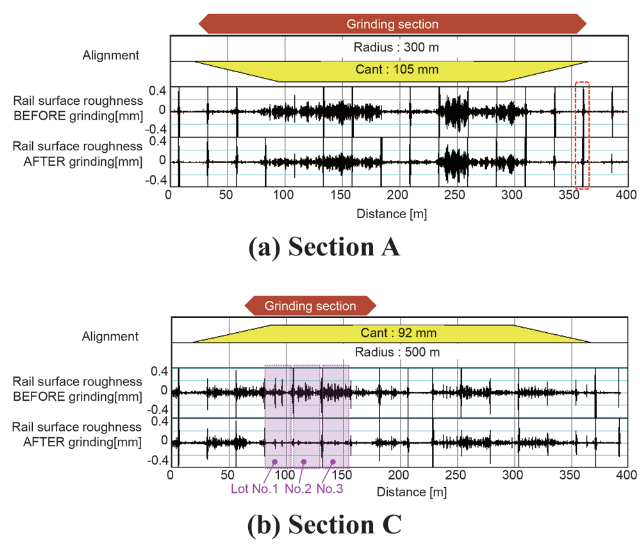

Fig. 1 Rail surface roughness

average rail surface roughness before and after rail grinding (average rail surface roughness improvement) in the inside track of the trial sections A-C and the difference in longitudinal level irregularity progression before and after maintenance. The observed trend is that the greater the average rail surface roughness improvement due to rail grinding, the greater the combined maintenance effect on longitudinal level irregularity progression. This is because the difference in longitudinal level irregularity progression represents the suppression effect on longitudinal level irregularity progression due to combined maintenance. Moreover, in the same figure, it is observed that at lots where the amount of improvement in rail surface roughness is small due to an insufficient number of passes, such as in section A shown in Fig. 1 (a), the combined maintenance effect also tends to be small.

Figure 5 shows the change in standard deviation of the longitudinal level irregularity and the axle-box acceleration in a 25-m lot within section D. Although the rail surface roughness was not directly measured in section D, it is likely that a certain amount of rail surface roughness was repaired by rail grinding, because after the rail grinding the axle-box acceleration was reduced by about half of that before grinding. As observed in the same Fig., when only tamping was performed, there was no significant change in longitudinal level irregularity progression before and after maintenance. However, when tamping and rail grinding were combined and performed concurrently, the longitudinal level irregularity progression was significantly reduced after maintenance compared to that before maintenance. Furthermore, in this example, it is observed that the suppression effect on longitudinal level irregularity progression due to combined maintenance persists for at least three years.

The aforementioned results indicate that, as was observed in the Shinkansen lines, the longitudinal level irregularity progression before combined maintenance is also significant on conventional lines. Furthermore, it can be seen that the greater the amount of rail surface roughness improvement due to rail grinding, the more the combined maintenance effect is realized.

3. Model for estimation of effect of combined maintenance

3.1 Relationship between rail surface roughness and axle-box acceleration

The utilization of axle-box acceleration, which can be measured continuously on trains, is known to be an effective method for assessing rail surface roughness [6]. Accordingly, in order to construct a model for estimating the combined maintenance effect in the target line section of this analysis, we ascertained the relationship between axle-box acceleration and rail surface roughness.

For sections A-C, Fig. 6 shows the relationship between the average rail surface roughness obtained using the rail surface roughness continuous measuring equipment and the standard deviation of axle-box acceleration for the 25-m lot, as measured at the front axle of the bogie in the track inspection car. Figure 7 shows a robust correlation between the rail surface roughness and the axle-box acceleration (standard deviation), with a correlation coefficient of 0.963. Note that, the running speed of the track inspection car in the section analyzed in this study was distributed in the range of 60-65 km/h. In a previous study [6], the axle-box acceleration data at the front axle of the bogie were BPF processed according to the wavelength band of rail corrugation formation caused by track wear. The

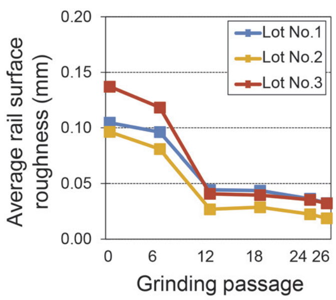

Fig. 2 Number of passes and average rail surface roughness

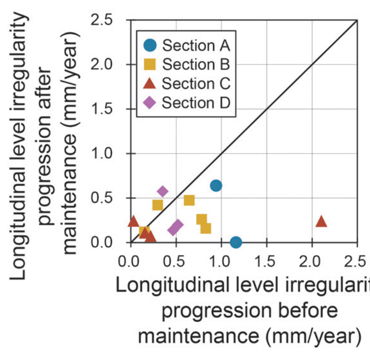

Fig. 3 Irregularity progression before and after combination maintenance

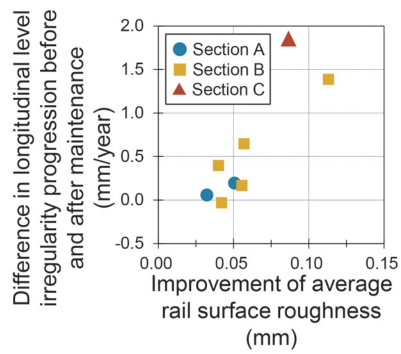

Fig. 4 Average rail surface roughness improvement

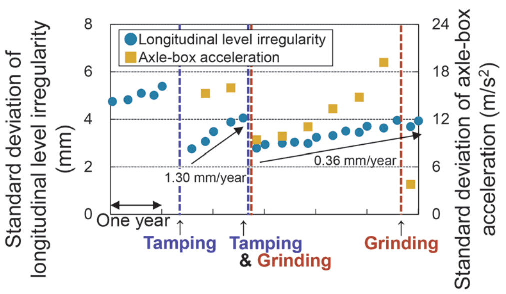

Fig. 5 Change of longitudinal level irregularity and axle-box acceleration

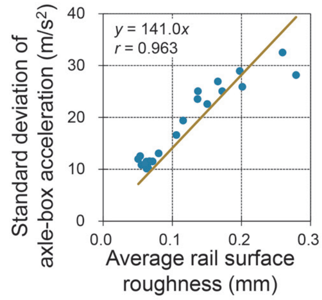

Fig. 6 Rail surface roughness and axle-box acceleration

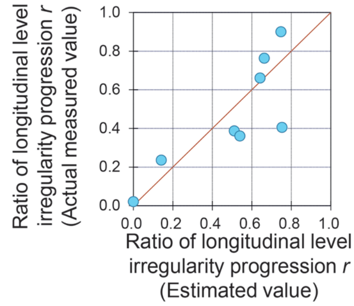

Fig. 7 Estimation Accuracy of irregularity progression ratio

data were collected under normal running speeds (approximately 40-70 km/h) depending on the curve radius. The data indicate that the impact of running speed on rail surface roughness is small, making it suitable for evaluating rail surface roughness. Based on these observations, using the relationship shown in Fig. 6, the rail surface roughness can likely be estimated using the axle-box acceleration for the section excluding the low-speed running sections such as stations.

3.2 Model for estimation of effects of combined maintenance on conventional lines

For the Shinkansen lines, a model for estimating the combined maintenance effect has been proposed using the improvement in axle-box acceleration due to rail grinding, and the order and interval of maintenance combining tamping and rail grinding as explanatory variables [3]. However, since the amount of rail grinding required on conventional lines is much smaller than that required on the Shinkansen lines, sufficient data on maintenance sequences and intervals could not be collected in this verification. Accordingly, using the data collected in this verification, we proposed an estimation model for the effect of combined maintenance on conventional lines without using maintenance order and interval as explanatory variables.

Based on the results of the previous section, the suppression effect of combined maintenance on longitudinal level irregularity progression, was likely affected by the longitudinal level irregularity progression before maintenance $\Delta\sigma_b$ mm/year as shown in Fig. 3, and the amount of improvement in rail surface roughness due to rail grinding as shown in Fig. 4. In addition, since according to section 3.1, there is a strong positive correlation between rail surface roughness and axle-box acceleration, it is likely that there is a strong correlation between the amount of improvement in rail surface roughness and the amount of improvement in axle-box acceleration α_{imp} m/s^2, which are the respective differences for these indicators before and after the maintenance. Based on these relationships, an estimation model of the longitudinal level irregularity progression ratio r (the ratio of longitudinal level irregularity progression after maintenance to longitudinal level irregularity progression before maintenance) for combined maintenance was constructed as shown in equation (1), using regression analysis with $\Delta\sigma_b$ and α_{imp} for sections A-D as parameters. The same equation shows that the greater the longitudinal level irregularity progression before maintenance and the greater the improvement in the axle-box acceleration resulting from rail grinding, the smaller the longitudinal level irregularity progression ratio r, and the greater the combined maintenance effect.

$$r = 1 - 0.0205 \times \alpha_{imp} - \Delta\sigma_b \ (\text{where} 0 \leq r \leq 1) \quad (1)$$

The coefficient of determination of this equation was 0.945, indicating that the regression equation exhibited high goodness of fit and high explanatory power as an estimation model of the longitudinal level irregularity progression ratio r.

Figure 7 shows the relationship between the estimated value of the longitudinal level irregularity progression ratio r and the measured value. In the same figure, it is observed that the estimated value and the measured value exhibited a close correlation, with an RMSE (root mean square error) of the difference between the two values of 0.174. Although equation (1) above is an estimation equation for the purpose of application to the target line section in this analysis, it is likely that an estimation model of the longitudinal level irregularity progression ratio due to combined maintenance can be constructed for another line section using the method described here.

4. Combined maintenance planning system

4.1 System configuration

By coupling the following three systems, the combined maintenance planning system enables easy formulation of an operation plan for the tamping machine and the rail grinding machine in combined maintenance. The first system is the Railway Condition Analyzer (RCA) [7], which evaluates track conditions using track inspection data. The second system is the tamping machine (Multiple tie Tamper) Scheduler (MTS) [1], which creates a tamping schedule. The third system is the Rail Grinding Scheduler (RGS) [2], which creates operating plans for the rail grinding car.

Figure 8 shows the configuration of the combined maintenance planning system. First, using RCA, we select "candidate lots for combined maintenance" where combined maintenance is expected to be effective. Note that, as shown in Table 1, the parameters used are different from those for Shinkansen lines. Next, MTS is utilized to generate the tamping schedule with longitudinal level irregularity serving as the indicator. At this point, the conditions are set such that tamping is conducted at the combined maintenance candidate lots within the designated plan period. Finally, using RGS, the rail grinding car operation plan is created with the input of axle-box acceleration as the indicator. The plan is created such that, at the candidate lots for combined maintenance, the rail grinding will be conducted within a certain period of time before and after the tamping period. This approach is expected to result in the maintenance of track irregularities by the tamping machine, the repair of rail surface roughness by the rail grinding machine, and the suppression of longitudi-

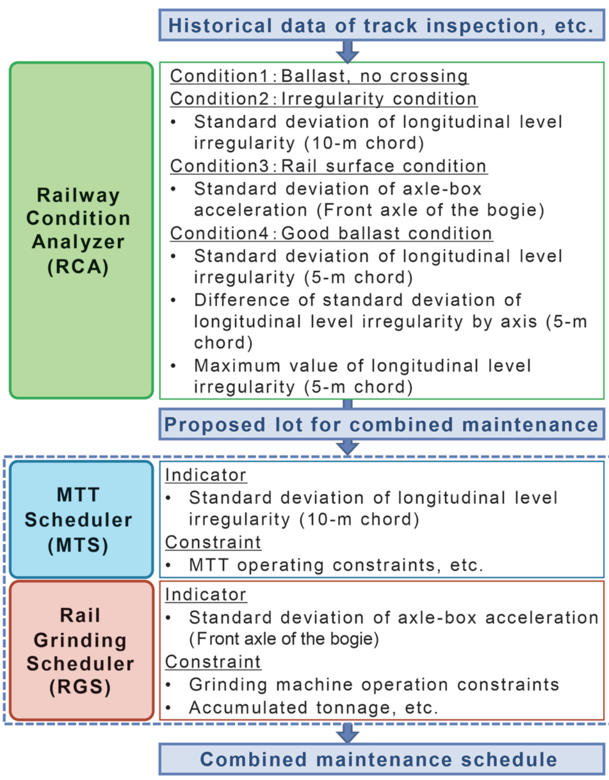

Fig. 8 Combined maintenance planning system

nal level irregularities due to the combined maintenance effect.

4.2 Combined maintenance planning simulation using the system

4.2.1 Simulation condition

A simulation was conducted to assess the operational plan for the tamping machine and rail grinding machine, as well as the estimation of track conditions in consideration of combined maintenance over a three-year period. To achieve this, we used the combined maintenance candidate conditions (Table 1) and integrated the results of the estimation of combined maintenance effects described in section 3 into the maintenance planning system. The following are the five conditions for the simulation.

A) Target line sections and number of lots planned

The target was one control area in the same line section as the trial section shown in Table 2. This area was a single-track section, and one tamping machine and one rail grinding machine were assumed. The length of a lot, which is the minimum distance unit at the time of planning, was set at 100 m, with the total number of lots in the target area being 1,270 (equivalent to 127 km). Of these, 1,000 lots were used in the planning, excluding 270 lots, including crossings, and non-ballast sections, where rail surface roughness evaluation using axle-box acceleration was inappropriate because of low-speed driving.

B) Track inspection and axle-box acceleration data

We used the latest three years of data on track inspection and axle-box acceleration. For the target sections the data were measured four times using track inspection cars, among which, the axle-box acceleration at the front axle of the bogie was measured two times. Excluding the data where appropriate axle-box acceleration data could not be collected, the data utilized comprised track inspection data from 11 track inspection runs, and axle-box acceleration data from four track inspection runs.

C) Plan of maintained length of track and number of maintenance days

The planned length of track to be maintained per day and the number of days of maintenance planned annually were set to be close to the most recent results of tamping and rail grinding. The planned tamping length was set at 46.8 km/year and the planned rail grinding length was set at 14.4 km/year.

D) Amount of improvement due to rail grinding

As shown in Fig. 2, with adequate number of passes, the rail surface roughness after grinding is likely to be about 0.04 mm or less. Moreover, based on the equation of the relationship between the rail surface roughness and the axle-box acceleration shown in Fig. 6 (axle-box acceleration = 141.0 × rail surface roughness), it can be estimated that the rail surface roughness of 0.04 mm corresponds to an axle-box acceleration of 5.6 m/s^2. Accordingly, the axle-box acceleration after grinding was set to be uniform at 5.6 m/s^2 irrespective of the axle-box acceleration before grinding. Note that, the adequate number of passes for rail grinding should be determined from the rail surface roughness that can be estimated from the axle-box acceleration in Fig. 6 and the rail surface roughness measured before maintenance.

E) Maintenance designation of combined maintenance candidate lots

In the combined maintenance candidate lot selection conditions shown in Table 1, we set the condition No. 2 regarding the rail grinding target to be axle-box acceleration of 13 m/s^2 or more, to select even more candidate lots, and simulated a plan considering combined maintenance. Moreover, we simulated the case where the operating plan for the tamping machine and the rail grinding machine were created independently without considering the combined maintenance and its effects.

4.2.2 Simulation results

Figure 9 shows an example of the change in longitudinal level irregularity (standard deviations) of lots for which combined maintenance was planned. In the proposed system, the estimation model for the effect of combined maintenance derived in section 3.2, enables estimating the change reflecting the suppression effect of longitudinal level irregularity progression after combined maintenance.

Moreover, Table 3 shows the longitudinal irregularity progression and longitudinal irregularity at the beginning of the first year and at the end of each year in the maintenance plan obtained in this simulation, as the average value of all lots (1,000 lots) considered in the plan. The results of longitudinal level irregularity progression indicate that, when combined maintenance is considered, the suppression effect of longitudinal level irregularity progression is accumulated as the year passes, such that the longitudinal level irregularity progression at the end of each year decreases. In contrast, if combined maintenance is not considered, the longitudinal level irregularity progression at the end of each year will increase slightly. Next, the results of longitudinal level irregularity indicate that, considering combined maintenance it is only slightly smaller at the end of the first year, but as the second and third years pass, the longitudinal level irregularity becomes even smaller when combined maintenance is considered. That means, it results in improved track conditions. Note that, although as described above, the track irregularity progression increases slightly year by year when combined maintenance is not considered, the track irregularity is smaller than at the start of the project, since the effect of improving the track irregularity by maintenance exceeds this.

Based on the aforementioned results, it is likely that combining tamping machine and rail grinding machine in maintenance operations can suppress longitudinal level irregularity progression and improve the track conditions in the line section. Moreover, consid-

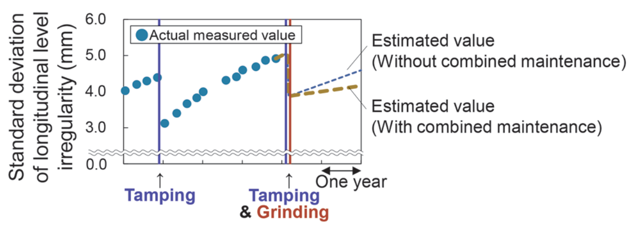

Fig. 9 Longitudinal level irregularity of combined maintenance lot

Table 3 Result of simulation

Indicator	Consideration of combined maintenance	Start of the 1st year	End of the 1st year	End of the 2nd year	End of the 3rd year
Longitudinal level irregularity progression (mm/year)	Included	0.310	0.294	0.286	0.276
	Not included		0.311	0.315	0.317
Longitudinal level irregularity (mm)	Included	2.86	2.81	2.78	2.75
	Not included		2.82	2.80	2.80

ering that, as the years passed, it became more advantageous to consider combined maintenance, it is likely that even if it is difficult to observe the effect of combined maintenance on conventional lines in the short term, the effect accumulates and produces a large effect by continuing it in the medium to long term.

5. Conclusion

The findings of this study are as follows.

(1) To verify the combined maintenance suppression effect on longitudinal level irregularity progression on conventional lines, we conducted trial runs of combined maintenance. The results demonstrated that the greater the amount of improvement in rail surface roughness due to rail grinding, and the greater the longitudinal level irregularity progression before maintenance, the greater the effect of suppression of longitudinal level irregularity progression due to combined maintenance.

(2) For application to conventional lines, we analyzed the candidate lot selection conditions and estimation models for the effects of combined maintenance. Based on the results, we investigated the input parameters suitable for conventional lines, for use in a combined maintenance planning system for creating an operating plan utilizing the tamping machine and the rail grinding machine. Moreover, we verified that the combined maintenance effect estimated by this model was close to the measured value.

(3) We performed a simulation with the combined maintenance planning system. The results indicate that planning tamping and rail grinding in combined maintenance can reduce longitudinal level irregularity and longitudinal level irregularity progression, i.e., it can lead to improved track conditions.

We plan to conduct further studies regarding the practical application of combined maintenance, such as follow-up surveys of the duration of the combined maintenance effect and analysis of the length of the appropriate combined maintenance plan.

References

[1] Miwa, M., "Mathematical Programming Model Analysis for the Optimal Track Maintenance Schedule," *Quarterly Report of RTRI*, Vol. 43, No. 3, pp. 131-136, 2002.

[2] Tanaka, H. et al., "Modeling the development of rail corrugation to schedule a more economical rail grinding," *In IME, Part F JRRT*, Vol. 234, No. 4, pp. 370-380, 2019.

[3] Matsumoto, M. et al., "Modeling an Optimal Track Maintenance Schedule in Consideration of Timing of Grinding and Tamping," *Quarterly Report of RTRI*, Vol. 58, No. 3, pp. 229-235, 2017.

[4] Matsumoto, M. et al., "Field Verification of the Combination of Rail Grinding and Ballast Tamping to Extend the Life of Track Conditions," *JSCE Infrastructure Maintenance Practices*, Vol. 2, pp. 109-117, 2023 (in Japanese).

[5] Kimura, H. et al., "Detection Methods for Finding Quickly Deteriorating Lots for Vertical Displacement Irregularities in Ballast Tracks," *JSCE 65th Annual Meeting*, pp. 277-280, 2009 (in Japanese).

[6] Tanaka, H. et al., "Application of axle-box acceleration to track condition monitoring for rail corrugation management," *Railway Condition Monitoring*, Birmingham, 1.b.2, 2016.

[7] Miwa, M., et al., "Optimal Track Maintenance Strategy Model Constructed by Considering Deterioration Level of Both Rail and Ballast, *RTRI Report*, Vol. 26, No. 2, pp. 13-18, 2012 (in Japanese).

Authors

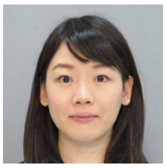

Mami MATSUMOTO
Assistant Senior Researcher, Track Geometry and Maintenance Laboratory, Track Technology Division
Research Areas: Track Geometry Management, Maintenance Support Systems

Kenya MORI
Assistant Senior Researcher, Track Geometry and Maintenance Laboratory, Track Technology Division (Former)
Research Areas: Track Geometry Management, Maintenance Support Systems

PAPER

Obstacle Detection Method using On-Train Forward-facing Cameras and Sensors

Ryo KAGEYAMA **Nozomi NAGAMINE**
Image Analysis Laboratory, Information and Communication Technology Division
Junki YOSHINO
Image Analysis Laboratory, Information and Communication Technology Division (Former)

Developing sensing technology that can reliably detect obstacles on the track well ahead of a train is essential for advancing on-train forward-facing track monitoring. Therefore, we developed a method for detecting obstacles in front of trains using cameras and sensors. In our method, obstacles such as people and vehicles are detected by combining multiple sensors within a detection area around the tracks. In this paper, we report on the results of a study of sensor configurations suitable for obstacle detection, the detail of our detection algorithm using cameras and LiDARs or a stereo camera, and the results of detection performance evaluation according to distance between train cab and object.

Key words: *train forward surveillance, obstacle detection, LiDAR, sensor fusion*

1. Introduction

It is important to reduce the risk of accidents involving obstacles on railway tracks in order to further improve railroad safety. If we can develop technology that uses a forward monitoring system to detect obstacles on the tracks, it will help maintain operational safety. Furthermore, this technology will be essential for future automatic operation of trains. In recent years, driver assistance systems using cameras and sensors have become popular in the automotive field to prevent accidents. The use of such sensing technology is considered effective as a driver assistance measure for railroads as well. However, trains run at higher speeds and over longer braking distances than automobiles.

Therefore, we are developing a method for detecting obstacles using cameras and sensors for operational support for railroads, with the aim of constructing a system capable of monitoring tracks for objects further away from the driving position than operational support systems in the automotive field [1].

This paper first describes the characteristics of each sensor and presents the results of a desk study of sensor configurations suitable for detecting different obstacles, based on the characteristics of obstacles on the tracks that should be detected. Secondly, detection algorithms using typical sensor configurations (camera + LiDAR and stereo camera) are developed, and the detection performance for obstacles at different distances is verified based on data obtained from tests and real trains.

2. Organization of requirements for obstacle detection

To organize the requirements for the obstacle detection method, we established environmental conditions and targets for detection. In addition, sensor configurations to meet the requirements were organized based on the characteristics of the sensors and the obstacles to be detected.

2.1 Target obstacles

In setting the target, we investigated past accident data in order to understand the situation of accidents in Japan involving contact with obstacles on or along railway tracks. Specifically, we analyzed a total of 8,343 cases of accident information stored in the “Railway Safety Database” [2] that resulted in serious accidents or delay due to contact between trains and obstacles during the past 20 years (2001-2021). The number of accidents by time of day is shown in Fig. 1. It has been confirmed that accidents can occur at any time of day and night when commercial trains are in operation. Figure 2 shows the number of accidents by obstacle. The most frequently occurring obstacle was a person, accounting for more than half of all accidents. This was followed by collisions with automobiles and motorcycles. Based on the above, in this study, we set the detection targets as three-dimensional objects such as people, vehicles, falling rocks, and fallen trees that enter the railway tracks, and aimed to detect these objects both in day and night time.

2.2 Characteristics of obstacles

Table 1 compares the characteristics of several sensors used mainly in ADAS for automobiles. A camera is a sensor that captures the light reflected from an object onto an imaging element, allowing the color and texture of the object to be captured in fine detail. Thus, it is possible to identify not only the presence or absence of an object from an image, but also its type. On the other hand, when illumination decreases at night, especially when there is no light source in the vicinity, performance deteriorates. A stereo camera consists of several cameras (generally two cameras) which can recreate the three-dimensional shape of an object based on the principle of triangulation, but its performance degrades at night when there is no light source in the vicinity, as is the case with cameras. LiDAR is a sensor that uses the reflection of a near-infrared laser with a wavelength of 900 to 1,500 nm to make measurements, and it is capable of identifying objects day or night as point cloud data, a set of laser points. The 3D ranging accuracy is higher than that of stereo cameras, and some models can detect distant objects. However, since laser points have only position and reflectance information, it is difficult to correctly identify the type of object unless there is a large difference in the reflectance of the object. In addition, since the laser is attenuated or reflected by glass, the performance is reduced when installed inside a car (depending on the thickness and material of the glass). Millimeter wave radar is a sensor that uses millimeter waves to measure reflected waves from objects. Depending on the millimeter wave bandwidth used, it can detect the presence or absence of distant objects with high resolution, but it is difficult to detect the size and shape of objects.

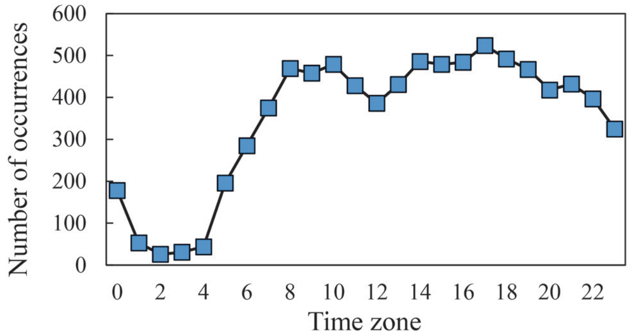

Fig. 1 Number of accidents by time of day

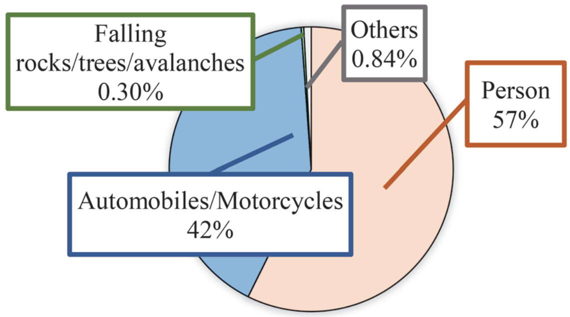

Fig. 2 Breakdown of obstacles

Table 1 Characteristics of typical sensors

	Recognition	3D shape detection	Application at night	Installation inside the car
Camera	○	×	△ Depends on lighting	○
Stereo camera	×	○	△ Depends on lighting	○
LiDAR	△ Depends on reflectivity	○	○	△ Depends on the type of glass
Millimeter wave radar	×	×	○	×

○ : Applicable △ : Depends on situation × : Not applicable

Table 2 Sensor configuration suitable to detect each obstacle

Obstacle	Time	Camera	Stereo camera	LiDAR
Person	Day	◎	○	Outside the car: ○ Inside the car: △ (Depends on type of glass)
	Night	△ (Depends on lighting)	△ (Depends on lighting)	Outside the car: ○ Inside the car: △ (Depends on type of glass)
Automobile	Day	◎	○	Outside the car: ○ Inside the car: △ (Depends on type of glass)
	Night	△ (Depends on lighting)	△ (Depends on lighting)	Outside the car: ○ Inside the car: △ (Depends on type of glass)
Fallen rocks and trees	Day	×	○	Outside the car: ○ Inside the car: △ (Depends on type of glass)
	Night	×	△ (Depends on lighting)	Outside the car: ○ Inside the car: △ (Depends on type of glass)

◎ : Identifiable ○ : Detectable △ : Depends on situation × : Not detectable

2.3 Characteristics of obstacles

The characteristics of the main in-line obstacles described in Section 2.1 are summarized. People can be identified by their limbs and heads, and automobiles can be identified by their bodies and tires. On the other hand, it is difficult to identify falling rocks and fallen trees from their appearance.

2.4 Characteristics of obstacles

Table 2 shows the results of the sensor configurations suitable for detection for each obstacle to be detected. For objects with well-defined shape characteristics, such as a person or a car, the camera can identify the category of object under sufficiently high illumination. On the other hand, since the recognition performance of the camera may deteriorate at night, it is desirable to use the camera in combination with LiDAR, which allows measurement in the dark. If the sensor cannot be installed outside the vehicle, it is preferable to use a stereo camera in an environment where the surrounding area can be illuminated to some extent, such as a station or a rail yard. Any three-dimensional objects, including falling rocks and fallen trees, are considered to be detectable by LiDAR or stereo camera.

3. Obstacle detection method

3.1 Overview of proposed method

We developed the obstacle detection method according to sensor configuration described in the previous chapter. Figure 3 shows the overall image of the proposed method. The detection area is set by predicting the track area from images, and obstacles within sight of the train are detected by combining information obtained from multiple sensors. In this study, a camera and LiDAR were used as cases where the sensor can be installed outside the vehicle, and a stereo camera was used as a case where the sensor location is restricted to inside the vehicle, and detection performance was evaluated. The details of each method are described in the following sections.

3.2 Setting of detection area

In order to detect obstacles around the track from the front of the train, it is necessary to recognize the track on which the train runs and to set up a detection area around the track. Therefore, we have developed a method for setting a detection area based on the prediction of the area between the left and right rails on which the train runs (track area) from the camera images. Figure 4 shows the method for setting detection areas. First, the track area is predicted by semantic segmentation (Step 1), a deep learning method that extracts specific areas in the image pixel by pixel. As pixels other than the track area may be output as the track area due to prediction errors, post-processing is performed to output only the area included in the specified range (red box in Fig. 4) at the lower edge of the image as the final detection area (Step. 2). An example of the output result is shown in Fig. 5. It was confirmed that the same accuracy was achieved in extracting the track area even for different scenes. We also confirmed that it is possible to expand the detection area to within the width of the clearance gauge based on the ratio between the gauge and the width of the clearance gauge.

3.3 Overview of proposed method

3.3.1 Detail of detection method

The process of obstacle detection by camera and LiDAR is shown in Fig. 6. The proposed method uses images and point cloud data obtained from multiple LiDARs to ensure detection performance regardless of illumination conditions, even in distant locations. First, we estimate the area where an object is likely to be located based on the information from both the images and the point cloud data. For the image, the position, size, existence probability, type, and recognition probability are predicted for each grid that divides the image evenly, using a deep learning model for object detection. On the other hand, after pre-processing the point cloud data to remove the ground data, the regions where the laser density exceeds a threshold value are extracted as candidate object point clouds. Secondly, using the information on the position of LiDAR installation as seen from the camera, a candidate object point cloud is projected onto the image, and an integration process is carried out to superimpose and compare the results with the detection results for each grid from the image. Since an object can be said to be almost certainly present on the grid where the center of a group of candidate object points is located, the probability that there is an object on that grid is set to 100% regardless of the value predicted from the image, and the size of the object is also set to the size of the group of candidate object points. When determining the object type, if the probability of determination predicted by deep learning is higher than a certain threshold value, the prediction result of deep learning is adopted. Otherwise, the object type is determined to be "unknown." When detection is performed with cameras alone, the recognition probability becomes low in low illumination, and objects may be missed. However, by overlaying a group of object candidate points on the image, it is possible to recognize the type of object up to a certain level of illumination. Also, even when the surroundings are completely dark, at least the presence or absence of an object can be ascertained.

3.3.2 Performance evaluation experiments of detection method

The performance evaluation experiment of the detection method using camera and LiDARs was carried out on a test road (NV/

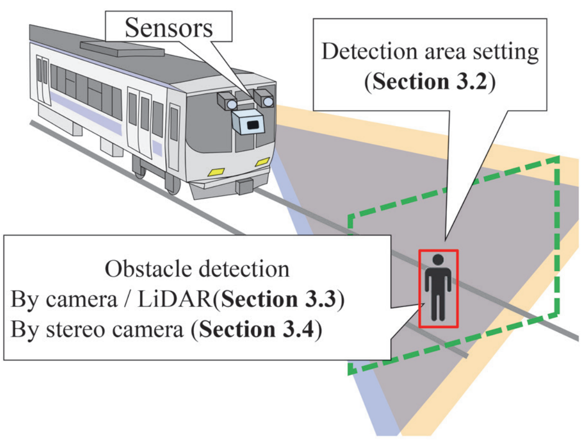

Fig. 3 Overview of obstacle detection

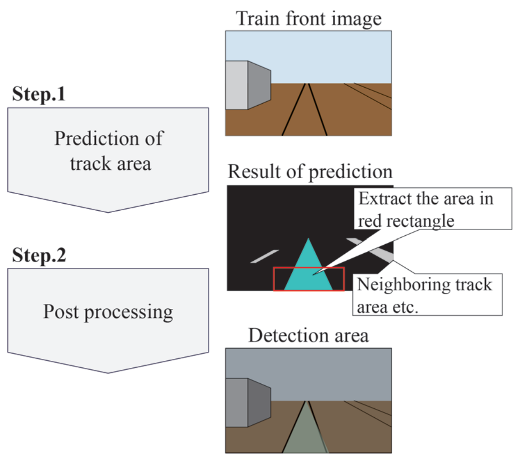

Fig. 4 Illustration of detection area setting process

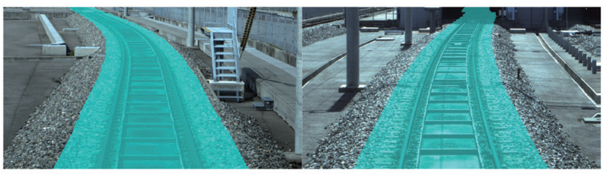

Fig. 5 Example of detection area setting result

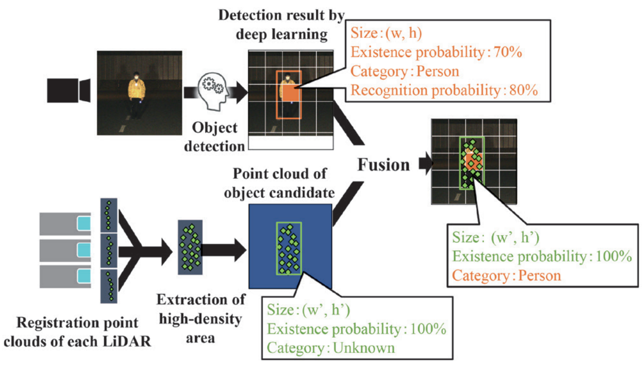

Fig. 6 The obstacle detection using camera and LiDAR

Table 3 Specifications of camera and LiDAR used in the experiment

Camera	Resolution	Horizontal 4,096 px Vertical 2,160 px
	Focal length of lens	35 mm
	Field of view	Horizontal 22.9° Vertical 12.1°
	Frame rate	Approximately 10 frame per second
LiDAR	Field of view	15°
	Number of laser points per 0.1 seconds	Approximately 24,000 points

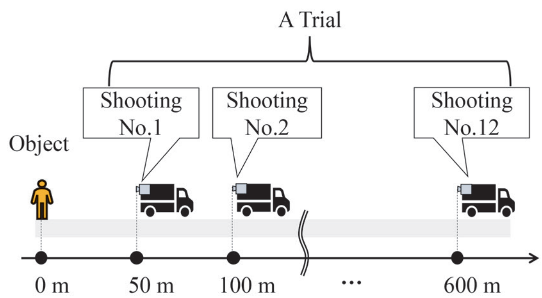

Fig. 7 Experimental procedure

Fig. 8 Examples of subjects

Versatile Test Road) at the Shirosato Test Center of the Japan Automobile Research Institute, which offers a long straight section of road (total length 1,500 m). A camera, nine LiDARs, and two LED front lights were installed on the back of a truck at a height of approximately 1.5 m from the ground to simulate the condition in which sensors are installed on a real vehicle. The camera and LiDAR specifications are shown in Table 3. The experiment procedure is shown in Fig. 7. A total of 12 fixed-point shooting sessions of 10 seconds (100 frames of images) were repeated for a stationary subject, every 50 m to a point 600 m away. A series of 12 shots for one subject is defined as one trial hereafter. The subjects were people in different clothing as shown in Fig. 8.

3.3.3 Detection Performance by distance from obstacle

As detection performance for each distance, the detection rate and recognition rate were calculated for 100 frames of images and corresponding point cloud data obtained at each shooting location for each trial. The detection rate is the percentage of frames in which the object is correctly predicted to be near the correct value of the position in the image where the object exists. The recognition rate is the percentage of frames in which the object can be predicted to be correctly located near the correct value of the position of the object in the image, and the type of the object matches the correct type.

Figure 9 shows an example of daytime and nighttime detection / recognition results for a person. At night, the green rectangle indicating "detection" disappears about 300 m away when only images are used, but when images and point clouds are used together, the rectangle is displayed at the same position as in daytime, indicating that detection is possible. In order to understand the relationship between the density of the point cloud data and the detection performance, Fig. 10 plots the detection rate for the detection of a person at night using the point cloud data obtained from 2 to 9 LiDAR units. Figure 10 shows that the detection rate of persons per distance tends to improve as the number of LiDARs increases. The detection rate at a distance of 500 m was estimated to be more than 95% when the lasers of 14 LiDARs were irradiated to the object (indicated by brown and red dotted lines in Fig. 10). The above results indicate that if the object is irradiated with lasers equivalent to the 14 LiDARs used in this test (about 25 points per square meter in 0.1 second), it is possible to detect a person 500 meters away with almost certainty. However, since this verification test was conducted using data obtained when both the sensor and the subject were stationary, further verification of the detection performance while the train is running is needed.

3.4 Obstacle detection method using stereo camera

3.4.1 Detail of detection method

Assuming that the sensor is installed in a limited space inside the vehicle, we have developed an obstacle detection method using a stereo camera. In the proposed method, a depth image is obtained from the images of the left and right cameras, mapping the depth from the camera to each pixel. The ground can be represented by a mathematical expression as a certain plane in a three-dimensional coordinate system with the camera position as the origin, and the approximate position of the ground and the height of an object from the ground in the depth image can be estimated by giving the installation height of the camera and the angle of elevation. As shown in Fig. 11, this allows us to extract three-dimensional objects in the image by extracting only those areas in the depth image that are a certain height above relative to the ground. Of these, the three-dimensional objects that exist within the detection area set by the method described in section 4.1 are extracted as obstacles on the track.

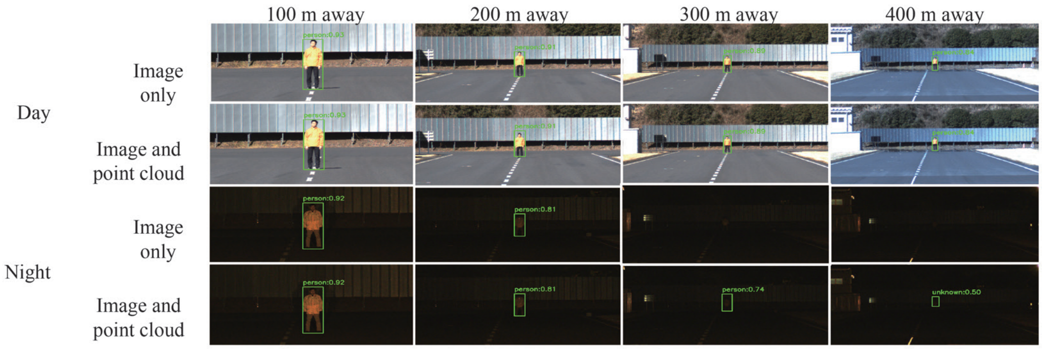

Fig. 9 Detection results for a person

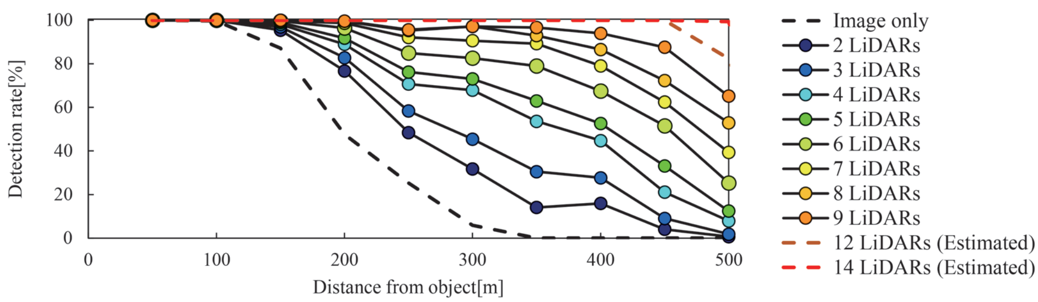

Fig. 10 Detection rate of person by distance at nighttime.

3.4.2 Performance evaluation experiment of detection method

An evaluation test of the detection performance of the developed method was carried out at a rail yard. A camera was installed on the rear of the vehicle. The camera specifications are shown in Table 4. The train was moved away from the obstacle on the track and the images were taken. As shown in Fig. 12, workers and toolboxes were selected as subjects.

3.4.3 Detection Performance by distance from obstacle

To evaluate the detection performance at each distance from the image, the presence or absence of detection was counted for each frame, and the detection rate was tabulated for each 10 m distance. The distance to the object per frame was estimated by the correspondence between the pixel-by-pixel movement in the track plane of the forward image and the total length of the train running path during the test.

Examples of detection results for a worker and a toolbox are shown in Fig. 13. It was confirmed that the developed method can detect objects with a certain height above the ground as three-dimensional objects in the depth image. Figure 14 shows the detection rate (average of 20 daytime trials and 22 nighttime trials) for a person standing on a track in the daytime at different distances from the subject. For daytime, the detection rate was found to be more than 90% when the distance from the subject was within 90 m. Assuming that the speed of a train running in a rail yard is 40 km/h, the deceleration of a train is 4 km/h/s, and the time required for the driver to notice obstacles and apply the brakes (reaction time) is 1 second, the distance from the time the obstacles is detected to the time the train stops is estimated to be about 90 m. Therefore, if the train is running at 40 km/h or less and there is sufficient illumination, the proposed method can be used to detect the obstacles.

4. Conclusions

In this study, we examined sensor configurations for detecting obstacles on the tracks using on-train forward-facing cameras and sensors to assist the drivers, developed a detection method, and

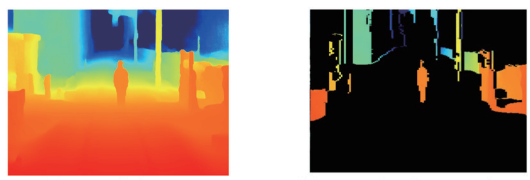

(a) Depth image

(b) Result of extraction of three-dimensional objects

Fig. 11 The example of the result of extracting three-dimensional objects from a depth image

Table 4 The specifications of stereo camera

Resolution	Horizontal 1,024px×Vertical 768px
Focal length of lens	25 mm
Frame rate	10 frame per second
Base line length	25 cm

Fig. 12 Examples of subjects

verified its performance.

The past data on collisions between trains and obstacles on tracks were used to develop the method, with the goal of “detecting three-dimensional objects on the tracks, both day and night.” Next, the characteristics of typical cameras and sensors used for obstacle detection were summarized, and a sensor configuration suitable for detecting the target obstacle was studied.

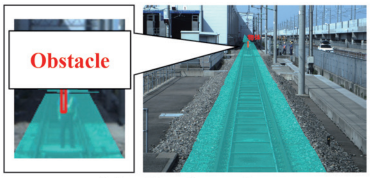

(a) Track worker

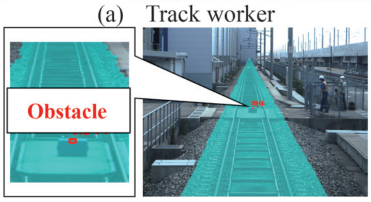

(b) Toolbox

Fig. 13 Example of detection results

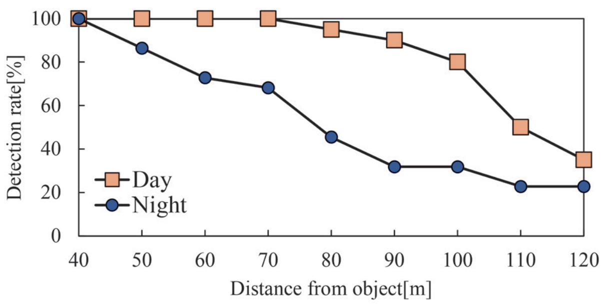

Fig. 14 Detection rate per distance to a person

A detection method using the studied sensor configurations (camera, LiDAR, and stereo camera) was developed and its performance was evaluated. We confirmed that the obstacle detection method using cameras and LiDARs can detect a person at a distance of 400 m with a detection rate of more than 90%, day or night, when up to nine LiDARs are used in combination. The relationship between the number of LiDARs used and detection performance showed that 15 LiDARs can detect obstacles 500 m away with a detection rate of more than 95%. We also developed a detection method using a stereo camera based on the assumption that the sensor is installed only inside the vehicle, and evaluated its performance by installing it on a real vehicle at a rail yard.

In the future, as sensor technology develops, we will work to further improve the detection distance by applying more advanced cameras and LiDAR to the developed method. In addition, we will examine sensor configurations and develop detection methods for other abnormal events which are not the subject of this paper because there are no cases directly related to accidents that affected train operations, such as fires along train tracks and objects falling from overhead wires.

References

[1] Kageyama, R. and Nagamine, N., Study on Sensor Fusion Method for Train Forward Surveillance, *J-RAIL2022*, S4-3-4, 2022.

[2] Railway Technology Promotion Center in Railway Technical Research Institute, Railway Safety Database (Checked on 2023/2/3).

Authors

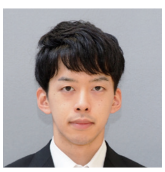

Ryo KAGEYAMA
Researcher, Image Analysis Laboratory, Information and Communication Technology Division
Research Areas: Image Processing, Point Cloud Processing

Nozomi NAGAMINE, Ph.D.
Senior Chief Researcher, Head of Image Analysis Laboratory, Information and Communication Technology Division
Research Areas: Computer Vision, Image Processing, Signalling Systems

Junki YOSHINO
Researcher, Image analysis Laboratory, Information and Communication Technology Division (Former)
Research Areas: Image Processing

PAPER

Elucidation of Noise Near the Bogie Using Sound Source Visualization Method

Minoru SASAKURA
Traction Systems Laboratory, Vehicle Technology Division

There are many sources of railway vehicle noise generated by equipment such as gear devices installed in the narrow space of a bogie frame under the floor of a vehicle. Therefore, it is difficult to separate the sound sources onboard a vehicle with a sound level meter, and up to now there no method has been developed for separating the sound sources. As a method to solve this problem, we are working on applying a sound source visualization method to the noise measurement of railway driving devices. The 4-channel beamforming method (BF method) and the envelope intensity method (EI method) are used as sound visualization methods, and the test results are compared. This paper reports on the results of noise measurement on a driving device using a sound source visualization method in bench-scale testing, and the results of a study to improve accuracy. We confirmed that the beamforming method has excellent imaging stability for transient sounds, and that image processing using multiple small microphone arrays improves the imaging accuracy of the BF method.

Key words: *driving device, noise analysis, sound source visualization, beamforming method.*

1. Introduction

The main noise sources of an electric vehicle driving device are the traction motor, and the gearbox, and there are several sound sources in the confined space inside the bogie.

Conventional noise measurements use sound level meters, but it is sometimes difficult to separate individual sound sources. Therefore, it is difficult to pinpoint exactly where noise is coming from. This makes it difficult to take measures to reduce noise and find out the cause of failures. In recent years, several noise visualization techniques have been developed that use multiple microphones and small cameras to visualize the location and intensity of noise sources and the flow of acoustic energy. These techniques do not require a special measurement environment such as an anechoic chamber. This makes it possible to identify noise sources with high accuracy in vehicle factories and outdoor environments.

By using these techniques, it becomes possible to quickly recognize and specify the location of noise generation visually. This makes it possible to quickly determine equipment failures and confirm the noise reduction effects of developed products.

This study focuses on a 4-channel beamforming method (BF method), which is smaller than conventional sound source visualization equipment, and describes the effectiveness of the method and the elucidation of the sound sources of driving devices.

2. Noise environment of driving device

A drive unit is attached to a bogie frame under the vehicle floor. The traction motor, the coupling, and the gearbox are located within a limited space of approximately 1 to 2 meters around it, and noise is generated by each of these devices (Fig. 1).

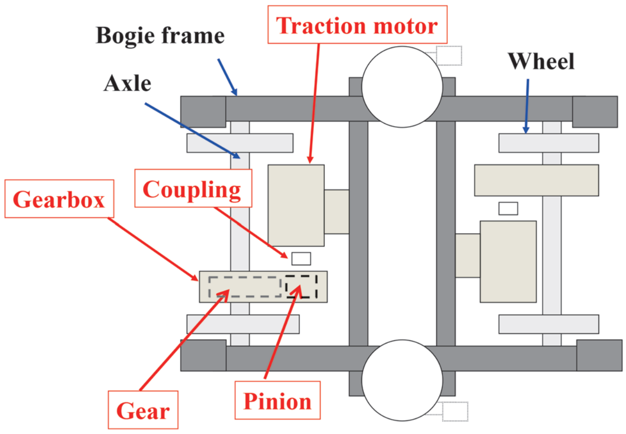

Fig. 1 Driving device of motor car

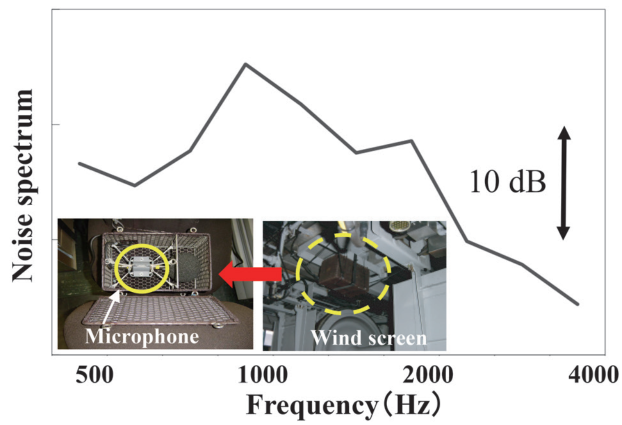

Fig. 2 Frequency band of underfloor noise

Furthermore, there is also rolling noise generated by the wheels and rails. When the vehicle is running, high-frequency noise is generated under the floor, and the frequency band is approximately 300 Hz to 4 kHz (Fig. 2). In particular, frequencies around 1 kHz overlap with the main frequency band of rolling noise, making it difficult to accurately locate the sound source. In order to advance noise reduction measures for driving devices, it is essential to understand individual noise sources and analyze their factors. Therefore, it is necessary to establish an analysis technology that can separate sound sources.

3. Sound source visualization method and measurement principle

The noise generated by the driving device may be caused by the meshing force of gears, but the vibration source and the noise generating part are not necessarily located at the same place, and the noise can be generated by parts far away from the vibration source due to solid-borne vibration. For this reason, it may be difficult to elucidate the phenomenon.

In this study, we investigated the applicability of sound source visualization methods, focusing on the BF method, and also carried out correlation analysis using vibration accelerometers and sound level meters (Fig. 3).

Table 1 shows a comparison of sound source visualization methods. The BF method uses the principle of exploring the spatial distribution of sound sources by using the difference in arrival time of incident waves due to the differences in the position of each microphone to provide directivity (delay time estimation method) (Fig. 4). This principle makes it possible to identify sound sources coming from a specific direction. The range of effectiveness of the BF method covers a relatively wide frequency range, approximately 500 Hz to 8 kHz. This almost covers the noise frequency band of the driving device shown in Fig. 2, and the BF method is considered to be highly applicable.

On the other hand, an envelope intensity method (EI method) uses the same small microphone array as the BF method, but the center of the sound source is represented as a moving trajectory of a point, instead of a two-dimensional map as in the BF method. The time resolution of the BF method is ms, while the time resolution of the EI method is μs. Therefore, it is possible to visualize the noise even in transient sounds where the value and the location of the noise changes rapidly. The EI method is a method for calculating the instantaneous amplitude and instantaneous phase by replacing the envelope of an acoustic signal (time waveform) with a complex time signal using the Hilbert transformation.

Data processing in the conventional BF method corresponds to A (Fig. 5). There are methods such as arranging a large number of microphones at regular intervals in a grid pattern, or arranging them in a circle at irregular intervals, but depending on the required spatial resolution and the target frequency band, a large number of microphones may be required. For this reason, the scale of the configured microphone array also increases. In addition to A in Fig. 5, this device uses the minimum dispersion method shown in B, making it possible to suppress noise with a small number of microphones, thus reducing the size of the system [1]. The system uses a device called a microphone array, in which four microphones are arranged in a regular tetrahedral structure, as shown in Fig. 6, and a camera is attached to the center to reduce the overall size. By superimposing the camera image and the position coordinates of the sound source, the

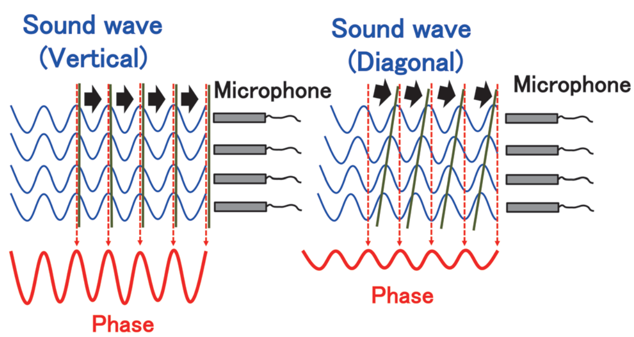

Fig. 4 Principle of BF method (Delay time estimation method)

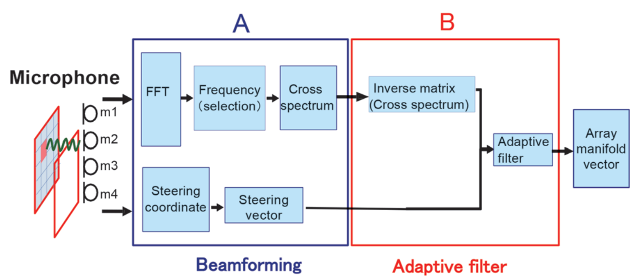

Fig. 5 Data processing using the BF method

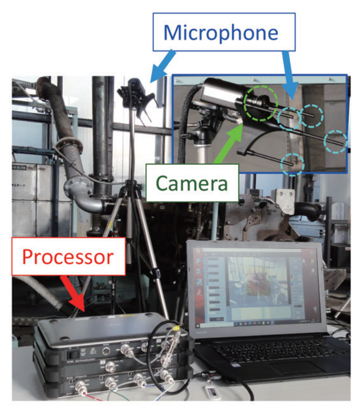

Fig. 6 BF small microphone array measurement device

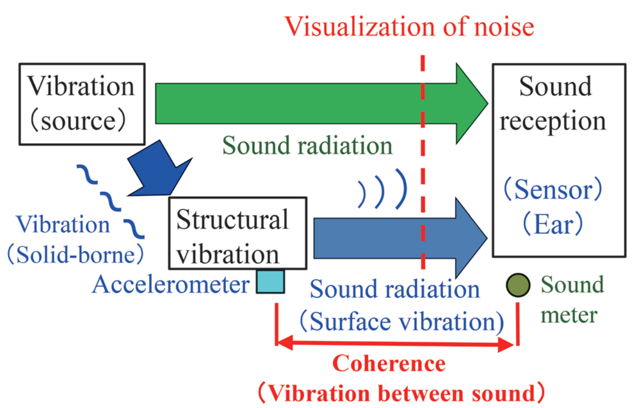

Fig. 3 Relationship between vibration and noise paths and sound source visualization

Table 1 Comparison of sound source visualization methods

Measurement method	Sensor	Processing principle	Sound source	Advantage	Disadvantage
Beamforming	Microphone	Delay time (estimation)	2D map	Wide band Transient sound	Decrease in accuracy (low frequency range) Ghost (virtual image)
Envelope intensity	Microphone	Hilbert transform	Point cloud	Transient sound	Short time display
Conventional method	Microphone	Mode separation	2D map	Low frequency	Large number of microphone

sound source position is visually shown using a two-dimensional contour diagram. The conventional BF method assumes that the incident wave is a plane wave. The distance between the sound source and the microphone must be sufficiently far away, and the distance must be several times the wavelength. However, this device performs the correction based on the assumption of spherical waves, so that it can also handle measurements from nearby locations.

4. Sound source visualization using driving rotation test device [2]

This chapter provides an overview of the drive rotation test device, the BF measurement method, and correlation analysis.

The test device has the ability to rotate at high-speed (130 km/h for conventional gears). Drive torque is transmitted from the traction motor to the pinion gear via the WN coupling. The axle is connected to another traction motor, which applies torque in the opposite direction to the drive torque to reproduce the meshing condition of the gears. The rotation conditions were acceleration, constant speed, and deceleration, as shown in Fig. 7. The test gear is a conventional line type with a gear ratio of 5.65 (96/17), a module of 6, a pressure angle of 26°, and a helix angle of 23°. Figure 8 shows the measurement position of the small microphone array, and Fig. 9 shows the measurement area of the small microphone array. Measurement position 1 targeted the gearbox side and traction motor side, and measurement position 2 targeted the gearbox top and traction motor top. Position 1 has a height of approximately 1 m from the floor level and a distance of approximately 0.9 m from the measurement area.

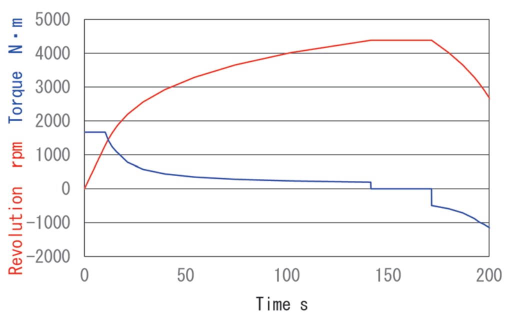

Fig. 7 Operating conditions of drive rotation test device

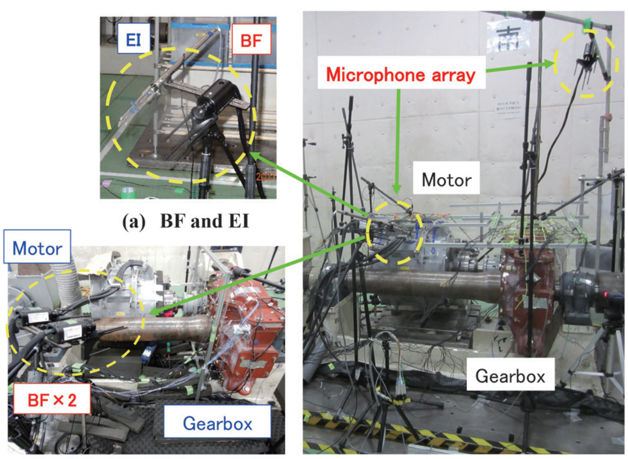

(a) BF and EI

(b) BF (Double unit)

(c) Drive system and microphone array

Fig. 8 Measurement position of small microphone array

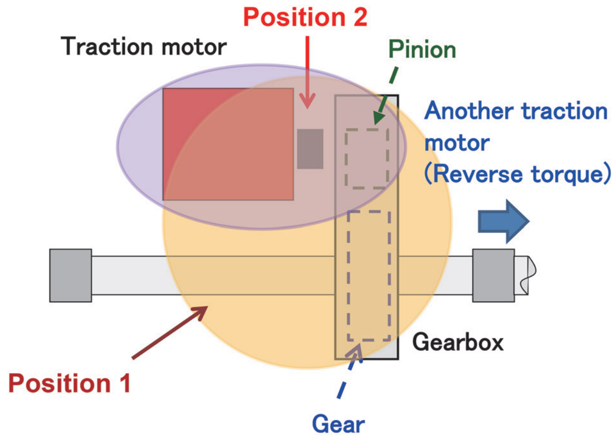

Fig. 9 Measurement area of small microphone array

The wide-angle capability of the camera allows the gear system and the motor to be included in the analysis range at the same time. In this study, we performed sound source visualization measurements using the BF method and correlation analysis using accelerometers. At position 1, we compared the transient sound source movement due to speed changes with the EI method. We also improved the measurement accuracy of the BF method using multiple small microphone arrays.

4.1 Correlation analysis of driving device

Vibrations generated on the plate surface of the drive device may become a source of noise. A vibration accelerometer was attached to the location of the estimated vibration source, and correlation analysis with nearby noise was performed. Correlation analysis was used to identify frequency bands with a high possibility of vibration radiation. By narrowing down the analysis frequency band through analysis, it has become possible to improve the imaging accuracy of noise phenomena and reduce the computational load. A vibration accelerometer was attached to the center of the motor, assuming that vibration in the radial direction of the housing would be the source of noise radiation. Many of the gears used in railway vehicles are helical gears. These gears tend to have larger meshing vibrations in the thrust direction [3]. Because of this tendency, vibration accelerometers were attached to the left and right side of the gearbox near the pinion. Nearby noise measurements were performed using an ultra-compact microphone (MEMS MIC: Ono Sokki MB-2200M10). They were placed close to the gearbox (24 points) and close to the motor (20 points). Figure 10 shows the arrangement of the vibration accelerometer and MEMS MIC used in the correlation analysis. The analysis combinations are shown in ① to ④ in the figure. ④ is the same as the microphone arrangement of the conventional method described in Chapter 6.

4.2 Improving BF imaging accuracy using multiple small microphone arrays

In conventional BF measurements, only one small microphone array device is installed. However, depending on its position, imaging at the center of the sound source may not be stable due to transient sound source movement and acoustic reflection. The measurement environment in this test included multiple sound sources in a

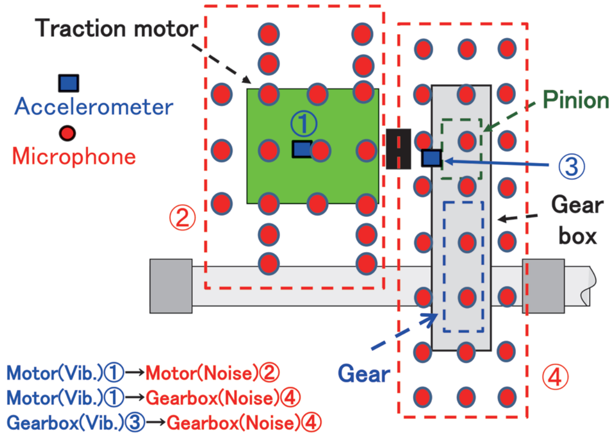

Fig. 10 Correlation analysis of driving device (gearbox and traction motor)

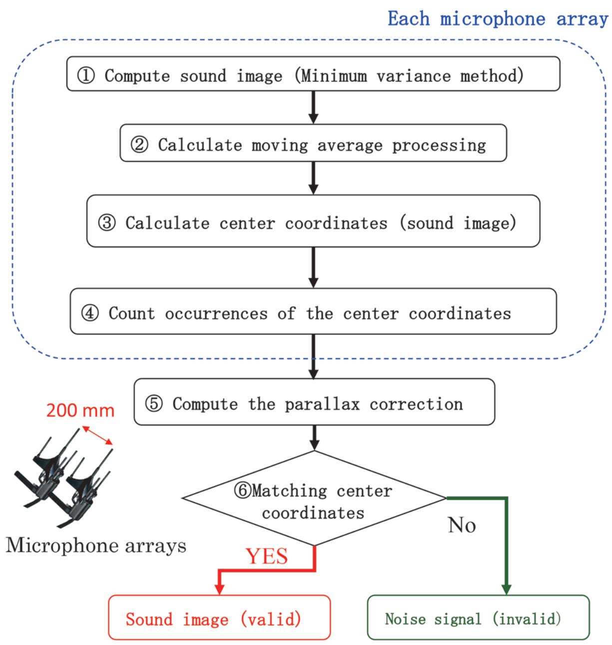

Fig. 11 Microphone array imaging result processing

small space, and the room in which the measurements were carried out was highly reverberant. As an improvement method in this measurement environment, we improved imaging accuracy by using multiple small microphone arrays installed at different locations in the same measurement direction and compositing the processed images. The two small microphone arrays were spaced 200 mm apart in the horizontal direction. Data processing was performed as follows (Fig. 11).

The imaging calculations for each microphone array were performed using the minimum variance method. A moving average process was performed to improve imaging stability. The number of occurrences of the sound source center coordinates after the moving average process over a certain period of time (10 seconds in this case) was calculated. After correcting the parallax between the two small microphone arrays, the sound source center coordinates were superimposed. If the coordinates matched a certain number of times, this was determined to be the center of the sound source. Coordinates that did not match (that is, only one unit was determined to be the center of the sound source) were treated as noise components, rather than the original center of the sound source, and were removed from the test results. In this analysis, the number of matches was set to one.

5. Sound source visualization analysis results [2]

This chapter mainly describes the analysis results regarding sound source separation, transient sound comparison, and imaging stability of the drive device using the BF method.

5.1 Correlation between driving device vibration and noise

Figure 12 is a spectrogram of the noise from the drive device using a small microphone array and shows that the noise level becomes noticeable in the torque load condition (acceleration section) just before reaching the high-speed range (approximately 120 km/h in terms of speed) shown in Fig. 7. Figure 13 shows the correlation analysis results for this selection. Motor noise is the average sound pressure at MEMS MIC (20 points) shown in Fig. 10 ②. Gearbox noise is the average sound pressure at MEMS MIC (24 points) shown in Fig. 10 ④. Vibration and noise near the motor were highly correlated in the high frequency band of approximately 2500 to 3300 Hz. Furthermore, although the correlation was lower than in the case of traction motors, the value with motor vibration and noise near gearbox were also higher in the same frequency band. It can be

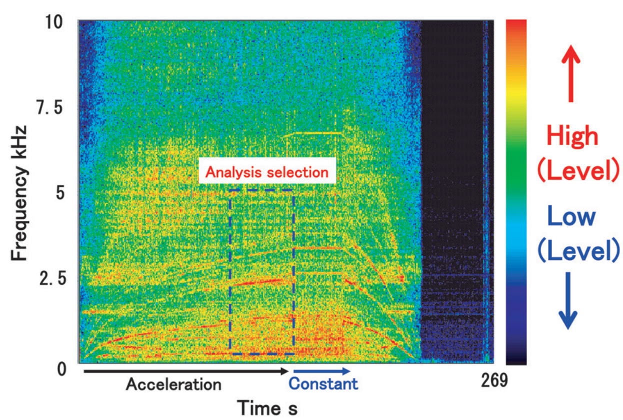

Fig. 12 Spectrogram of drive noise

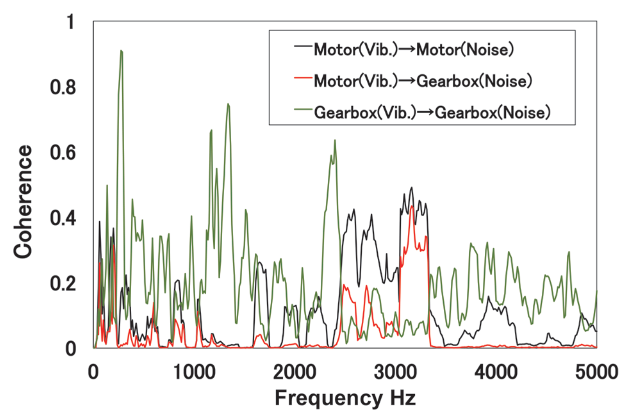

Fig. 13 Correlation between motor and gearbox vibration and noise

seen that motor vibration in this frequency band has a large effect not only on motor noise but also on gearbox noise. On the other hand, the frequency band that has a high correlation between gearbox vibration and noise near the gearbox is 300 Hz to 2400 Hz. This frequency band was thought to include many resonance frequencies of the gearbox and meshing frequency components.

5.2 Driving device sound source center

The BF analysis showed that the correlation between the motor housing vibration and the noise is high at approximately 3150 Hz. Figure 14 (a) and 14 (b) show the center of the sound source in the vicinity of the center of the motor housing. Since the center of this sound source is located in motor core, electromagnetic sound is considered to be generated by exciting vibrations in the radial direction of the housing.

Additionally, the results show that the motor vibration at 3150 Hz has a high correlation with the gearbox noise. As shown in Fig. 15 (a), the result shows that the center of the sound source can also exist in the vicinity of the joint with the gear device. It can be seen that vibrations at this frequency generated by the motor, propagated to the WN coupling, and acoustically radiated from the gearbox. Figure 15 (b) shows the center of the sound source in the vicinity of the gear unit, obtained by the BF analysis in the frequency band (1100 Hz) where the gearbox vibration and the gearbox noise are highly correlated. This frequency band corresponds to the primary meshing frequency of the gear. Since helical gears generate thrust force, it can be seen that the center of the sound source is around the large gear bearing.

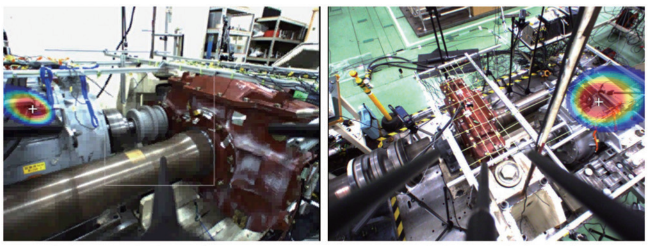

(a) Position 1 (b) Position 2

Fig. 14 Motor sound source center (3150 Hz)

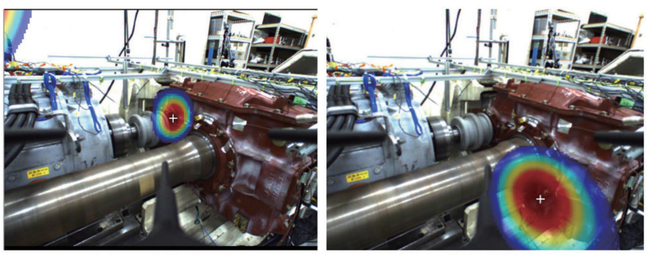

(a) 3150 Hz (b) 1100 Hz

Fig. 15 Gearbox sound source center

5.3 Comparison of sound source visualization methods for transient sounds

When the operating conditions change from acceleration to constant speed, the vibration state of the drive device changes due to changes in the meshing force of the gears and the influence of rotational inertia. This generates transient sounds. The primary frequency of the gear meshing, which is the main noise in the vicinity of the gearbox, is approximately 1200 Hz to 1300 Hz. The area is shown in the enlarged part of Fig. 16. The analysis results using the BF method are shown in Fig. 17 (a). During acceleration, the center of the sound source is seen around the large gear bearing due to the thrust force of the gear (Fig. 17 (a) ①), and when the speed changes to constant speed, the center of the sound source moves to the WN coupling and pinion gear axis (Fig. 17 (a) ②).

At this moment, it is estimated that the center of the sound source moves due to the changes in vibration state caused by the backlash of the WN coupling. It can be seen that the center of the sound source moves again around the large gear bearing or to the

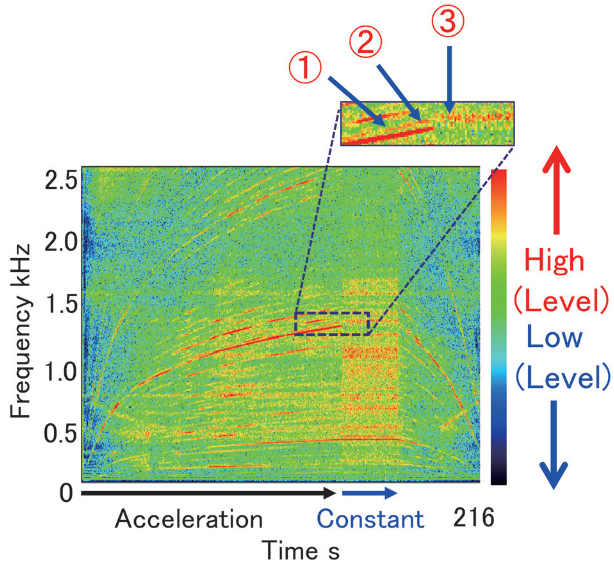

Fig. 16 Spectrogram and analysis selection of drive noise

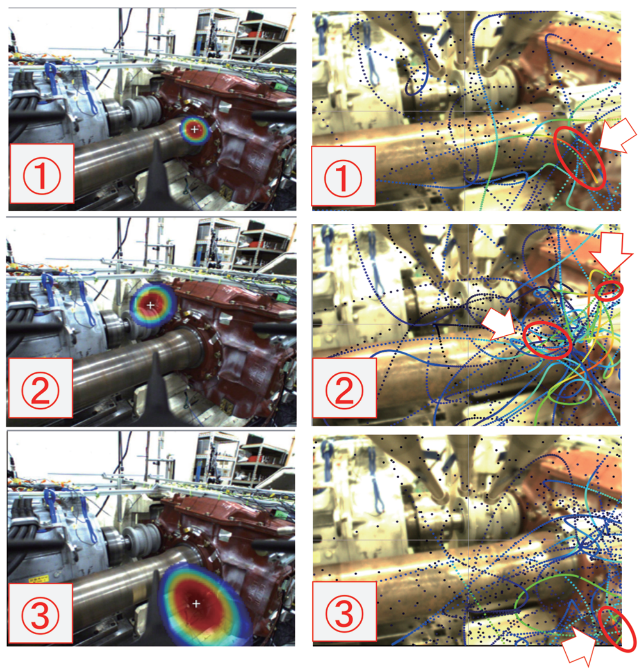

(a) BF method (b) EI method

Fig. 17 Transitional sound source center shift from acceleration to constant speed

rear of the gearbox (Fig. 17 (a) ③). Similarly, the analysis results using the EI method are shown in Fig. 17 (b) ① to Fig. 17 (b) ③. It shows the locus of movement of the center of the sound source every 200 μs, and the red circles indicated by arrows are the locations where the sound pressure is high at a certain moment. The sound source does not move stably as seen in the BF method, and the variation in the sound source area increases. Especially when the sound source moves near the WN coupling, the imaging situation becomes unstable (Fig. 17 (b) ②). In this test environment, in addition to the noise from the drive unit, there are also external noises from rotating equipment and reflections from the floor and walls. For this reason, the EI method with high time resolution is susceptible to disturbances. As a result, it is possible that the imaging stability deteriorates. It can be seen that the BF method provides better results for transient noise evaluation in this measurement environment.

5.4 Improving imaging accuracy using multiple small microphone arrays

Figure 18 (a) shows the trajectory of the center of the sound source with small microphone array (left) when the speed changes for about 10 seconds under acceleration conditions up to the maximum speed (120 km/h). This is indicated by a white +. Similarly, Fig. 18 (b) shows the results for a small microphone array (right). The analysis frequency band is the primary mesh frequency of the gear (1000-1100 Hz). Both results show that the center of the sound source is in the vicinity of the rear part of the gearbox. However, the imaging areas of the two results are significantly different.

The imaging position indicated by the symbol ■ in each figure is the area where the images of the two cameras overlap. Other positions where the images do not overlap (the top of the gearbox and the axle) are not the original center of the sound source, but are considered to be noise components, such as the influence of sound reflected from the floor. By excluding these images, it became possible to determine the center of the sound source with higher accuracy.

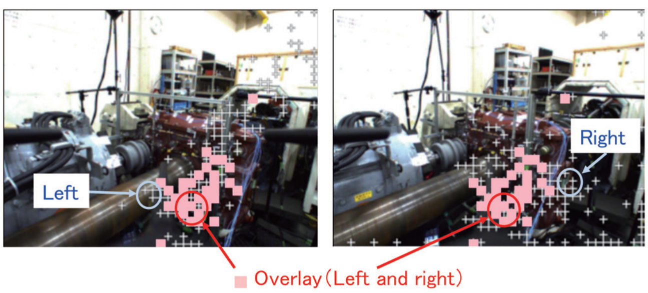

(a) Small microphone array (left)　(b) Small microphone array (right)

Fig. 18　Analysis results using the BF method

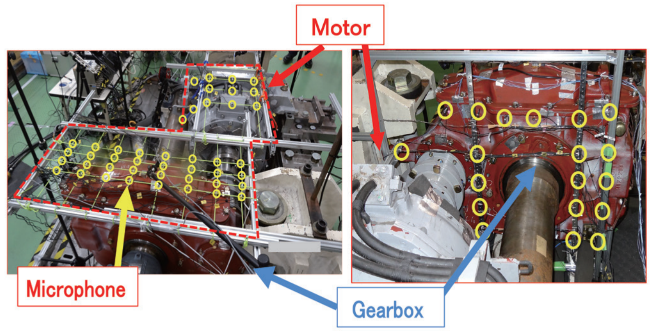

(a) Top surface of gearbox　(b) Side surface of gearbox

Fig. 19　Sound source visualization using conventional method (Drive rotation device)

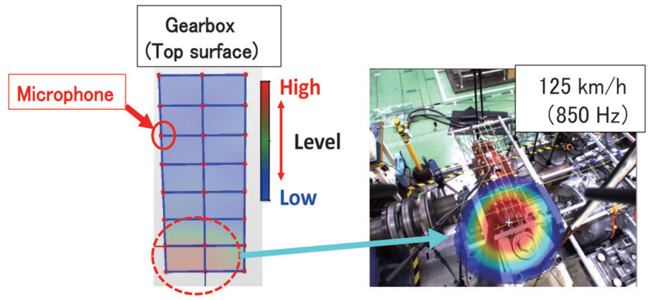

(a) Conventional method　(b) BF method

Fig. 20　Sound source center of sound source visualization method (top of gearbox)

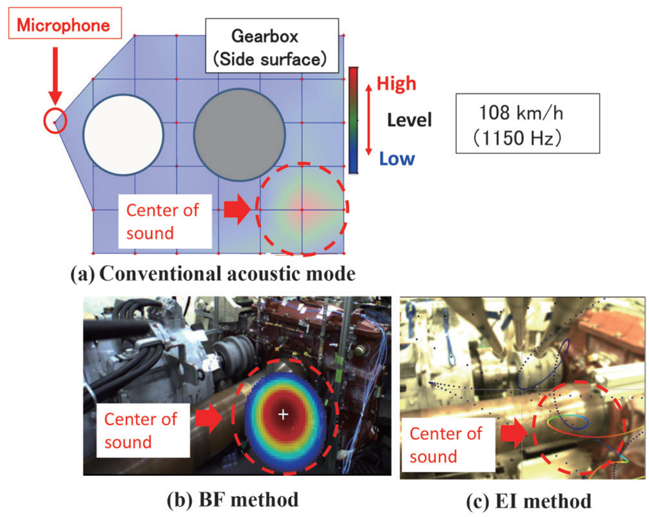

Fig. 21　Sound source center of sound source visualization method (side of gearbox)

6. Verification of effectiveness of sound source visualization method [2]

The effectiveness of both methods was demonstrated by comparing the imaging results of the sound source center obtained by the BF method and the conventional method (acoustic mode method using multipoint microphones) (Fig. 19).

Although the characteristics of the BF method are that imaging cannot be obtained in the low frequency range below 500 Hz, the response was good under acceleration and constant speed conditions during normal operation. The imaging position (center of the sound source) generally matched in both analysis results. Similarly, results with consistent imaging were obtained using the EI method (Fig. 20 and Fig. 21).

7. Other application examples of sound source visualization methods

The sound source visualization method can be applied to analysis in many fields other than drive devices, and we will describe an example of the BF method.

7.1 Application example for rolling noise

Under high-speed conditions (115 km/h) using the rolling stock test stand, the results showed high levels of noise frequency components at 750 Hz and 1100 Hz. There was a difference in the location of rolling noise between the two results. The center of the 750 Hz sound source is on the wheel side (Fig. 22 (a)), and the center of the 1100 Hz sound source is on the roller side (rail side) (Fig. 22 (b)).

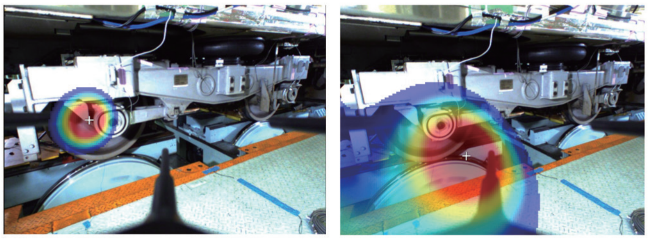

(a) Wheel side sound source (750 Hz) (b) Rail side sound source (1100 Hz)

Fig. 22 Sound source separation of rolling noise using the BF method (115 km/h)

7.2 Application example for gear damage

In addition to identifying the location of noise generation, the sound source visualization method can also be applied to monitoring the state of noise generation by changing the imaging state. In rotation tests at 2000 RPM using small gears, when the gear surface pressure is high (2.25 GPa), pitting fatigue begins to occur at the center of the gear mesh after cumulative rotations of 1.7 million (Fig. 23 (a)). The sound spectrum changes in the high frequency range (above 3000 Hz) centered around the secondary meshing frequency (3500 Hz) compared to the state before damage (Fig. 23 (b)). However, the change in sound cannot be distinguished by hearing. On the other hand, when condition monitoring is performed using the BF method, it is possible to detect damage at an early stage after it has occurred (Fig. 24). After gear damage has occurred, the sound source center of the meshing secondary frequency is located in the vicinity of the center of the bearing between the large gear shaft and the small gear shaft, and it can be seen that the imaging level in this area increases significantly.

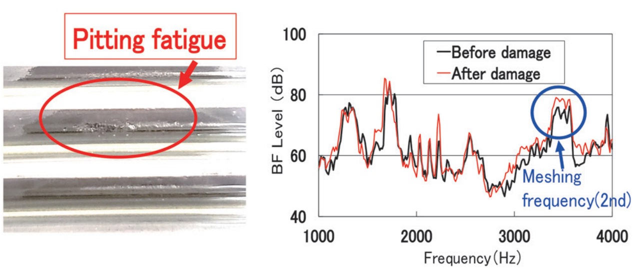

(a) Gear damage (b) Sound spectrum

Fig. 23 Gear pitting fatigue and sound spectrum changes

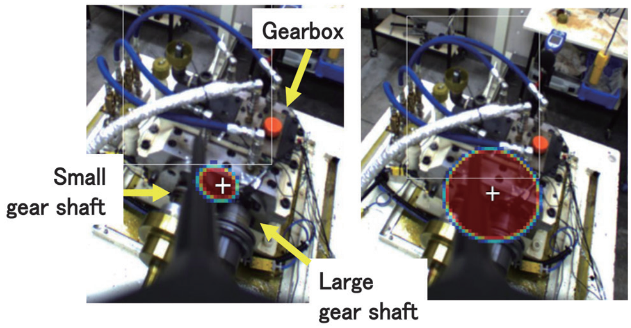

(a) Before damage (b) After damage

Fig. 24 Gear pitting fatigue and sound source imaging (2000 rpm, 3500 Hz)

8. Conclusion

We evaluated the location of noise generation on railway driving devices in bench-scale testing, using a sound source visualization method, mainly based on the BF method. In this study, we obtained the following results:

[1] The driving device rotation test was carried out using correlation analysis of vibration and noise. In this test, we separated the high-frequency sound source (3150 Hz), which is the noise source of the traction motor, and the low-frequency sound source (1100 Hz), which is the noise source of the gear system. It was found that the former sound source is located in the vicinity of the center of the motor housing, and the latter sound source is located in the vicinity of the large gear bearing.

[2] In the analysis of transient sound during changes in operating conditions, it was found that the beamforming method (BF method), which is less susceptible to disturbance effects, has better imaging stability than the envelope intensity method (EI method).

[3] Image processing with several small microphone arrays has improved the imaging accuracy of the BF method.

[4] The effectiveness of the BF and EI methods has been confirmed by comparison with the conventional method (acoustic mode method using multi-point microphones).

Acknowledgment

We would like to express our gratitude for the assistance and cooperation received from Kure National College of Technology, Mitsubishi Electric Corporation, and Ome Casting Co., Ltd., in conducting this research.

References

[1] Ito, K., Seto, M., Ishida, K., Development of sound visualization system using 4ch beamforming, Society of Automotive Engineers of Japan, *Automotive Technology*, Vol. 71, No. 7, "Designing vibration noise," pp. 62-66, 2017 (in Japanese).

[2] Sasakura, M., Takeshita, M., Osodo, T., Mikami, K., Maeda, S.,

Applicability of sound source visualization technology in bench test environment of railway drive equipment, *D&D2023 lecture proceedings*, Japan Society of Mechanical Engineers, 2023 (in Japanese).

[3] Sasakura, M., Suzuki, F., Naga, E., Shimamura, K., Occurrence of gear mesh vibration of railway vehicles and vibration/noise analysis, *D&D2015 lecture proceedings*, Japan Society of Mechanical Engineers, 2015 (in Japanese).

Author

Minoru SASAKURA
Senior Researcher, Traction Systems Laboratory, Vehicle Technology Division
Research Areas: Acoustic, Gear Material.

Numerical Flow Simulation of Increase Mechanism and Method for Suppressing Increase in Lift Force of Pantograph Head for Conventional Trains under Crosswind

Takumi ABE **Koji NAKADE**
Computational Mechanics Laboratory, Railway Dynamics Division

Takeshi MITSUMOJI
Current Collection Laboratory, Railway Dynamics Division

We numerically investigated the aerodynamic characteristics of pantographs for conventional trains in a crosswind by using large-eddy simulations (LESs). Although previous experimental study revealed that the lift force increases significantly under crosswind conditions, the mechanisms underlying this phenomenon have not been clarified. Therefore, the flow fields around the pantograph head were carefully investigated by LESs. It was found that there are two main mechanisms: one is a steady large-scale vortex generated on the upper surface of the pantograph head, and the other is a pressure increase on the lower surface of the pantograph head. In addition, LESs were carried out using modified pantograph head shapes to investigate methods for reducing the lift force on the pantograph head taking into account the mechanisms above. As a result, a maximum lift reduction rate of approximately 60% was achieved, indicating that an effective lift force reduction method was proposed.

Key words: *numerical simulation, conventional line pantograph, lift force characteristics, aerodynamic characteristics, crosswind, LES*

1. Introduction

Optimization of the aerodynamic lift force of pantographs during operation is important to maintain a steady, continuous contact with the overhead wire and leads to a stable power supply. The optimal value of the lift force of conventional line pantographs depends on various conditions of the vehicle and overhead wires, so there are no clear standard values. However, previous research [1] has investigated the lift force characteristics of various pantographs used in commercial operations without problems, where it was reported that the lift force was between several N and around 30 N at a driving speed of 100 km/h. Trains on conventional lines run at lower speeds than Shinkansen trains, so the lift force of the pantograph is less of a problem in normal operation. On the other hand, the lift force can increase due to crosswinds in cases of strong wind, and studies have been carried out on the lift force characteristics of pantographs for conventional rail vehicles in crosswind environments. In general, when a vehicle is subjected to a crosswind, the pantograph is exposed not only to lateral flows but also vertical flows due to the wind blowing upwards along the side of the vehicle, so studies have been carried out on the flow field near the pantograph focusing on the blow-up angle. Experimental studies of the lift force characteristics of single-arm pantographs for conventional lines, which have been increasingly introduced in recent years, have been carried out with the assumption of crosswinds in the various conditions mentioned above [2, 3]. These studies produced findings relating to the wind speed and wind direction of crosswinds that increase the lift force. Additionally, our recent research [4] on increased lift force in case of strong winds, and accidents due to cutting into the overhead wires has shown the limit value of the lift force at which cutting can occur, and there is a need for a method to suppress the increase in lift force.

Many findings have been found on the lift force characteristics, but there has been no research that analyzes the mechanism by which the lift force increases due to crosswind, nor has there been any study of methods for suppressing the lift force increase. Therefore, in this study, we used the numerical analysis method Large-eddy simulation (LES) to elucidate the mechanism of the lift force increase in flows where lift force increases due to crosswinds, and to investigate and evaluate a method for suppressing the lift force increase. In general, the pantograph lift force refers to the change in uplift force due to an aerodynamic force, and this includes the effects of link mechanisms such as the frames. In this study, we defined the vertical upward force caused by an aerodynamic force in the coordinate system fixed by the pantograph as the lift force. We then focused on the pantograph head, which has a large contribution to the lift force of the pantograph, and then discussed the lift force obtained by integrating the pressure distribution on the pantograph head surface.

2. Numerical analysis method

2.1 Simulation model

The simulation target is an actual shape model of a general single-arm pantograph for conventional lines used in wind tunnel experiments [3] using the large, low-noise wind tunnel of the Railway Technical Research Institute. Additionally, we investigated methods for suppressing the increase in the lift force by preparing three different shapes, using the actual shape model as the basic shape and changing the shape of the pantograph head. Figure 1 shows the computational domain and coordinate system. The computational domain was the same for all simulation cases.

Figure 2 shows the actual shape model used in the simulations. This study mainly focuses on the pantograph head lift force characteristics and the flow field around the pantograph head. The computational target was composed of a part of the lower frame, the upper frame, the horns, and the pantograph heads. The simulation grid was an orthogonal irregular grid with uniformly spaced grids with a minimum grid width of Δx=Δy=Δz=2 mm distributed near the pantograph head, with the grid spacing increasing as the distance from

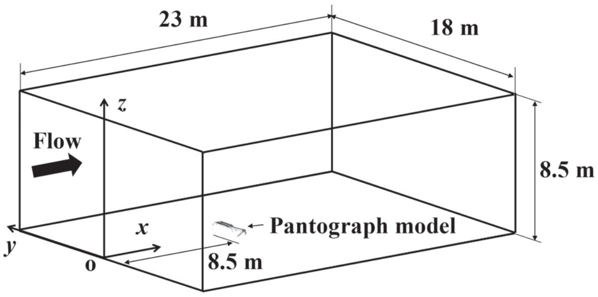

Fig. 1 Computational domain

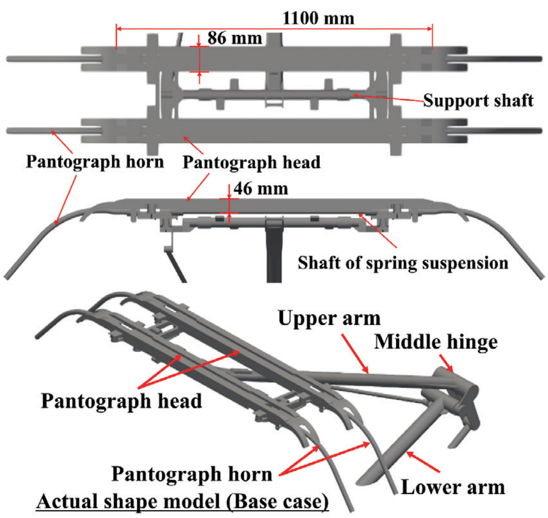

Fig. 2 Pantograph model

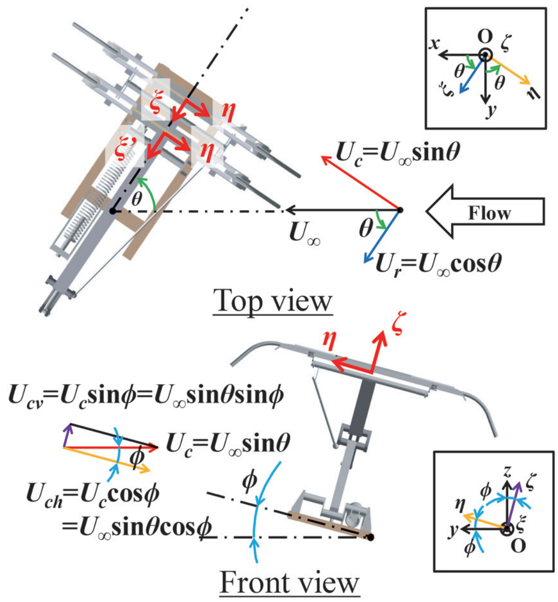

Fig. 3 Relationship between velocity and coordinate system

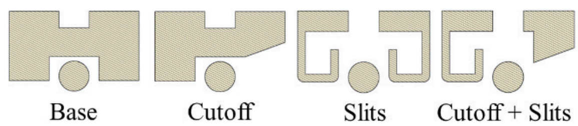

Fig. 4 Cross-sectional shape of pantograph head

the model increased. The number of simulation grids was approximately 1 billion points without crosswind and approximately 1.2 billion points with crosswind.

2.2 Coordinate system and simulation conditions

The mainstream flow velocity was fixed at 80 km/h. The Reynolds number based on the mainstream flow velocity and the pantograph head height (0.046 m) of the actual shape model was approximately 6.8×10^4. Hereafter, unless otherwise noted, the physical quantities that have been made dimensionless were representative velocity U_∞=80 km/h and representative length L=1 m.

We reproduced a crosswind blowing up from the bottom of the pantograph by fixing the incoming wind and rotating the model in the computational area. The coordinate system fixed to the object was defined so that the direction of $\xi\eta\zeta$ corresponded to xyz when there was no rotation. The origin of $\xi\eta\zeta$ was set at the center of the lower surface of the upstream pantograph head, and the origin of $\xi'\eta\zeta$ was set at the center of the lower surface of the downstream pantograph head (the origins of ξ and ξ' differ between the upstream and downstream pantograph heads).

Figure 3 shows the relationship between the yaw angle θ, the roll angle ϕ, and the mainstream flow velocity U_∞ of the pantograph. The yaw angle θ is called the crosswind angle because it expresses the wind direction angle with respect to the traveling train, and the roll angle ϕ is called the blow-up angle because it expresses the blowing up of the crosswind. Additionally, the wind velocity that the train receives from the front while driving is the driving velocity U_r, and the crosswind velocity including blowing up is the crosswind velocity U_c. Reference [5] shows the details of the method of the computation, but the following conditions for the wind direction where the lift force is maximum were used: crosswind angle θ=56°, blow-up angle ϕ=15°, and anti-fluttering conditions with the middle hinge on the downstream side. In all simulation cases, the mainstream velocity was U_∞=80 km/h (equivalent to U_r=45 km/h with crosswind), and when comparing the lift force, the driving velocity was fixed to U_r=60 km/h, and the lift force was converted.

LESs were carried out on the actual shape model ("base case") in both crosswind present and absent conditions (simply referred to as "crosswind present" and "crosswind absent" in Sections 3.1 and 3.2). Additionally, three shapes with different pantograph head shapes were prepared. Figure 4 shows the cross-sectional shape of the pantograph head, and Fig. 5 shows the method used to change the shape and the area in which the shape was changed. In Fig. 4, the cross-sectional shape shows only the upstream pantograph head, but asymmetry in the pantograph shape due to differences in driving direction was eliminated by making the shapes of the upstream and downstream pantograph heads front-to-back symmetrical. For the "cutoff" a diagonal cut was made to the lower edge of the pantograph head, and its range in the η direction is the blue area between the protrusions shown in the figure ($-0.335 \leq \eta \leq 0.335$). Multiple "slits" were made in the top of the pantograph head, and the slits were defined as the area between the pair of sliding plates at the top of the pantograph head ($-0.55 \leq \eta \leq 0.55$). The "combined type" indicates a pantograph head where both changes are made to the basic shape, i.e., a cutoff and slits. Here, the "slits" and the "combined type" pantograph heads were made hollow to match the structure of the model used in the wind tunnel experiment [4]. However, during

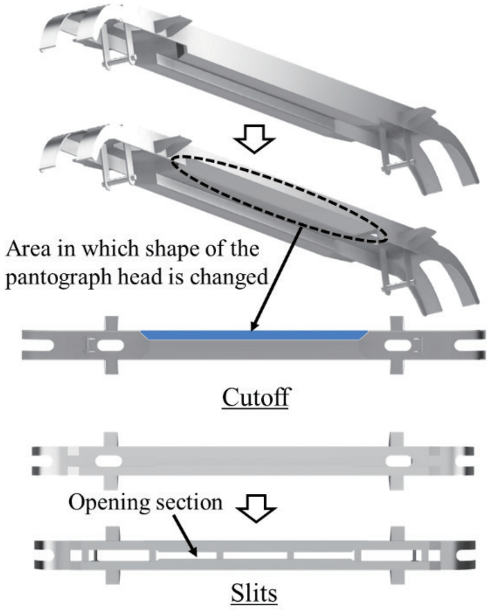

Fig. 5 Pantograph head shape change method

the study stage, numerical analysis was conducted on many more shapes. The shapes described in this paper were those selected for their relatively large lift force reduction effect.

2.3 Overview of numerical simulation

The basic equation of LES for incompressible fluids was discretized using the finite difference method. The coherent structure Smagorinsky model [6] was used as the subgrid scale model. A second-order central difference method [7] was used for spatial discretization, and a third-order Adams-Bashforth method was used for time integration. We solved the Poisson equation for pressure by using the Jacobi method, where the average pressure value of the entire simulation area was used as the reference pressure. The boundary conditions were as follows: the velocity was fixed at 1 at x_{min} (inflow surface) and the convective outlet condition was set at x_{max} (outflow surface); and the pantograph surface was set as a no-slip boundary condition with zero velocity, and the far boundary surface (y_{min}, y_{max}, z_{min}, z_{max}) was set as a slip boundary condition. The model shape was expressed using a voxel-based orthogonal grid method.

In this simulation, a uniform flow was used as the initial value, and a time integration was performed until the flow field reached a statistically steady state. The dimensionless time step interval was set to Δt=0.0002. Statistics such as pressure coefficients were calculated by averaging the calculation results for T=10 – 30 in dimensionless time.

3. Analysis results and discussion

3.1 Comparison of wind tunnel experiments and simulation results

We verified the validity of the numerical simulation results by conducting a wind tunnel experiment and compared the pressure coefficient distribution on the surface of the pantograph head, where we confirmed that the two results were generally in good agreement. See reference 6 for details.

3.2 Mechanism of increase in pantograph head lift force due to crosswinds

3.2.1 Change in pantograph head lift force due to crosswinds

We investigate the increase in pantograph head lift force due to crosswinds. The mainstream flow velocity is often assumed to be constant when examining the aerodynamic force acting on an object, but here, we sought to investigate the changes in the pantograph head lift force due to crosswinds under constant velocity conditions by unifying the flow velocity in the direction of travel at U_r=60 km/h. The simulation uses a mainstream flow velocity of U_∞=80 km/h, but reproducing the above conditions requires U_∞=108 km/h for the crosswind conditions. Since the dimensionless lift force in the experiment in the velocity range considered in this study (U_∞ of approximately 60–180 km/h) was approximately equal regardless of the flow velocity, the dependence of the flow field on the Reynolds number is likely to be small, and the converted lift force shown in (1) and (2) below was calculated, assuming that the lift force is proportional to the square of the flow velocity:

$$L_{\mathrm{A\_u60}} = (60 / 80)^2 \times L_{\mathrm{A\_u80}} \quad (1)$$

$$L_{\mathrm{B\_u108}} = (108 / 80)^2 \times L_{\mathrm{B\_u80}} \quad (2)$$

where subscripts A and B indicate “crosswind absent” and “crosswind present,” respectively, and the number after u indicating the U_∞ value.

Table 1 shows the lift forces of the two front and rear pantograph heads calculated from (1) and (2) for the two cases of crosswind present and absent, together with the experimental results. Here, the total value of the two pantograph head lift forces in the experimental results (Lift 1 + Lift 2, henceforth “total lift force”) is calculated by subtracting the pantograph lift force with the two pantograph heads removed from the lift force measurement results for the entire pantograph including the pantograph head, and thus simulating the lift force due to the aerodynamic force exerted on the two pantograph heads. Meanwhile, in the numerical simulations, the lift force was calculated from the aerodynamic force acting on the object (integral value of the pantograph head surface pressure). As mentioned above, the lift force due to the aerodynamic force acting on the pantograph head was calculated using different methods in the experiment and the numerical simulation, but the total lift force in Table 1 was in good agreement between the experiment and the

Table 1 Comparison of experiment and simulation of pantograph head lift force

Case name	Mainstream [km/h]	Lift 1 [N] (Upstream pantograph head)	Lift 2 [N] (Downstream pantograph head)	Lift 1 + Lift 2 [N]
Crosswind absent (experiment)	60	—	—	2.53
Crosswind present (experiment)	108	—	—	41.0
Crosswind absent (simulation)	60	0.280	1.28	1.56
Crosswind present (simulation)	108	31.3	12.1	43.5

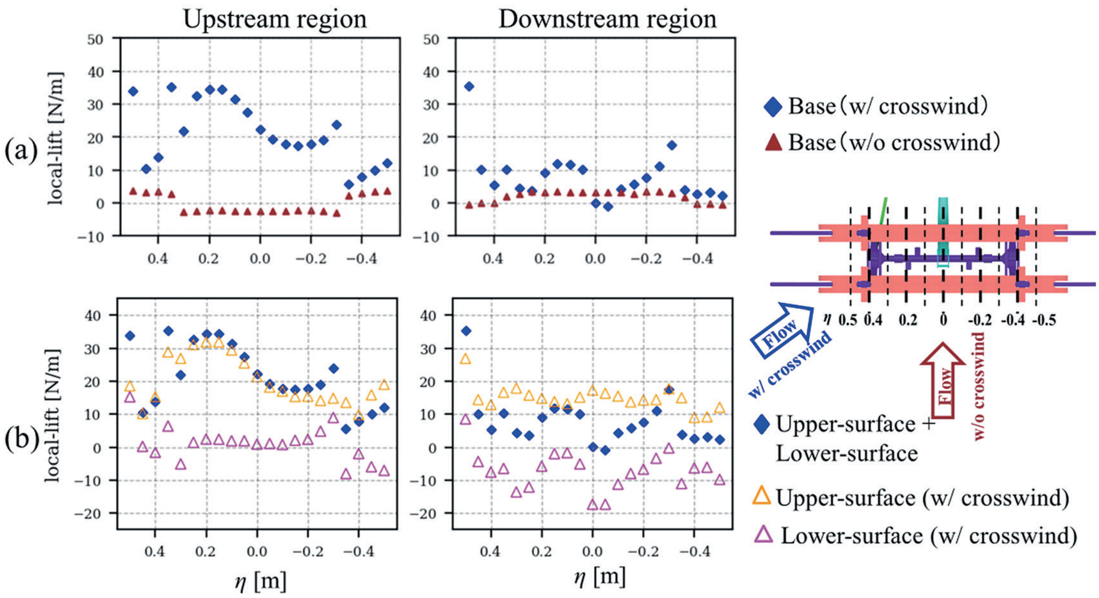

Fig. 6 Local lift force distribution (comparison between crosswind present and crosswind absent)

numerical simulation. Table 1 shows that the crosswind increased the total lift force by approximately 40 N in both the experiment and the simulation. Additionally, the simulation results showed that the increase in lift force of the upstream pantograph head due to crosswinds (Lift 1) was larger than the lift force of the downstream pantograph head (Lift 2), accounting for approximately 3/4 of the total lift force with crosswind present. The reason for the difference in the increase in lift force between the two pantograph heads is discussed below.

Figure 6(a) shows the local lift force distribution in the span direction (direction perpendicular to the rail) of the upstream and downstream pantograph heads for the cases of crosswind present and absent. The local lift force was determined by integrating the C_p distribution around the pantograph head in each η cross-section over a unit width in the η direction. The left and right figures are for the upstream and downstream pantograph heads, respectively, and the left side of the η axis is the upstream side of the crosswind. In the case of crosswind absent, the local lift force is almost uniform in the span direction, but in the case of crosswind present, the lift force is high overall and has a distribution with local peaks. In particular, a locally significant increase in the lift force is observed near the ends of the two pantograph heads in the positive η direction and near η=0.2 of the upstream pantograph head.

For the pantograph head lift force in the case of crosswind present, we sought to clarify the breakdown of the lift force on the upper and lower surfaces by separately showing the local lift force distribution on the upper and lower surfaces in Fig. 6(b). Here, the lift force on the upper surface is the integral value of the difference between the upper surface pressure and the reference pressure, and the same applies to the lower surface.

First, for the upstream pantograph head, the lift force distribution on the upper surface peaks around η=0.2, but the change in the lift force distribution on the lower surface is small. As a result, the influence of the lift force on the upper surface is strongly expressed, suggesting that there is an important aerodynamic phenomenon on the upper surface of the pantograph head. Next, for the downstream pantograph head, the peak of the local lift force on the upper surface around η=0.2 that was observed on the upstream side disappears, and the lift force on the lower surface becomes locally small. Both contributed to the reduction of the lift force, and the lift force was reduced more than on the upstream side. Possible causes of the difference in lift force between the two pantograph heads include flow interference between the pantograph heads and differences in the position of the pantograph members relative to the mainstream.

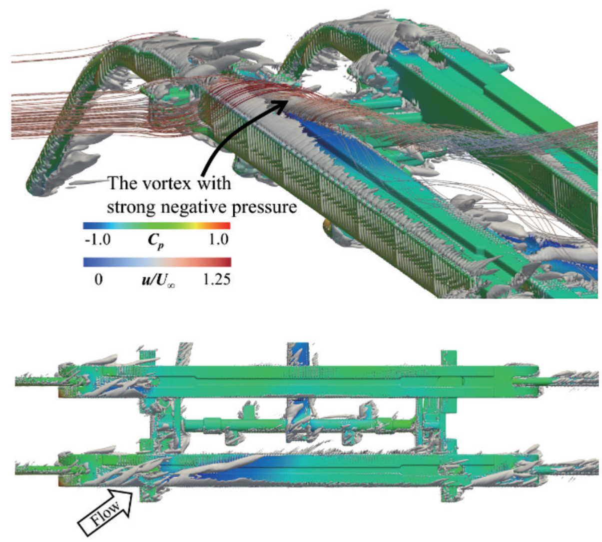

Fig. 7 Flow on upper surface of pantograph head

3.2.2 Comparison of flow fields

Figure 7 shows the time-averaged flow field with crosswind present. The gray area shows the isosurface of the Q value (second invariant of the velocity gradient tensor), the streamlines are colored by the magnitude of the flow velocity, and the pantograph surface is colored by the C_p value. The overhead view shows that the flow that collides with the front surface of the upstream pantograph head separates upward, gets caught up in the upper surface of the pantograph head, and is advected downstream, which creates a steady

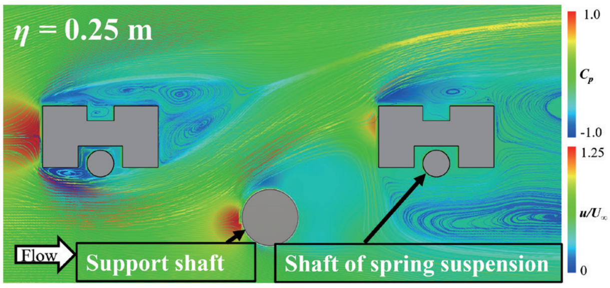

Fig. 8 Flow within cross-section (crosswind absent)

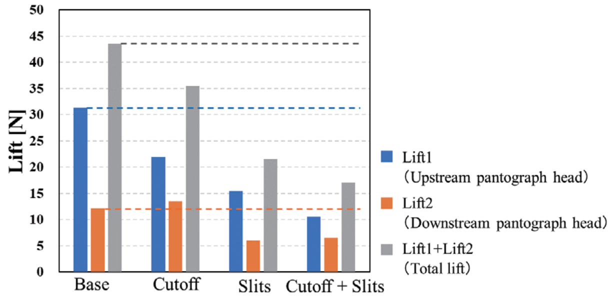

Fig. 10 Change in pantograph head lift force

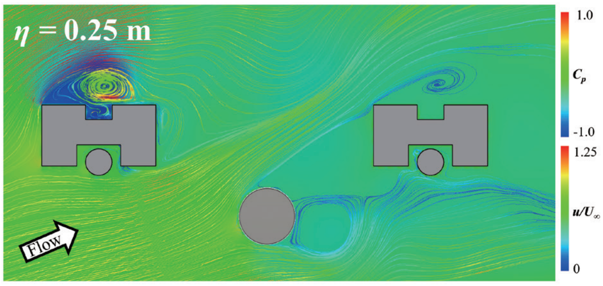

Fig. 9 Flow within cross-section (crosswind present)

vortex. The top view shows that a strong negative pressure region spreads over the top of the pantograph head near this steady vortex, contributing to the significant increase in Lift 1 in Table 1.

Figures 8 and 9 show the flow within the η cross-section (cross-section between pantograph support and upper frame) of the time-averaged flow field. In the case with crosswind absent, the flow collides with the front of the upstream pantograph head, causing separation on the top and lower surfaces. The negative pressure caused by the separation of the upper and lower surfaces is balanced, and the pantograph head lift force becomes slightly positive with the crosswind absent. With crosswind present, the steady vortex shown in Fig. 7 can be seen near the top of the upstream pantograph head, and strong negative pressure is generated.

Additionally, unlike the case with crosswind absent, the flow acts from the bottom of the pantograph head, so the separation and reattachment does not occur on the lower surface, and no low-pressure areas are visible. Therefore, it is thought that the increase in negative pressure on the upper surface of the pantograph head due to the steady vortex and the disappearance (increase in pressure) of the negative pressure area on the lower surface of the pantograph head due to the blowing up wind resulted in a significant increase in the lift force of the upstream pantograph head. Similarly, for the downstream pantograph head, the locally strong negative pressure area on the upper surface and the pressure increase on the lower surface are thought to contribute to an increase in the lift force.

3.3 Method for suppressing increase in pantograph head lift force

3.3.1 Effect of suppressing lift force increase by changing pantograph head shape

In the previous section, we investigated the phenomenon where the pantograph head lift force increased due to crosswinds. In this section, we used the fluid phenomena described in the previous section as a basis to investigate a pantograph head shape that suppresses the increase in pantograph head lift force, and evaluated its effectiveness. The three pantograph head shapes to be examined are shown in Fig. 5 (cutoff, slits, and combined type), and the pantograph head lift force was compared using the conversion equation (2) when the train was traveling at a speed of 60 km/h.

Figure 10 shows the lift force of the pantograph head obtained with the "base case" and three shapes. The lift force is shown separately for the upstream pantograph head and the downstream pantograph head, and the total lift force of the two pantograph heads is also shown. First, in the "cutoff" case, where "cutoff" is made in the lower surface of the pantograph head, the lift force of the upstream pantograph head was significantly reduced, and the total lift force was 18.5% lower than with the "base case." Secondly, in the "slits" case, where "slits" are made on the top and lower surfaces of the pantograph head, the lift force reduction rate of the upstream pantograph head was higher than that of the "cutoff," and lift force of the downstream pantograph head also significantly decreased. As a result, the total lift force was reduced by 50.7% compared to the "base case," and its effect of suppressing the increase in lift force was more prominent than that of the "cutoff." Additionally, in the "combined type" that has the features of both the "cutoff" and "slits," the lift force of the upstream pantograph head was further reduced than that of the "slits," and the total lift force reduction rate reached 60.8%, which was the largest effect obtained. Here, in the "slits" case, the reduction rate of the upward (ζ direction) projected area of the pantograph head due to the slits was approximately 18%, but the reduction rate in the total lift force of the pantograph head was 50.7%, which was greater than the reduction in the pressure-receiving area of the pantograph head. This suggests that the reduction in the lift force due to the slits was not only due to a decrease in the pressure-receiving area but also due to a change in the flow field.

3.3.2 Comparison of flow fields

Figure 11 shows the flow within the η cross-section of three shapes. Compared to the "base case" in Fig. 9, the "cutoff" expands the flow path between the lower surface of the upstream pantograph head and the support shaft, which alleviates the pressure rise on the lower surface and also creates a low-pressure area in the wake of the cylindrical shaft of the spring suspension, which contributes to a reduction in the lift force. Additionally, the steady vortex on the upper surface is weakened due to changes in the flow of the lower surface, thereby weakening the negative pressure. The lift force of the upstream pantograph head is thought to have decreased due to this change in the flow on the upper and lower surfaces. In the "slits" case, the vortex on the upper surface of the upstream pantograph head disappeared due to the flow passing through the slits that penetrates the pantograph head vertically, and the region of strong negative pressure disappeared (see Fig. 12 for details). Here, the

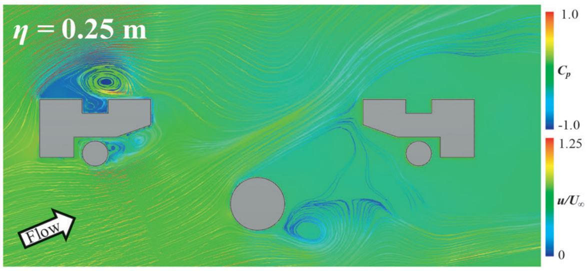

(a) Cutoff

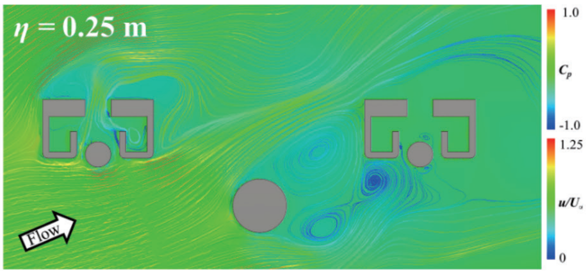

(b) Slits

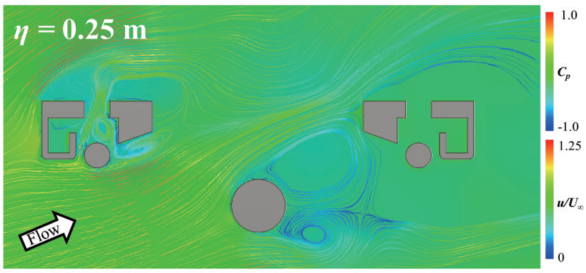

(c) Combined type

Fig. 11 Flow within cross-section of three shapes

low-pressure area behind the shaft of the spring suspension due to the cutoff and the disappearance of the negative pressure on the upper surface due to the slits are different fluid phenomena, and both effects are simultaneously obtained in the "combined type," which is thought to have maximized the effect of suppressing the increase in pantograph head lift force.

Figure 12 shows the time-averaged flow field of the "slits" around the pantograph head. Compared to the "base case" in Fig. 7, the slits had streamlines that can be seen passing from the lower surface to the upper surface. The flow passing through these slits interferes with the stational vortex with negative pressure on the upper surface, and the stational vortex almost disappears, weakening the negative pressure on the upper surface of the pantograph head. This flow interference is also seen at the slits near both ends of the pantograph head in the span direction, and the stational vortex on the top of the pantograph head seen in the "base case" are weakened throughout. This is thought to be the main fluid phenomenon that caused the lift force to decrease significantly with the "slits."

3.4 Examination of simulation results from wind tunnel experiment

We carried out an experiment on the results of the numerical simulation when changing the pantograph head shape discussed in the previous section. In the "slits" case, the shapes of the simulation model and the experimental model were the same, and the total lift forces were in good agreement between simulation and experiment

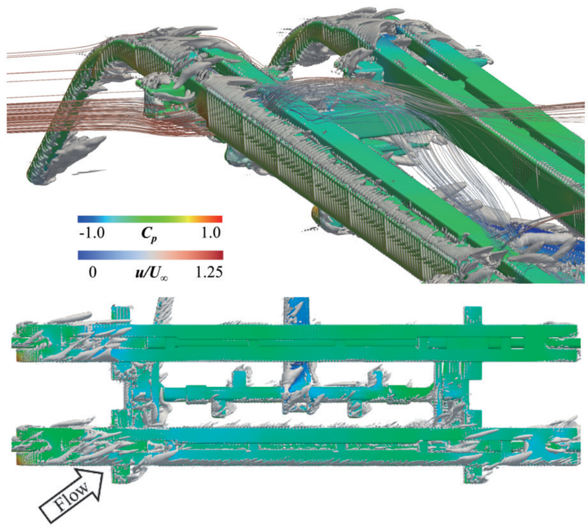

Fig. 12 Flow in upper surface of the pantograph head (slits)

(see reference 5 for details of the experiment). Additionally, in the "cutoff" case and the "combined type," there were differences in the shape of the simulation model and the experimental model but it was confirmed that the same lift force could be obtained with similar shapes [5]. Therefore, the simulation results properly reproduce the fluctuation in pantograph head lift force and demonstrate the usefulness of what was examined in this study.

4. Summary

In this study, we carried out a numerical analysis using LES on a pantograph for conventional rail vehicles running in a crosswind environment, where we clarified the factors that increase the pantograph head lift force due to crosswinds and evaluated the effect of suppressing increase in lift force when changing the pantograph head shape. The findings obtained from this study are summarized below.

(1) In a crosswind environment, the lift force of the upstream pantograph head is approximately 3/4 of the total lift force of both upstream and downstream pantograph heads.

(2) The lift force of the pantograph head in a crosswind environment is increased due to the vortex with negative pressure on the top surface of the pantograph head and the pressure increase due to the flow impinging on the lower surface. The vortex on the upper surface is generated when the flow separated at the leading edge of the pantograph head gets caught back on the upper surface of the pantograph head. This creates an area of strong negative pressure in the vicinity and contributes to an increase in lift force. For the flow on the lower surface, the negative pressure associated with the separation and reattachment flow in the absence of crosswind disappears due to the flow from the bottom side, and the pressure increases, which in turn contributes to an increase in lift force.

(3) The pantograph head shape was changed, and the effect of suppressing the increase in lift force was investigated. All the changes made to the basic pantograph head, namely, adding a cutoff, making slits and combining the two, reduced the lift force. The reductions in lift force were 18.5%, 50.7%, and 60.8%, respectively.

(4) In the “cutoff” case, the flow path is extended from the lower surface of the pantograph head on the upstream side to the upper surface of the pantograph head on the downstream side, which creates negative pressure on the lower surface and weakens the vortices associated with the negative pressure on the upper surface, thereby achieving the reduction effect in lift force. In the “slits” case, the reduction in the pressure-receiving area due to the slits as well as the interference of the flow that passes through the slits with the vortices on the top of the pantograph head weaken the negative pressure and achieve a high lift force reduction effect. The fluid phenomena of the two shapes are different, so the highest effect of suppressing the increase in lift force is achieved by combining both shapes.

References

[1] Aboshi, M., Shimizu, M., Yoshiyuki, H., “Aerodynamic characteristics of narrow-gauge line’s pantograph,” *RTRI Report*, Vol. 6, No. 9, pp. 25-32, 1992 (in Japanese).
[2] Kobayashi, S., Mitsumoji, T., Usuda, T., Yamashita, Y., Tsunemoto, M., Kiyono, T., Adachi, I., “Lift force of pantograph for conventional railways in crosswind ambient,” *J-RAIL2018*, 2018 (in Japanese).
[3] Isono, T., Mitsumoji, T., Hirakawa, H., Usuda, T., “Effects of Pantograph Head Variation on Lift-Force Characteristics of Conventional Railway Pantograph under Cross-Wind Environment,” *TRANSLOG2019,* 2019 (in Japanese).
[4] Mitsumoji, T., Amano, Y., Abe, T., Kobayashi, S., Nakade, K., Noguchi, Y., “Countermeasures to Prevent Dewirement Incident of Conventional Railway Pantographs Based on Lift Force Characteristics Under Crosswind,” *RTRI Report*, Vol. 38, No. 4, pp. 1-7, 2024 (in Japanese).
[5] Abe, T., Nakade, K., Mitsumoji, T., “Numerical flow simulation of mechanism of increase and method for suppressing increase in lift force of pantograph head of conventional line pantograph under crosswind,” *Transactions of the JSME*, Vol. 89, No. 926, 2023, pp. 23-00121 (in Japanese).
[6] Kobayashi, H., “The subgrid-scale models based on coherent structures for rotating homogeneous turbulence and turbulent channel flow,” *Physics of Fluids*, Vol. 17, 2005, pp. 045104-1-12.
[7] Kajishima, T., “Finite-Difference Method for Convective Terms using Non-Uniform Grid,” *Transactions of the JSME*, Vol. 65, No. 633, 1999, pp. 1607-1612 (in Japanese).

Authors

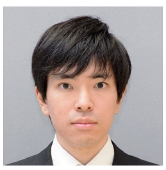

Takumi ABE
Researcher, Computational Mechanics Laboratory, Railway Dynamics Division
Research Areas: Fluid Mechanics, Computational Fluid Dynamics

Koji NAKADE
Senior Chief Researcher, Head of Computational Mechanics Laboratory, Railway Dynamics Division
Research Areas: Fluid Mechanics, Computational Fluid Dynamics

Takeshi MITSUMOJI
Senior Researcher, Current Collection Laboratory, Railway Dynamics Division
Research Areas: Aerodynamics and Aeroacoustics around Current Collection Equipment

Study on Parameter Setting for Deformation Characteristics in a Dynamic Ground Response Analysis

Keigo TSUKIOKA
Soil Dynamics and Earthquake Engineering Laboratory, Center for Railway Earthquake Engineering Research

Yasutomo YAMAUCHI
Dia Nippon Engineering Consultants Co., Ltd.

Masanori YAMAMOTO **Tomoya ONODERA** **Jun IZAWA**
Soil Dynamics and Earthquake Engineering Laboratory, Center for Railway Earthquake Engineering Research

In this paper, setting and testing methods for deformation characteristics of soils for a dynamic ground response analysis were studied. First, we proposed a parameter setting method using an optimization technique and it was confirmed that the proposed method could be used to set the parameters more accurately than three designers with different experience. Second, deformation characteristics tests with some cyclic numbers were carried out. The result showed that a slight difference in cyclic numbers causes quite large differences in the shear stiffness in large strain levels. In addition, a series of ground response analyses was carried out using the above-mentioned parameter-setting method with some test results. The results showed that differences in the number of cycles at each strain level may affect the results of the dynamic ground response analysis. Moreover, it was also confirmed that by using the shear stiffness obtained from monotonic loading test results we can accurately evaluate the dynamic response of the surface ground observed in the hybrid dynamic ground response analysis and simulate real soil behavior.

Key words*: *dynamic ground response analysis, GHE-S model, deformation characteristic parameter

1. Introduction

A dynamic ground response analysis is used in practice as a recommended method for seismic design of Japanese Railway structures [1], to whose analysis the GHE-S model [2] which can precisely reproduce deformation characteristics of soils from small to large shear strain level is applied. As the parameters for the GHE-S model are usually set to fit deformation characteristics obtained from laboratory tests by a designer, accuracy of the analysis greatly depends on how to set the parameters and how to obtain the deformation characteristics. In this paper, therefore, setting and testing methods for deformation characteristics of soils for a dynamic ground response analysis were studied.

First, we examined parameter setting for deformation characteristics (Chapter 2). The parameters of the GHE-S model are usually determined by trial and error to fit the deformation characteristics. To save labor and improve accuracy of parameter settings, we proposed a parameter setting method using an optimization technique. To verify the effectiveness of the proposed method, deformation characteristics parameters were identified by the proposed method for several soils, and it was compared with the identification results by three designers with different experience.

Second, testing methods for deformation characteristics were studied (Chapter 3). To determine the shear stiffness-shear strain relationship of soils, cyclic shear tests are usually carried out to obtain the shear stiffness of shear stress and strain relationships observed in seconds by changing shear strain levels. Although the Japanese Geotechnical Society recommends that cyclic shear be repeated 11 times and the cyclic shear stiffness be calculated at the 10th cycle (Japanese Geotechnical Society, 2020), it is well-known that the number of cycles greatly influences the shear stiffness-shear strain relationship. Therefore, to clarify the effect of the number of cycles, deformation characteristics tests with some cyclic numbers were carried out. In addition, to verify the effect of differences of the number of cycles on a dynamic ground response analysis, a series of ground response analyses was carried out by using some test results with the different number of cycles.

In this study, the GHE-S model was used as the soil constitutive law.

2. Study on parameter setting

In this section, the GHE-S model is described first. The proposed optimization method and the results of the validation calculations are described next.

2.1 GHE-S model

Increased shear strain due to undrained cyclic loading during large earthquake results in the stress-strain (τ-γ) relationship changing from a spindle-shape to an inverted S-shape when the shear strain exceeds 1%, and the hysteretic damping changing from a monotonic increase to a decrease. The GHE-S model has been proposed as a nonlinear model that can express this behavior [2]. The GHE-S model uses the general hyperbolic equation (GHE) model [3] for the skeleton curve, which is improved by changing the Masing's similitude rule that is used for the hysteresis law according to the shear strain to make the hysteresis curve into an inverted S-shape and allowing for the expression of the decrease in hysteretic damping.

The GHE-S skeleton curve model is shown in the following (1) and (2):

$$y = \frac{x}{\dfrac{1}{C_1(x)} + \dfrac{x}{C_2(x)}} \tag{1a}$$

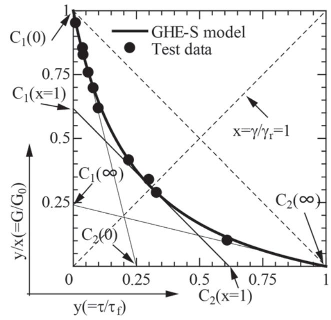

Fig. 1 Overview of GHE-S model parameters

$$C_1(x) = \frac{C_1(0) + C_1(\infty)}{2} + \frac{C_1(0) - C_1(\infty)}{2}\cos\left(\frac{\pi}{\alpha/x + 1}\right) \tag{1b}$$

$$C_2(x) = \frac{C_2(0) + C_2(\infty)}{2} + \frac{C_2(0) - C_2(\infty)}{2}\cos\left(\frac{\pi}{\beta/x + 1}\right) \tag{1c}$$

$$\alpha = \frac{\pi}{\cos^{-1}\left(\dfrac{2C_1(1) - C_1(0) - C_1(\infty)}{C_1(0) - C_1(\infty)}\right)} - 1$$

$$\beta = \frac{\pi}{\cos^{-1}\left(\dfrac{2C_2(1) - C_2(0) - C_2(\infty)}{C_2(0) - C_2(\infty)}\right)} - 1 \tag{2}$$
$$h = h_{\max}(1 - G/G_0)^{\kappa}$$

where $x = \gamma/\gamma_r$ is the normalized strain, $y = \tau/\tau_f$ is the normalized shear stress, γ_r is the reference strain, and τ_f is the shear strength. Figure 1 shows the relationship between the deformation characteristic test results on the $G/G_0 \sim \tau/\tau_f$ axis and the GHE-S model parameters. As shown in (1) and (2), in the GHE-S model, a total of eight parameters need to be set: the six parameters $C_i(0)$, $C_i(1)$ and $C_i(\infty)$ ($i = 1,2$) for the skeleton curve, and the two parameters of $h_{\max}$ and κ for the hysteretic damping. As shown in Fig. 1, $C_1(0)$ and $C_2(\infty)$ are 1.0, so six parameters need to be set.

2.2 Optimization method

2.2.1 Overview of optimization method

We used the optimization method to estimate the parameters for the skeleton curve of the GHE-S model that fit the deformation characteristic test data. We used the optimization program SolvOpt [4] for estimation. SolvOpt is based on the iterative Shor's algorithm, and it supports both constrained and unconstrained nonlinear optimization problems. The unknown variable $\boldsymbol{m}$ to be obtained by the optimization method in this paper is the following six GHE-S parameters mentioned above:

$$\boldsymbol{m} = (C_1(\infty), C_1(1), C_2(0), C_2(1), h_{\max}, \kappa)^T \tag{3}$$

2.2.2 Setting constraint conditions (upper and lower limits)

The constraint conditions shown in (4) were imposed between each parameter based on the relationships in Fig. 1 to exclude physically meaningless solutions in parameter identification:

$$\begin{cases} 0 < C_1(\infty) < C_1(1) < C_1(0) = 1 \\ 0 < C_2(0) < C_2(1) < C_2(\infty) = 1 \end{cases} \tag{4}$$

Additionally, we referenced previous results to set the following upper and lower limits of the search range for the hysteretic damping parameter $h_{\max}$. For κ, only the lower limit was set; the upper limit was not set because the effect on the analysis results was small.

$$\begin{cases} 0.1 < h_{\max} < 0.5 \\ \kappa > 0 \end{cases} \tag{5}$$

2.2.3 Setting objective function (residual) and its characteristics

The objective function was set as the sum of the squares of the residuals of the GHE-S model and deformation characteristic test, as shown in (6):

$$E(\boldsymbol{m}) = E_1(\boldsymbol{m}) + E_2(\boldsymbol{m}) + E_3(\boldsymbol{m}) + E_4(\boldsymbol{m}) \tag{6a}$$

$$\begin{aligned} E_1(\boldsymbol{m}) &= \sum_{i=1}^{N_c}\left\{y(\boldsymbol{x})_i^{\text{cal.}} - (\tau/\tau_f)_i^{\text{test}}\right\}^2 \\ E_2(\boldsymbol{m}) &= \sum_{i=1}^{N_c}\left\{y(\boldsymbol{x})_i^{\text{cal.}} - (\tau/\tau_f)_i^{\text{test}}\right\}^2 \\ &\quad + \sum_{i=1}^{N_c}\left\{y/x(\boldsymbol{x})_i^{\text{cal.}} - (G/G_0)_i^{\text{test}}\right\}^2 \\ E_3(\boldsymbol{m}) &= \sum_{i=1}^{N_c}\left\{y/x(\boldsymbol{x})_i^{\text{cal.}} - (G/G_0)_i^{\text{test}}\right\}^2 \\ E_4(\boldsymbol{m}) &= \sum_{i=1}^{N_c}\left\{h(\boldsymbol{x})_i^{\text{cal.}} - h_i^{\text{test}}\right\}^2 \end{aligned} \tag{6b}$$

where E_1, E_2, E_3, and E_4 correspond to the residuals of the τ/τ_f-γ/γ_r, G/G_0-τ/τ_f, G/G_0-γ/γ_r, and h-γ/γ_r relationships, respectively (Fig. 2). The subscripts "cal." and "test" are the values calculated from the GHE-S model and the values obtained from the deformation characteristic test, respectively. N_c is number of element test data. The data after the hysteretic damping h decreased were excluded from the fitting calculation (Fig. 2d).

E_1 has a small shear stress until the normalized shear strain x exceeds approximately 10^{-1}, so the residual (difference between deformation characteristic test value and calculated value) is accordingly small, but when the normalized shear strain x exceeds 10^{-1}, then the normalized shear stress y sharply increases. Therefore, if the parameter were inadequate, the residual in the large strain region of $10^{-1} < x$ became significant. It can be said from this that E_1 is a residual assessment equation that emphasizes the large strain region.

Additionally, E_3 is an equation that assesses the residual of shear stiffness ($G/G_0 = y/x$), and the stiffness decreases sharply as the strain increases. Even if the parameter were inadequate, E_3 would be assessed as a small residual in the large strain region. As a result, the influence of E_3 in (6a) would decrease. It can be said from this that E_3 is a residual assessment equation that emphasizes the small strain region.

Meanwhile, E_2 has the relationship $E_2 = E_1 + E_3$ from (6b), and when y/x takes a value close to 0 in the large strain region, then y takes a value close to 1, and conversely, when y/x takes a value

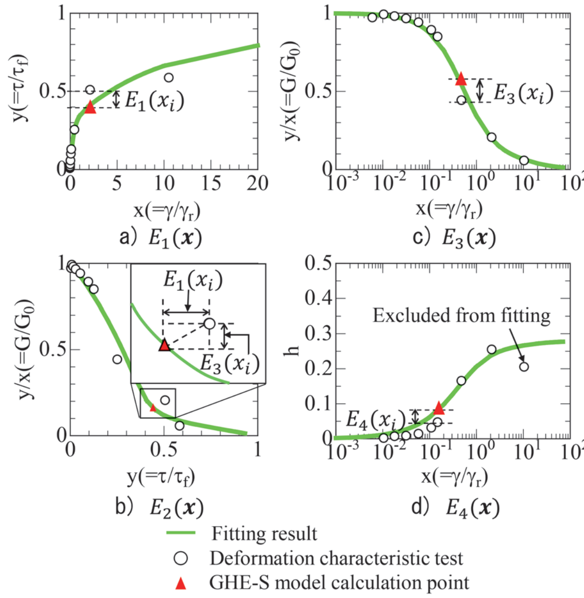

Fig. 2 Schematic diagram of the residual of the objective function of the optimization method for skeleton curves and hysteretic damping curve

close to 1 in the small strain region, then y takes a value close to 0. It can be said from this that E_2 is a residual assessment equation that can simultaneously assess the impact of parameters in both the small and large strain regions.

2.2.4 Optimization problem setting

The optimization problem for fitting the GHE-S model in this paper, including the constraints of (4) and (5) and the objective function of (6), is defined as follows:

$$\min\{\, E(\boldsymbol{m}) + r \cdot \max[0, \max(\boldsymbol{P})] \,\} \tag{7}$$

where $\boldsymbol{P}$ incorporates the constraint conditions (upper and lower limits of parameters) of (4) and (5) as a penalty function, r is the penalty factor and set to $r=2n$, and n is the number of unknowns in this optimization problem ($n=6$).

The optimization calculation starts from the initial value $\boldsymbol{x}_0$, and iterative calculations are conducted to obtain GHE-S parameters ((3)) that minimize (7). The GHE-S standard parameters [1] were set for the initial value $\boldsymbol{x}_0$ of the optimization calculation.

2.3 Estimation of GHE-S parameters

The deformation characteristic test data used in this examination were obtained by applying the test method proposed by some of the authors (henceforth referred to as the 'RTRI method' [5] to Toyoura sand, silica sand No. 6, and silica sand No. 8, each with relative densities Dr=60 and 80% (list of soil samples used for fitting is shown in Table 1). Fitting of the deformation characteristic test data was conducted by three analysts with different analytical experience or by the optimization method described in 2.2. The reference strain γ_r was calculated using the relational expression shown in (8):

$$\begin{cases} \tau_f = \sigma' \cdot \tan\phi' \\ \gamma_r = \tau_f / G_0 \end{cases} \tag{8}$$

Figure 3 shows the fitting results (For reasons of space limitation, only the results for sample No. 1 are shown.). The features of

Table 1 List of soil samples used for fitting

Sample No.	Sample name	Internal friction angle ϕ'(deg)
1	Toyoura sand Dr60%	35.7
2	Toyoura sand Dr80%	37.6
3	Silica sand No. 6 Dr60%	38.2
4	Silica sand No. 6 Dr80%	38.2
5	Silica sand No. 8 Dr60%	40.3
6	Silica sand No. 8 Dr80%	39.7

* Confining pressure σ' = 100(kPa)

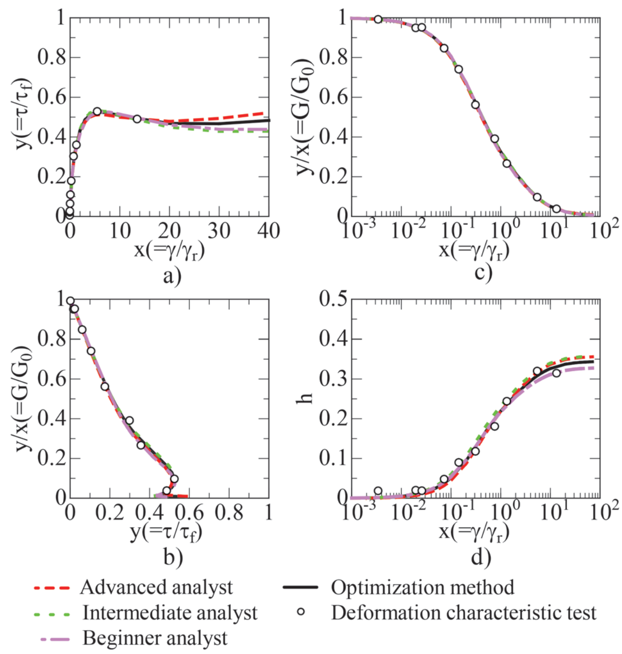

Fig. 3 Fitting result (Toyoura sand D_r60%)

the fitting results for each relationship are described below.

a) τ/τ_f - γ/γ_r relationship (E_1)

No differences between each analyst and the optimization method can be seen in the small strain region (normalized shear strain $x<2.0$), but a difference can be seen in each in the large strain region of $x>2.0$.

b) G/G_0 - τ/τ_f relationship (E_2)

This relationship is thought to be affected by τ/τ_f-γ/γ_r and G/G_0-γ/γ_r, and as described later, the G/G_0-γ/γ_r relationship is almost the same regardless of the analyst, so the residual of each fitting is determined by the residual of the τ/τ_f-γ/γ_r relationship (E_1). However, the residual is relatively small compared to that from the τ-γ relationship (E_1).

c) G/G_0 - γ/γ_r relationship (E_3)

Almost identical fitting results were obtained for the soil samples as a whole, with no differences between each analyst and the optimization method.

d) h - γ/γ_r relationship (E_4)

There were differences, because the beginner analysts had conducted fitting including the point where the damping decreased, but

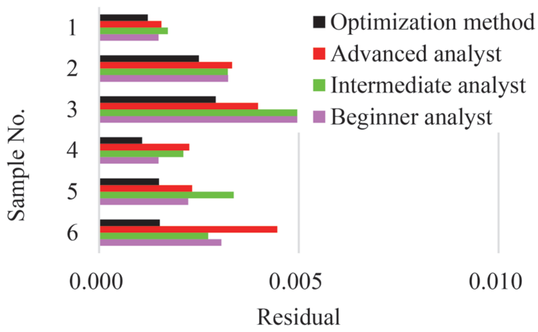

Fig. 4 Comparison of residual

the other analysts obtained results similar to the fitting results obtained by the optimization method.

Figure 4 show a comparison of the residuals with the deformation characteristic test values calculated based on (6) using the GHE-S parameters obtained by each analyst and optimization method. The optimization method had smaller residuals than each analyst, regardless of the soil sample. Therefore, it could be said that the test data was most appropriately estimated by the optimization method.

Meanwhile, it is thought that the estimation results by each analyst were generally varied values based on the fitting conditions and the comparison with the residual values of the optimization method. Therefore, it is thought that the parameters could be estimated with sufficient accuracy even by conventional trial-and-error fitting. In this study, all analysts were able to fit all the samples relatively easily and accurately, so no significant differences were observed between analysts. Meanwhile, there is a possibility of a large variation in parameters among analysts when analyzing deformation characteristic test data where fitting was difficult. In such cases, it is thought that appropriate and objective parameters could be estimated in a short period of time without human error by applying the residual-based optimization method that is proposed in this paper.

3. Study on testing method

3.1 Overview of examination

In this study, we compared the results of dynamic ground response analysis with the results of the hybrid ground response test [5] (henceforth referred to as “hybrid test”) to verify the accuracy of the deformation characteristic test. In the hybrid test, the input displacement to the target layer is calculated in dynamic ground response analysis, and the displacement is directly applied to the soil specimen in the soil testing machine to calculate stresses of the target layer, which are then fed back to dynamic ground response analysis. By repeating this process, precise evaluation of seismic ground response can be performed. Figure 5 shows the target

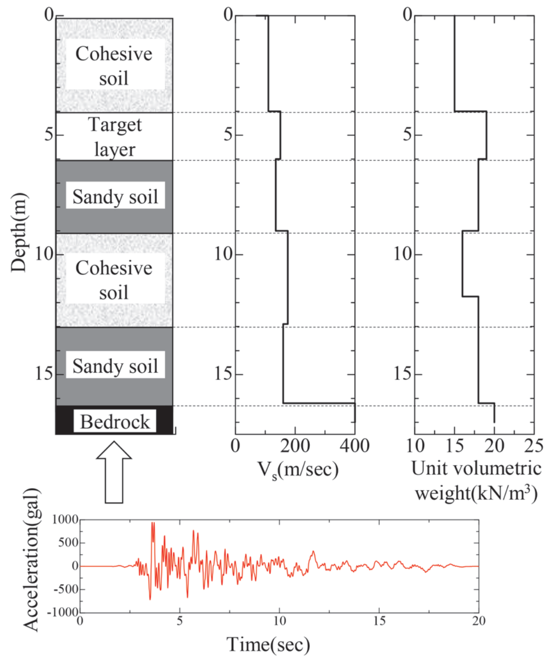

Fig. 5 Layer configuration and input seismic motion

ground structure and input seismic motion. We set the target layer consisting of Toyoura sand (relative density Dr=60%) at a depth of 4–6 m. For the dynamic ground response analysis, we set the GHE-S parameters of the target layer from the deformation characteristic test results. For the other layers, standard parameters described in the seismic standard [1] were used. Rayleigh damping was used for the damping, which was set based on the natural period of the ground ($\alpha = 1.019$, $\beta = 0.002$) with reference to Fukushima and Midorikawa [6]. A cohesive boundary that was equivalent to $\rho = 2.0$ g/cm^3, $V_s = 400$ m/s was set on the bedrock, and the seismic standard L2 seismic motion (spectrum II, G1 ground) [1] was input.

3.2 Deformation characteristic test

For the deformation characteristic test for setting the GHE-S parameters, two types of cyclic loading tests (RTRI type [5], JGS type [3]) and an undrained monotonic loading test were conducted for Toyoura sand (Dr=60%) using a hollow torsional shear tester. Table 2 shows an overview of the cyclic loading test method. The main difference between the RTRI method and the JGS method is the number of cyclic loads for each stage, with the JGS method conducting 11 cycles and calculating the deformation characteristics on the 10th cycle, whereas the RTRI method involves repeating once each. Drainage is conducted between each stage in the JGS method, but this is not done with the RTRI method. In addition to these two types of test methods, the deformation characteristic test results of the RTRI method were used up to the intermediate strain

Table 2 Outline of cyclic loading test

	RTRI type [5]	JGS type [3]
Amplitude setting	Strain amplitude	Strain amplitude
Loading method	Strain control	Stress control→Strain control
Input waveform shape	Triangular wave	Sine wave
Loading rate	Strain rate 0.1%/min	Frequency 0.2 Hz
Number of cycles per stage	1	11 (use 10th cycle as data)

Table 3 GHE-S parameters set from each test

	C1(0)	C1(∞)	C2(0)	C2(∞)	α	β	h_{max}	κ	γ_d	γ_{lim}
RTRI-1	1.0000	0.0112	0.4041	1.0000	1.5381	1.1989	0.3403	1.1338	0.0049	0.1953
RTRI-2	1.0000	0.0607	0.1199	1.0000	0.4612	1.9496	0.3397	1.1324	0.0049	0.1953
JGS	1.0000	0.0030	4.3100	1.0000	0.6083	2.7623	0.2655	1.0245	0.0021	0.1212

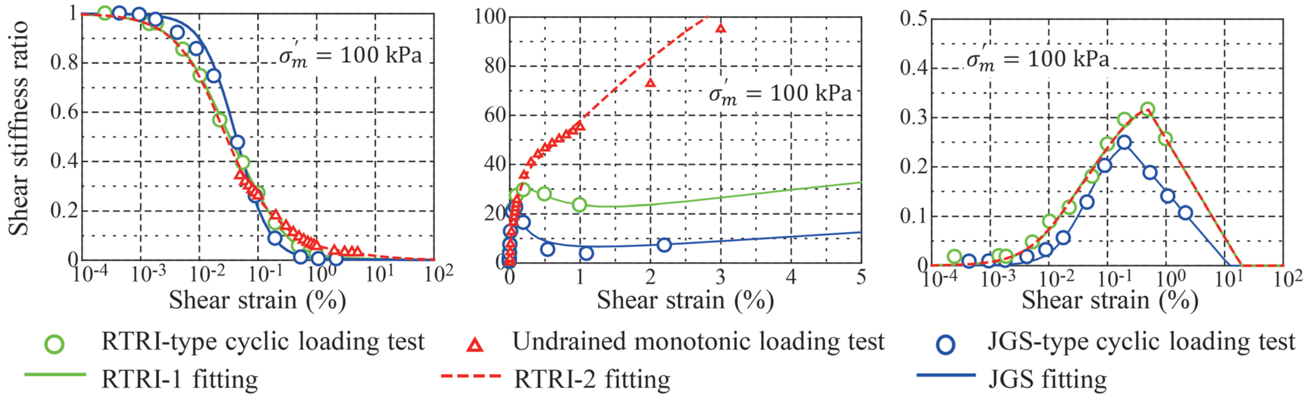

Fig. 6 Deformation characteristic test results and parameter fitting conditions

region, and the method using the monotonic loading test results in the large strain region (roughly $\gamma > 0.05$–0.1%) was also examined. In this case, the test results for the RTRI method were used for the hysteretic damping h. Based on the above, the parameters were set and the seismic response analysis of the ground was conducted using the following three methods: (1) RTRI-1 (RTRI-type cyclic loading test only), (2) RTRI-2 (RTRI-type cyclic loading test + undrained monotonic loading test), and (3) JGS (JGS-type deformation characteristic test). Table 3 shows the set GHE-S parameters, and Fig. 6 shows the relationships for the test results and fitting results.

3.3 Analysis results and comparison with hybrid test results

Regarding the analysis results conducted using each parameter and the hybrid test results, the τ-γ relationship for the target layer is shown in Fig. 7, and the acceleration, displacement, shear stress, and shear strain maximum response depth distributions are shown in Fig. 8. For the τ-γ relationship, RTRI-1 and JGS showed excessive strain compared to the hybrid test results, and the stress level also tended to be small. Additionally, the shape was very distorted, and it is thought that the application limit of the model was reached. The reason for this was that the stiffness was calculated to be excessively low due to increase in excess pore water pressure by repeated shear events, and this was modeled as the strain softening (as can be seen in Fig. 6). Meanwhile, in RTRI-2, which combined the monotonic loading test results, the strain level was shown to be similar to that of the hybrid test, showing a relatively high reproducibility. However, in the τ-γ relationship, the shear stress increased sharply due to cyclic mobility in the large strain region, but the total stress analysis used in this examination cannot reproduce the increase in effective stress, so the shear stress was underestimated regardless of the method.

For the maximum response depth distribution, RTRI-2 showed high reproducibility of displacement and shear strain across all layers. Meanwhile, RTRI-1 and JGS showed poor reproducibility due to excessive deformation of the target layer. Additionally, the maximum response to shear stress for RTRI-1 and JGS was confirmed at the spike-shaped portion during unloading. If we assume this to be due to modeling limitations and we ignore the spike shape as a result, then the maximum shear stress of the target layer was in the order of RTRI-2 > RTRI-1 > JGS; it was also confirmed that the

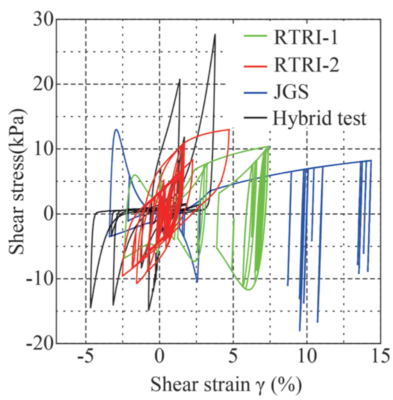

Fig. 7 Shear stress-shear strain elationship at the target layer

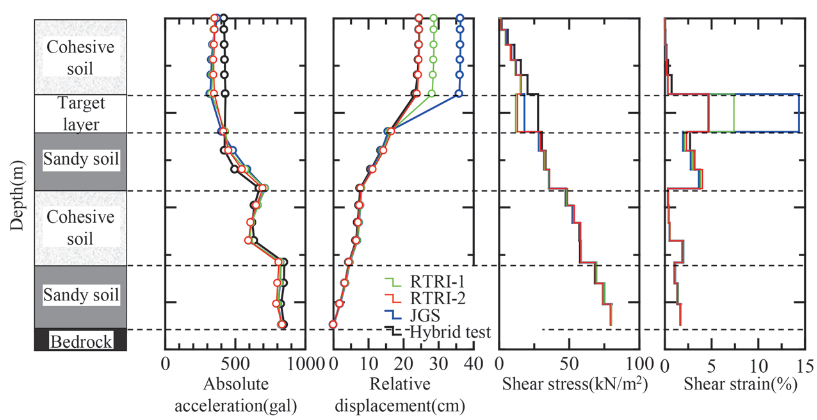

Fig. 8 Maximum response depth distribution

stress level in the large strain region was underestimated due to the increase in the number of cyclic loadings in the deformation characteristic test. Additionally, the acceleration response was underestimated to the same extent in all cases from the target layer to the upper layer, and this was thought to be the result of the above-mentioned underestimation of the shear stress.

From the above, it can be said that by using the shear stiffness obtained from monotonic loading test results we can accurately evaluate the dynamic response of the surface ground observed in the hybrid dynamic ground response analysis and simulate real soil behavior.

4. Conclusions

In this paper, setting and testing methods for deformation characteristics of soils for a dynamic ground response analysis were studied. The results obtained are summarized below.

- We proposed a deformation characteristics parameter-setting method using an optimization technique. It was confirmed that the proposed method could be used to set the parameters more accurately than three designers with different experience.
- In cyclic shear tests of soil, it was shown that a slight difference in cyclic numbers causes quite large differences in the shear stiffness in large strain levels. In addition, it was found that these differences may affect the results of the dynamic ground response analysis.
- It was confirmed that using the shear stiffness obtained from monotonic loading test results it is possible to accurately evaluate the dynamic response of the surface ground observed in the hybrid dynamic ground response analysis and simulate real soil behavior.

References

[1] Railway Technical Research Institute, *Design Standards for Railway Structures and Commentary (Seismic Design)*, 2012 (in Japanese).

[2] Murono, Y., Nogami, Y., Tanoue, K. and Sakai, K., "Evaluation of Nonlinear Dynamic Response at Subsurface Ground Applying GHE-S Model," *RTRI REPORT*, Vol. 25, No. 9, pp. 13-18, 2011 (in Japanese).

[3] Japanese Geotechnical Society, *Japanese standards and explanations of laboratory tests of geomaterials*, 2020 (in Japanese).

[4] Kappel, F. and Kuntsevich, A., "An implementation of Shor's r-algorithm," *Computational Optimization and Applications*, Vol. 15, No. 2, pp. 193-206, 2000.

[5] Izawa, J., Toyooka, A., Kojima, K. and Murono, Y., "Deformation properties of soils for a nonlinear dynamic response analysis," presented at the *7th International Conference on Geotechnical Earthquake Engineering*, 2019.

[6] Fukushima, Y. and Midorikawa, S., "Evaluation of site amplification factors based on average characteristics of frequency dependent Q−1 of sedimentary strata," *J. Struct. Constr. Eng.*, Vol. 59, No. 460, pp. 37-46, 1994 (in Japanese).

Authors

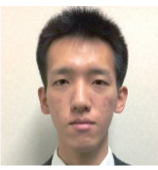

Keigo TSUKIOKA
Researcher, Soil Dynamics and Earthquake Engineering Laboratory, Center for Railway Earthquake Engineering Research
Research Areas: Earthquake Engineering

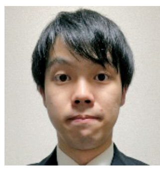

Tomoya ONODERA
Researcher, Soil Dynamics and Earthquake Engineering Laboratory, Center for Railway Earthquake Engineering Research
Research Areas: Earthquake Engineering

Yasutomo YAMAUCHI
Engineer, Dia Nippon Engineering Consultants Co., Ltd.
Research Areas: Earthquake Engineering

Jun IZAWA
Technical Manager, Center for Railway Earthquake Engineering Research
Research Areas: Earthquake Engineering

Masanori YAMAMOTO
Researcher, Soil Dynamics and Earthquake Engineering Laboratory, Center for Railway Earthquake Engineering Research
Research Areas: Earthquake Engineering

Summaries of Papers in RTRI REPORT (in Japanese)

A Study on the Wheel-rail Impact Behavior due to a Wheel-flat by Finite Element Analysis
Risa SAITO, Hirotaka SAKAI
(Vol.38, No.8, 1-7, 2024.8)

We simulated the continuous impact force due to a wheel-flat using the finite element method to investigate the influence of running velocity and positions of the impact force generation on the rail on the mechanism of impact force generation. For each position of the impact force generation on the rail pad, the peak values of the wheel load are almost identical, confirming the reproducibility. It was also found that high frequency vibrations are generated on the rail when the running velocity is 100 km/h or 130 km/h and the vibrations caused the peak value of the wheel load to increase. Finally, the relationship between the running velocity and the peak value of vertical acceleration of the axlebox by the proposed method was compared with that obtained from the experiment. Since they were close, we can say that the proposed analysis method is reasonable to use.

Wheel/Rail Tangential Contact Force Model for Analyzing Vehicle Dynamics under Running in Rainy Conditions
Daisuke YAMAMOTO
(Vol.38, No.8, 9-15, 2024.8)

This paper describes a wheel/rail tangential contact force model for analyzing vehicle dynamics under running in rainy conditions. So far, vehicle dynamics analyses have been conducted under only dry conditions. In this study, the authors investigated and proposed a wheel/rail tangential contact force model for analyzing vehicle dynamics under running in rainy conditions. The proposed model combines Kalker's linear rolling contact theory with the relationship between adhesive coefficient and velocity measured in running experiments. The validity and generality of the proposed model was confirmed by the measurement experiment of tangential contact force using a twin-disc rolling machine.

Improving the accuracy of Seismic Ground Motion Estimation along Railways by Integrating Observed and Estimated Data
Naoyasu IWATA, Misa MORIWAKI, Shunta NODA, Hirotoshi MATSUBAYASHI, Shunroku YAMAMOTO
(Vol.38, No.8, 17-24, 2024.8)

In the event of an occurrence of earthquake, railway companies suspend trains as soon as possible, considering the seismic intensity. Subsequently, if necessary, they inspect railway facilities based on seismic ground motion (SGM), which is spatially discrete, observed along the railways. In some cases, time required for safety inspections may be considerable depending on the circumstances. Estimating spatially continuous SGMs is one of the key technologies for reducing inspection time, since the early resumption of train operations after earthquakes has become a significant issue recently. In this study, we first describe differences in SGM between measured data and true data in conventional systems and then propose a method to estimate spatially continuous SGMs by integrating observed data and estimated data. Furthermore, a case study is presented in which the proposed method is employed to estimate SGMs along a virtual railway, assuming additional data observed by seismometers along a railway.

FEM Analysis for Construction of Rail Head Transverse Defect Detection System Using Guided Wave
Yuki KONAYA, Mitsuru HOSODA, Ryuichi YAMAMOTO
(Vol.38, No.8, 25-31, 2024.8)

Simulations of ultrasonic wave propagation in cracked rails have been carried out to investigate a method of detecting transverse rail head cracks using guided waves. The results show that 100~150 kHz input frequencies are suitable for detecting rail head cracks, and that the intensity of the first few waves in the received signal waves decreases with the degree of cracking. Further investigation shows that transverse cracks greater than 20 mm that have grown below horizontal cracks can be detected by checking the intensity of the first 3 waves in the received signal waves at the 100 kHz.

Numerical Analysis Method for Seismic Behavior of a Train with Consideration of up to Post-derailment Period
Keiichi GOTO, Kohei IIDA, Munemasa TOKUNAGA
(Vol.38, No.9, 1-7, 2024.9)

The authors are researching with the aim of establishing a numerical analysis method capable of evaluating vehicle behavior up to after the derailment of a vehicle during earthquakes. In this paper, as a basic study, we propose an analysis method that can represent seismic vehicle behavior before and after the derailment of a single stationary vehicle. Then, to consider the coupling of multiple vehicles, the proposed method is also extended to include dynamic models of connection elements between vehicles. Furthermore, the influence of the interaction between vehicles on the derailment limit is investigated through trial calculations.

A Control Method of Stationary and On-board Energy Storage Systems for Use of Renewable Energy
Takeshi KONISHI, Takamitsu OGATA, Tamanosuke OIDE, Tatsuhito SAITO
(Vol.38, No.9, 9-15, 2024.9)

The installation of renewable energy is accelerating to achieve the carbon neutrality in 2050. This paper proposes a control system for integrating charge/discharge of stationary and on-board energy storage systems in the DC electrified railway. By simulating the performance of a train operation power, we can obtain the effect of the demand response and effective use of renewable energy by adopting the control system.

Method for Determining the Degree of Impact on the Track due to the Damage of a Submerged Pipe in a Railway Embankment
Takashi NAKAYAMA, Yu OHARA, Akihiko MIWA, Takaki MATSUMARU
(Vol.38, No.9, 17-22, 2024.9)

When small-diameter pipes buried in railway embankments are damaged, there is concern that the surrounding ground may loosen, leading to a decrease in ground reaction forces and track settlement. In this study, we calculated the distribution of subgrade reaction coefficients on the roadbed surface when a pipe is damaged, and created an impact assessment chart that can easily determine the impact on the track based on the depth and diameter of the damaged pipe. The validity of the calculation method for the distribution of subgrade reaction coefficients has been verified by means of model tests and field tests.

Development of Steam Weeding Technique with Excellent Weed-Controlling Effect and Usability
Hikaru TANIGAWA, Tomoyoshi USHIOGI, Masateru IKEHATA, Takahisa NAKAMURA
(Vol.38, No.9, 23-28, 2024.9)

Currently, bush cutters are widely used for weed control along railway tracks. However, this method has some issues. For example, one of issues is that weeds regrow quickly after being cut during summer. Therefore, there is a need for more effective and efficient weed control methods. To address this need, we developed a specialized steam weeding equipment. This equipment consists of an ordinary steam cleaner and newly developed handheld nozzles. To verify the effectiveness of the developed equipment, it was tested in areas with vigorous weed growth. The test showed that this equipment provided effective usability with less labor and time. Furthermore, it was also confirmed that large weed regrowth was reduced by 70% after one year compared with bush cutter.

Dynamic Response of Steel Girders with Rail Joints during Train Passage

Haruyuki KITAGAWA, Munemasa TOKUNAGA, Manabu IKEDA

(Vol.38, No.9, 29-36, 2024.9)

The aim of this study is to elucidate the mechanism of the increase in the dynamic response of the bridge due to the passage of a train through a rail joint. The numerical results showed that the dynamic response due to the passage of a rail joint is amplified by the resonance that occurs when the excitation frequency with the passage of two wheelsets in a bogie coincides with the natural frequency of the bridge. Furthermore, the impact factor for rail joint is more sensitive to span than the calculation method of design standard and decreases as the bridge span increases.

Validation of Bedrock Motion Estimation Based on Time Domain Non-linear Analysis

Kimitoshi SAKAI

(Vol.38, No.9, 37-43, 2024.9)

We confirmed the effectiveness of a proposed method for estimating earthquake ground motion from observation waveforms at the ground surface based on time domain nonlinear analysis. Specifically, earthquake ground motion was estimated using the proposed method for various kinds of earthquake motion and ground conditions, and the results were compared with those of a conventionally used frequency domain method. The result confirmed that the proposed method can estimate more appropriate earthquake ground motion in all the cases investigated here. Therefore, the proposed method is an effective method for estimating earthquake ground motion, appropriately taking into account the effects of the ground non-linearity.

Allowable Strain Value for Contact Wires Taking into Account the Probability of Failure

Takuya OHARA, Chikara YAMASHITA

(Vol.38, No.9, 45-51, 2024.9)

The allowable strain value for all types of contact wire, including the high strength contact wires, has been set to 500×10^{-6} based on the fatigue characteristics of a basic hard-drawn copper. However, as train speeds increase, the strain value of contact wires may increase to more than 500×10^{-6} in the future. Therefore, in this paper, the authors propose a method for setting allowable strain values for each contact wire taking into account the probability of failure. This probability is consistent with the margins of the conventional allowable strain value of 500×10^{-6}. In addition, using this method, we propose allowable strain values for four types of high strength contact wires.

Trial Design of the Bearing Applying the Revised Standard for Railway Concrete Structures

Ryo SUZUKI, Shuntaro TODOROKI, Yuki NAKATA, Ken WATANABE

(Vol.38, No.9, 53-56, 2024.9)

Based on previous research, the formulas and values in the Design Standard and Commentary for Railway Structures (Concrete Structures) have been revised. In this report, we compare bearing designed based on the revised standard (published in 2023) with those designed based on the current standard (published in 2004). Consequently, this comparison reveals the influence of the updating formulas on the strength of the embedded part of stopper at girder and of the revision of the design value on concrete shrinkage and creep, durability, etc.

Numerical Analysis on Mechanism of Aerodynamic Noise Reduction in Bogie Area by Rounding Corners of Bogie Cavity

Tatsuya TONAI, Toki UDA

(Vol.38, No.10, 1-6, 2024.10)

Aerodynamic noise radiated from running high-speed trains is attracting attention from the environmental point of view. Bogie areas are known to be the main sources of the aerodynamic noise. Rounding the four corners of the bogie cavity has been proposed as a measure to reduce bogie aerodynamic noise, and wind tunnel tests have confirmed its effectiveness. However, detailed flow fields around bogie area have not been identified and the mechanism of noise reduction by such measures remains unclear. In this study, numerical analyses on the flow field near the bogie area were conducted to investigate the changes in the flow field caused by the proposed measure and to discuss the reduction mechanism.

Development of Prototype Current Monitoring System for Detecting High-resistance Earth Faults in DC Traction Power Supply Systems

Masataka AKAGI, Minoru KONDO, Kenta IMAMURA, Yusuke KAWAMURA, Satoko RYUO

(Vol.38, No.10, 7-14, 2024.10)

In DC 1.5 kV traction power supply systems for electrified railway, it is difficult to detect high-resistance earth faults using only electrical measurements installed in traction substations. On the other hand, utilizing the current data of both substations and vehicles, methods for detecting fault based on Kirchhoff's law have been proposed for the past 30 years. The recent rapid progress in the fields of telecommunication technology leads to increasing the possibility of realizing this method. Therefore, we have developed a prototype of current monitoring system for traction power supply systems which can distinguish the fault current with about 100 amperes by combining this method with telecommunication technology.

Aerodynamic Noise Reduction of Pantograph Head Support by Applying Flow Bypass Technique

Takeshi MITSUMOJI, Yuki AMANO, Mariko AKUTSU, Kyohei NAGAO, Isamu MAKARA, Yusuke WAKABAYASHI

(Vol.38, No.10, 15-21, 2024.10)

Reduction of aerodynamic noise emitted by a pantograph is an important challenge to reduce environmental impact and increase the speed of high-speed trains. In previous studies, a method for reducing aerodynamic noise has been proposed by applying porous material to pantograph head support covers. In this study, a new practical method is proposed to achieve the same aerodynamic noise reduction effect as using porous material. On the basis of a wind tunnel test result, it is clarified that the new method can reduce aerodynamic noise to almost the same extent as using porous material.

Transition Mechanism between Adhesive Wear Mode and Seizure Wear Mode of Current Collecting Materials

Koki NEMOTO, Chikara YAMASHITA

(Vol.38, No.10, 23-30, 2024.10)

In electric railways, measures to reduce wear of current collecting materials such as contact wires and contact strips are required to reduce the maintenance costs of current collecting materials based on the wear mechanisms. The authors have so far clarified that there are four mechanical wear modes of current collecting materials. However, the transition mechanism between adhesive wear mode and seizure wear mode has not been explained. In this paper, in order to elucidate the mechanism, the authors developed a model for analyzing contact temperatures considering the number of contacts. Using the developed model, the number of contacts was estimated by comparing analytical and experimental results. It shows that the number of contacts of seizure was less than that of adhesive wear. It was also clear that the transition to seizure occurs when the surface pressure exceeds the hardness of the material.

Information Provision Conditions Based on the Survey of the Usefulness of Guidance on the Train Congestion during Train Traffic Disruption

Daisuke TATSUI, Shunichi TANAKA, Taketoshi KUNIMATSU, Yoko TAKEUCHI

(Vol.38, No.10, 31-37, 2024.10)

Passengers' interests in train congestion have been growing up. In our previous research, we confirmed that passengers tend to be interested in both highly congested trains and low congested trains during train traffic disruptions. Therefore, we conducted a Web-based survey to understand the usefulness of providing information on the predicted train congestion. As a result of the survey, we obtained conditions for providing information during train traffic disruptions. In this paper, we describe an overview of the Web questionnaire, the results of the analysis, and the method of setting conditions for providing information that passengers are highly interested in, during traffic disruptions.

Trial Design of the Girder Applying the Revised Standard for Railway Concrete Structures

Ryo SUZUKI, Mami NAKAMURA, Munemasa TOKUNAGA, Ken WATANABE

(Vol.38, No.10, 39-42, 2024.10)

Based on previous research, the formulas and values in the Design Standard and Commentary for Railway Structures (Concrete Structures) have been revised. In this report, we compare RC/PC/PRC girders designed according to the revised standard (published in 2023) with those designed according to the current standard (published in 2004). Consequently, this comparison shows the influence of the updating formulas for the shear strength of RC/PC/PRC members and the revision of the design value for concrete shrinkage and creep, durability, etc. on the design aspects.

ERRATA

Vol.65, No.1 (Feb. 2024)
Paper title: Development and Performance Evaluation of Rail Fastening System Using Non-metallic Materials for Main Members
Page: 50
Table 2: In the item for the right-most column, the second from the bottom, “Carbon (chopped)” should be changed to “Glass (chopped).”

Error

Table 2 Material composition of proposed components

Component	CFRP spring clip	GFRP baseplate	FRTP baseplate
Resin	Epoxy resin	Vinyl ester resin	Polyamide
Fiber	Carbon (prepreg)	Glass (fabric)	Carbon (chopped)
Manufacturing method	Press molding	Hand lay-up	Injection molding

Correct

Table 2 Material composition of proposed components

Component	CFRP spring clip	GFRP baseplate	FRTP baseplate
Resin	Epoxy resin	Vinyl ester resin	Polyamide
Fiber	Carbon (prepreg)	Glass (fabric)	Glass (chopped)
Manufacturing method	Press molding	Hand lay-up	Injection molding

QUARTERLY REPORT of RTRI

第 65 巻　第 4 号	Vol. 65, No. 4
2024 年 11 月 1 日　発行	Published date: 1 November 2024
監修・発行所：公益財団法人鉄道総合技術研究所	Supervision/Publisher: Railway Technical Research Institute
〒 185-8540　東京都国分寺市光町 2-8-38	Address: 2-8-38 Hikari-cho, Kokubunji-shi, Tokyo 185-8540, Japan
発行人：芦谷公稔	Issuer: Dr. Kimitoshi ASHIYA
問い合わせ：鉄道総研広報	Contact us: Public Relations, Railway Technical Research Institute Mail Address: rtripr@rtri.or.jp

QUARTERLY REPORT of RTRI

RAILWAY TECHNICAL RESEARCH INSTITUTE

Printed in Japan